Thermochronologic and geochronologic investigations of the pre-volcanic crystalline basement of Thera (Santorini), Greece: Determining the tectonostratigraphy and deformational history of the metamorphic core

Allan Lion

A thesis submitted in partial fulfillment of the requirements for the
Master's degree in Earth Sciences

Department of Earth and Environmental Sciences
Faculty of Science
University of Ottawa

Abstract

The cores of most Cycladic Islands are formed as consequences of early Paleogene high-pressure subduction processes of the African plate beneath Europe, and Miocene extensional exhumation of the subduction trench. The island of Thera (Santorini) resides in the Hellenic Volcanic Arc, and is dominated by Quaternary eruptive volcanic material atop a pre-volcanic basement. The position of the island has led to debate as to the nature of the pre-volcanic basement, with connections drawn to either the Cycladic Blueschist Unit (CBU) or the Phyllite-Quartzite Unit (PQU). Field observations, which document a top-to-SSE detachment, in conjunction with geochronological techniques have been applied to assess the tectonostratigraphy of the pre-volcanic basement. The results resolve the pre-volcanic basement as belonging to the CBU which has been juxtaposed against Sub-Pelogonian marble by the SSE directed detachment. This firmly establishes Thera within the Cycladic realm, documents Miocene deformation, and changes the geologic map of the Hellenides.

Résumé

Les Îles Cycladiques ont été formées par des processus de haute pression lors de la subduction de la plaque Africaine sous la plaque Européenne durant le Paléogène suivi par un régime d'extension lors de son exhumation pendant le Miocène. L'île de Théra (Santorini) est située dans l'arc volcanique des Hellénides et est majoritairement composée de roches volcaniques éruptives quaternaire sur un sous-sol pré-volcanique. La position de l'île mène au débat l'origine du sous-sol qui est soit attribué au Schiste Bleu Cyladique (CBU) ou à l'Unité Phyllite-Quartzite (PQU). Les observations de terrain, ayant identifié un décollement en direction SSE, en conjonction avec des techniques géochronologiques ont été appliquées pour déterminer la

tectonostratigraphie de l’île. Les résultats confirment que le sous-sol consiste de CBU ayant été juxtaposé contre des marbres Sous-Pélagonien par le décollement. Ceci prouve l'appartenance de Théra au domaine Cycladique et date sa déformation durant le Miocène ce qui apporte un change à la carte géologique des Hellènides.

Acknowledgements

Firstly I would like to thank my supervisor Dave Schneider for pushing me to excel and investing in me both as a researcher and as a geologist. He has always been available to discuss and help me interpret new results, provide guidance, and most importantly, keeping me on task. This project was made possible by funding from a National Science and Engineering Research Counsil (NSERC) grant and a Natural Resources Canada grant to Dave.

I would also like to thank Samuel Morfin at the University of Ottawa ICP-MS lab for his help in conducting zircon U-Pb analysis. Jim Metcalf and the rest of the TRAIL group from the University of Colorado Boulder for (U-Th)/He analysis. Alfredo Camacho from the University of Manitoba for guidance in dating muscovite. Alain Mauviel for cutting thin sections, and Glenn Poirier and David Diekrup for help with the Microprobe and SEM.

I am grateful for many discussions with fellow graduate students and researchers, notably Mark Coleman, Renelle Dubosq, Élyse Gaudreau, Leo Lee, Meghan Moher and Jenn Spalding from the University of Ottawa, Bernhard Grasemann and Erich Draganits from the University of Vienna and Kostis Soukis from the University of Athens.

Lastly I would like to thank my friends and family for their patience and support throughout this project.

Table of Contents

List of Figures

List of Tables

Introduction

The Mediterranean region is host to an active subduction system that involves the interplay of the African, Eurasian and Arabian tectonic plates. Collison between Europe and Africa initiated subduction whereby the trench has migrated southwards over the last 50 m.y. due to slab rollback, and in the Aegean region is currently situated south of the Greek islands. As a consequence of subduction, a volcanic arc has developed in the overriding European plate in the southern Cyclades, which includes the archipelago of Santorini. Moreover, Miocene slab rollback drove bi-vergent extensional tectonism and crustal thinning to the north (Jolivet and Brun, 2010; Ring et al., 2010; Grasemann et al., 2012). Extension allowed for the exhumation of high-pressure/low-temperature (HP/LT) rocks that formed along the subduction trench to be exposed across the islands, including blueschist facies material and ophiolitic assemblages (Dürr et al, 1978; Okrush and Bröcker, 1990; Ring and Layer, 2003; Anders et al., 2007; Bröcker and Pidgeon, 2007; Jolivet and Brun, 2010; Grasemann et al., 2012). The cores of most Cycladic islands are composed of such HP/LT material leading to extensive and relatively young exposure of blueschist facies metamorphic rocks (Maruyama et al., 1996).

The HP/LT crystalline rocks have been defined as two discrete tectonic units (Davis and Bastas, 1978; Skarpelis and Liati, 1990; Marsellos et al., 2012; Grasemann et al., 2017): the Phyllite-Quartz Unit (PQU) and the Cycladic Blueschist Unit (CBU). In the case of Thera, the largest island of the Santorini archipelago, its location as the southernmost of the Cycladic islands has led to a debate as to the proper tectonostratigraphic correlation of the HP/LT rocks exposed on the island. The CBU composes the basement of the Cycladic islands to the north (Figure 1), whereas the PQU is present on Crete and the Peloponnese region to the south and west, respectively. As such, the basement on Thera has been alternatively referred to as either of these

units with the longstanding consensus that it belongs to the PQU (Bonneau, 1984; Kilias et al., 1998; Craddock et al., 2009; Marsellos et al. 2012). The Miocene extension responsible for unroofing these HP/LT rocks also caused them to be deformed and retrogressed under greenschist facies conditions, making correlations even more difficult. In the Cycladic islands, the retrogressed HP/LT rocks of the CBU comprise the footwall of regional detachment systems, which juxtapose them against the less deformed, low grade Pelagonian rocks (Grasemann et al., 2012; Jolivet et al., 2013; Liati et al., 2013) whereas on Crete the PQU has been similarly juxtaposed against limestones and marbles of the Tripolitza unit (Jolivet and Brun, 2010; Ring et al., 2010; Marsellos et al., 2012; Zulauf et al., 2015).

Recent fieldwork (Schneider et al., 2018) investigating the exhumed HP/LT rocks on the island of Thera (Santorini) has revealed the existence of a low angle detachment, that was first proposed by Kilias et al. (1998). The rocks on either side of the detachment have undergone a cursory characterization (Davis and Bastas, 1978; Skarpelis and Liati, 1990; Kilias et al., 1998). Following these early studies, a better regional understanding of the Cyclades has come to light. Through the application of multiple geochronological techniques, this study seeks to better define the island's tectonostratigraphy and to resolve the timing of deformation of the basement complex. This thesis will present evidence that the HP/LT rocks belong to the CBU, which are overlain by calcitic marble of the Pelagonian unit that contains a Peleogene metaflysch. Also proposed are age constraints on the development of this newly discovered detachment system and its role in further understanding the tectonostratigraphy of the Mediterranean domain.

Regional Geology

The Hellenic orogeny is largely responsible for the current configuration of the Mediterranean, which has been shaped by the displacement and interaction of major tectonic plates, notably between the Eurasian, African and Arabian tectonic plates and amalgamation of several microplates such as Anatolia and Apulia (Dürr et al., 1978; Jolivet and Brun, 2010; Ring et al., 2010; Thomson et al., 2010; Zulauf et al., 2015; Grasemann et al., 2017). Orogenic activity involved collision and subduction of the Apulian microplate beginning in the Mesozoic, which led to sections of Apulia being amalgamated with Eurasia. This was followed by late Mesozoic-Cenozoic obduction and stacking (from north to south) of the Pelagonian, Pindos (Cycladic Blueschist Unit), Tripolitza and Ionian blocks (Dürr et al., 1978; Jacobshagen, 1986; Ring et al., 2010; Grasemann et al., 2017), each block defined by differences in rock type, stratigraphy, geography and metamorphic history (Robertson et al., 1991).

The Pelagonian block extends southeast along central mainland Greece and continues to the Cycladic islands. It is composed of Paleozoic granites and gneisses, late Paleozoic to Mesozoic metasedimentary rocks (metaclastic rocks and calcitic marbles) and ophiolite sequences that exhibit late Jurassic to Cretaceous deformation, with portions subjected to blueschist facies metamorphism (Anders et al., 2007; Jolivet and Brun, 2010). In the Cyclades, fragments of Pelagonian units compose the structurally higher hanging wall of regional detachment systems (Dürr et al., 1978; Jolivet and Brun, 2010; Grasemann et al., 2017), and consist of ophiolitic material obducted over a pre-Alpine continental crystalline basement and its Paleozoic-Mesozoic sedimentary cover (Jolivet and Brun, 2010; Ring et al., 2010).

The Pindos unit, and its paleogeographic equivalent, the Cycladic Blueschist Unit (CBU), is a heterogeneous mix of oceanic crust and basement-cover sequences that formed Eocene

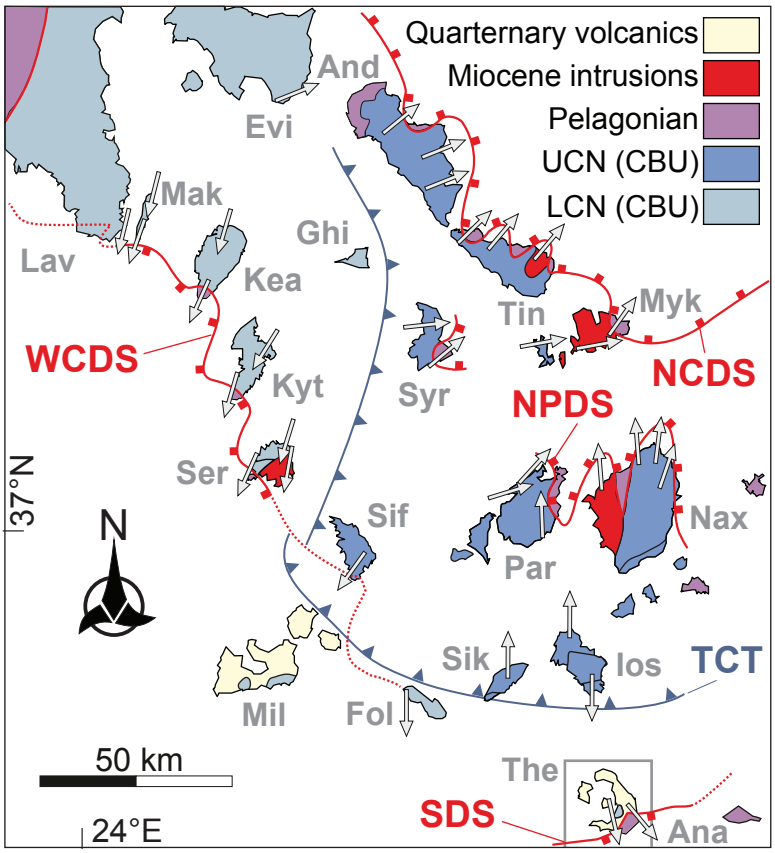

Figure 1: Simplified tectonic map of the Cyclades showing the Miocene post-orogenic shear sense (white arrows) between the Lower (LCN) and Upper Cycladic Nappes (UCN) of the CBU and undifferentiated Pelagonian-derived hanging wall units (modified from Grasemann et al., 2017 and Schneider et al., 2018). Gray box around Thera (labelled The) is location of Fig. 2. And: Andros, Ana: Anafi, Evi: Evia, Fol: Folegandros, Ghi: Ghiaros, Mil: Milos, Kyt: Kythnos, Lav: Lavrion, Mak: Makronisos, Myk: Mykonos, Nax: Naxos, Par: Paros, Ser: Serifos, Sif: Sifnos, Syr: Syros, Sik: Sikinos, The: Thera (Santorini), Tin: Tinos, NCDS: North Cycladic Detachment System, NPDS: Naxos-Paros Detachment System, WCDS: West Cycladic Detachment System, SDS: Santorini Detachment System, TCT: Trans-Cycladic Thrust.

accretionary complexes. The CBU is differentiated into a Lower (LCN) and Upper Cycladic Nappe (UCN) by the Trans Cycladic Thrust (TCT, Figure 1; Grasemann et al., 2017). The key difference between the two nappes is the degree of metamorphism with the UCN having been subjected to eclogite facies metamorphism whereas the LCN was brought to blueschist facies conditions. The CBU comprises Carboniferous metasedimentary and orthogneiss crystalline rocks overlain by younger passive margin sequences of metapelites, marbles and metavolcanics (Dürr et al., 1978; Okrush and Bröcker, 1990; Ring and Layer, 2003; Jolivet and Brun, 2010; Grasemann et al., 2017). The sediments that comprise these rocks originate from Pan-African sources as shown by U-Pb detrital zircon studies (e.g. Lister and Keay, 2002; Marsellos et al., 2010; Seman et al., 2017). Detrital zircon from Pan-African provenances possess a Neoproterozoic to Ordovician age that likely correlate to widepsread igneous events that occurred on the Pan-African continent.

The CBU underwent Eocene subduction where it was subjected to blueschist facies metamorphism. When subduction rates began to slow in the middle Cenozoic, rollback of the subducting African slab occurred in the Miocene and instigated widespread extension in the overriding plate prompting exhumation of the CBU. Exhumation and collapse of the CBU was accompanied by greenschist facies deformation, which overprinted much of the initial metamorphic signature (Altherr et al., 1979; Ring and Layer, 2003; Forster and Lister, 2005; Jolivet and Brun, 2010; Grasemann et al., 2012). The timing of greenschist overprinting has been resolved to be Miocene via $^{40}Ar/^{39}Ar$ dating in white mica and other low-temperature thermochronology (e.g., Brichau et al., 2006, 2007, 2008, 2010; Thomson et al., 2010; Grasemann et al., 2012; Bröcker et al., 2013; Cossette et al., 2015). Now exposed at the surface on many of the Cycladic islands, the CBU constitutes footwall metamorphic core complexes below regional detachment systems (Lister et al., 1984). Due to relatively rapid crustal thinning, contemporaneous

middle to late Miocene I- and S-type granitoids intrude the footwalls of these extensional detachments, and are deformed by the detachments themselves (e.g., Iglseder et al. 2009; Berger et al. 2013).

Exposed primarily in the Peloponnese region of mainland Greece, Crete and some of the southeastern Cycladic islands, the Tripolitza block is composed of Triassic to Eocene marbles and limestones. Certain sections of the Tripolitza underwent HP/LT metamorphism, notably in the Cyclades, but the southern occurrences were only weakly metamorphosed (Lips et al., 1999; Sherlock et al., 1999; Ring and Layer, 2003; Jolivet and Brun, 2010; Zulauf et al., 2015). Overlying the Tripolitza is the Ionian block, the outermost thrust unit of the Hellenides, which is composed of Carboniferous to Triassic shallow water carbonate sequences (Jolivet and Brun, 2010; Ring et al., 2010; Zulauf et al., 2015). Structurally intercalated between the Tripolitza and the Ionian blocks is the Phyllite-Quartzite Unit (PQU) that is found in parts of the Peloponnese, Kythira and Crete (Thompson et al., 1999; Ring et al., 2001; Jolivet and Brun, 2010). Comprised of clastic sediments of Mid-Carboniferous to Triassic age, the PQU is faulted against the Tripolitza (Bonneau, 1984; Kilias et al., 1998; Craddock et al., 2009; Zulauf et al., 2015). Analogous to the CBU from the Pindos block, the PQU has also been shown to possess sediments from the Pan-African continent (Marsellos et al., 2012; Zulauf et al., 2015). $^{40}Ar/^{39}Ar$ analyses in phengite from these rocks yielded Oligocene to Miocene dates of 25-15 Ma (Jolivet et al., 1996) and zircon fission track dating recorded cooling ages of 22-16 Ma (Thomson et al., 1998), suggesting relatively rapid exhumation.

The island of Thera (Santorini) is the southernmost of the Cyclades, and consists of a small archipelago of islands that formed during an explosive volcanic event c. 3600 years ago (Druitt et al., 1999). One of the few remaining active volcanoes in the Mediterranean, Thera is composed

primarily of Quaternary volcanic material atop a Carboniferous-Triassic crystalline metasedimentary basement (Davis and Bastas, 1978; Skarpelis and Liati, 1990; Marsellos et al., 2012; Grasemann et al., 2017). The pre-volcanic basement is exposed in a few localities, notably at Athinios, north of Emporio and at Profitis Ilias and Mesa Vouno (Figure 2). Although the Quaternary volcanic rocks have been studied and mapped in detail, the pre-volcanic crystalline basement remains poorly understood. Previous maps of the basement (Skarpelis and Liati, 1990; Kilias et al., 1998) do not provide much lithologic or structural detail nor do they distinguish between different units. The longstanding view is that the clastic metasedimentary rocks of Athinios and Emporio belong to the Phyllite-Quartzite Unit whereas the marble of Profitis Ilias and Mesa Vouno is part of the Tripolitza Unit, and defines Thera as geologically similar to Crete where both the Tripolitza and PQU feature prominently (Bonneau, 1984; Kilias et al., 1998; Craddock et al., 2009; Zulauf et al., 2015). This view was based on reports of *Megalodons* (bivalve mollusks) within the marbles (Papastamatiou, 1958), however these fossils have also been observed in the similar-aged marbles of the Pelagonian in mainland Greece (Mountrakis, 1987; Liati et al., 2013). Based on other fossil assemblages, an early Paleocene age has been suggested for flysch-type sediments that occur within the saddle of the marbles of Profitis Ilias (Figure 2; Tataris, 1964). Kilias et al. (1998) interprets that the flysch sequence was tectonically juxtaposed between the Triassic marbles by a top-to-NW thrusting event followed by subsequent top-to-SSE normal faulting that reactivated some earlier structures.

In contrast, Skarpelis and Liati (1990) suggested that the crystalline metasedimentary rocks at Athinios likely belong to the CBU based on similarities between the rocks at Athinios and those on other Cycladic islands. The presence of glaucophane and crossite in rocks from Athinios was observed by Davis and Bastas (1978) in conjunction with relics of preserved clinopyroxene and

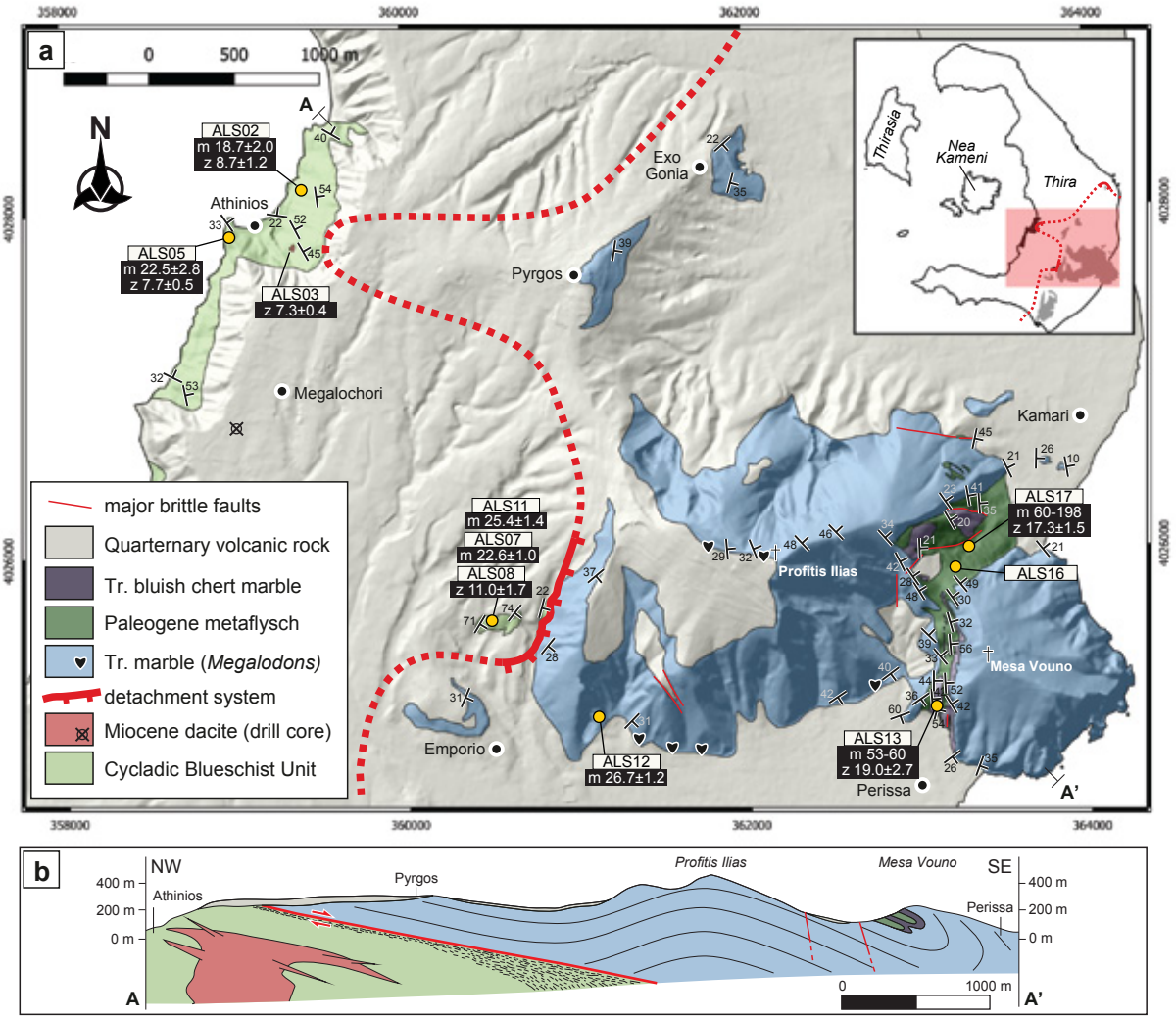

Figure 2: a) Geological map of the pre-volcanic crystalline basement (Athinios-Profitis Ilias area) on Santorini (after Schneider et al., 2018). The red line is the surface trace of the Santorini Detachment System. Structural symbols indicate dip direction and numbers are dip angles of the main foliation of the rocks. Note the dacite is a small body exposed at surface within the Cycladic Blueschist Unit southeast of Athinios (sample ALS03). The dacite was originally observed in drill core southwest of Megalochori. New geochronology (orange dots) includes (m) white mica 40Ar/39Ar and (z) (U-Th)/He zircon ages. Coordinates are given in UTM35 (NAD83). **b**) Schematic NW-SE (A-A') cross section across Santorini illustrating the structural architecture of the island. The Cycladic Blueschist Unit belongs to the Lower Cycladic Blueschist Nappe, and the overlying marble and flysch are part of the Pelagonian zone.

plagioclase phenocrysts within metabasite layers. Based on this mineral assemblage, these rocks had likely been subjected to blueschist facies metamorphism (<380°C, 11-12 kbar; Skarpelis and Liati, 1990). Furthermore, these workers described strongly deformed phengite overprinted by undeformed muscovite indicating the blueschist facies conditions was followed by a low-pressure metamorphic event. As is the case with the Cycladic islands to the north, the metamorphic core of Santorini likely experienced greenschist metamorphism during extension in the Miocene (Altherr et al., 1979; Ring and Layer, 2003; Forster and Lister, 2005; Jolivet and Brun, 2010; Grasemann et al., 2012). Miocene magmatism is often associated with the Cycladic detachment systems with a slight age trend that becomes younger to the south (Bolhar et al., 2010; Ring et al., 2010; Grasemann et al., 2017). These intrusive magmatic bodies are mostly I-type granites with Miocene ages ranging from 17-12 Ma (Bolhar et al., 2010). On Thera, an I-type granite was observed in drill core from Megalochori (labelled as a dacite, Figure 2) and was dated by Skarpelis et al. (1992) at ca. 9.5 Ma via K-Ar in biotite and $^{40}Ar/^{39}Ar$ in feldspar making it one of the youngest intrusion in the Cyclades. The intrusions are associated with localized hornfels assemblages of Grt+Cpx±Ep and silver and base metal ore mineralization in small pockets of skarns (Murad and Hubberten, 1975; Skarpelis and Liati, 1990).

New Field Observations

Based on new bedrock mapping and structural measurements (Figure 2), a hitherto unrecognized major detachment structure has been identified within the pre-volcanic rocks, and is best exposed ~1 km north of Emporio below the western flank of Profitis Ilias (Figure 3; Schneider et al., 2018). Intensely deformed quartz-rich phyllites, mylonites and metaconglomerates dip to the east below the weakly deformed marbles of the hanging wall. Abundant centimeter- to meter-

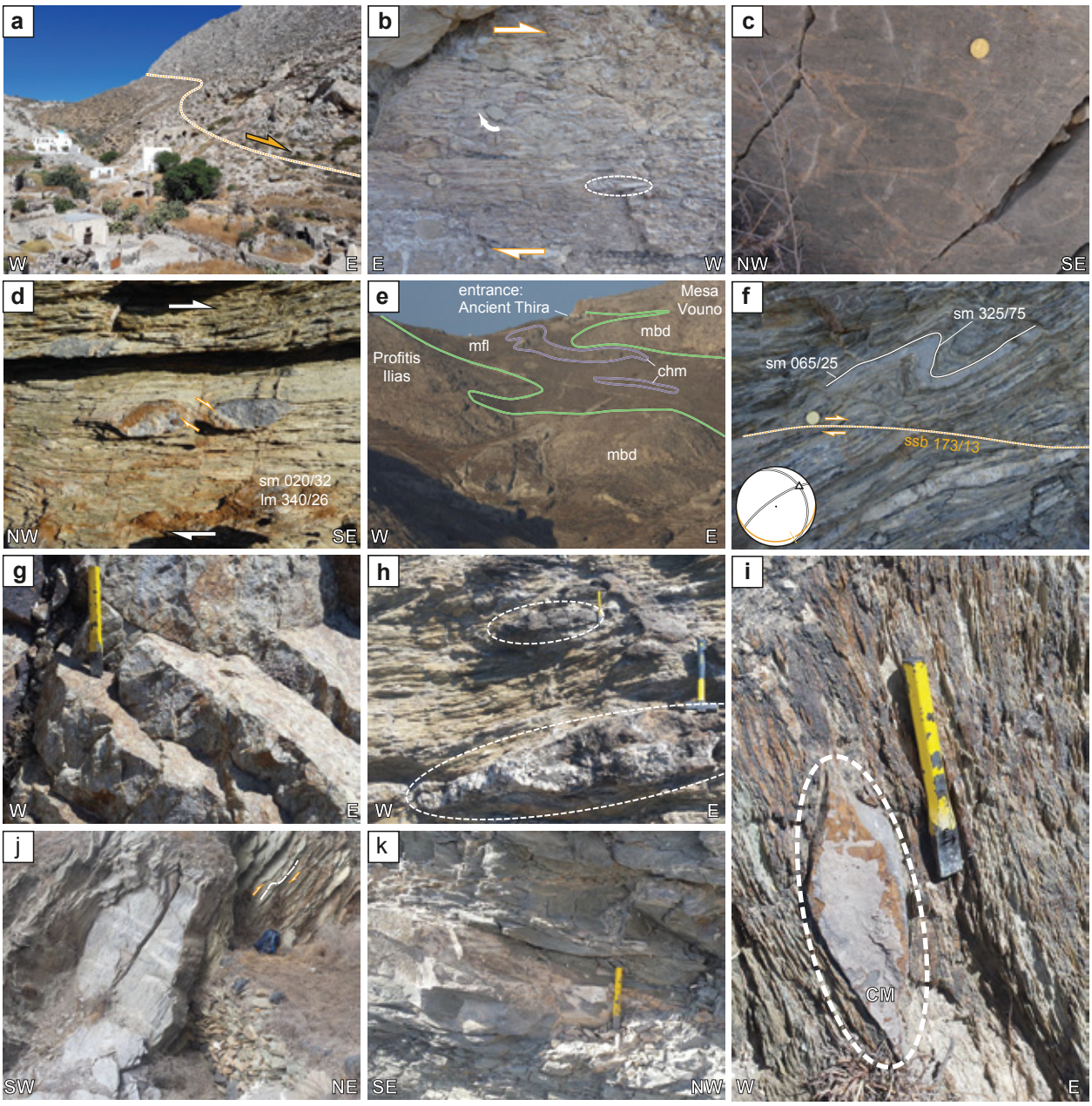
a
W
E
b
E
W
c
NW
SE
d
sm 020/32
lm 340/26
NW
SE
e
entrance:
Ancient Thira
Mesa
Vouno
mbd
mfl
Profitis
Ilias
chm
mbd
W
E
f
sm 325/75
sm 065/25
ssb 173/13
g
W
E
h
W
E
i
CM
W
E
j
SW
NE
k
SE
NW

Figure 3: a) Photo of Santorini Detachment System contact (orange dotted line) exposed ~1 km north of Emporio below the marbles of Mt. Profitis Ilias (4025472N/360706E, view towards north). **b)** Photo showing fault plane of the Santorini Detachment with arrows denoting movement. Deformation evinced by stretched layers and broken clasts (white dashed ellipse). Small clasts are evident throughout fault plane with some having been partially rotated as shown with white arrow. **c)** Photo of *Megalodon* fossils (horseshoe shape) from quarry on the western slope of Profitis Ilias, most fossils were 10-20 cm in length (4024917N, 361335E) **d)** Top-to-SSE shearing indicated by a shear band boudinage (small orange arrows) of a marble component in the metaconglomerate of the footwall (sm: main foliation; lm: stretching lineation; 4026975N/358546E). **e)** Eocene metaflysch (mfl) with chert marble mega-olistoliths (chm) refolded in a syncline above Upper Triassic marbles with *Megalodons* and dolomite layers (mbd). View is to the north of the saddle between Profitis Illias and Mesa Vouno. **f)** Top-to-SE low-angle brittle-ductile shear zone (ssb, orange dotted line) cutting a SE-vergent folded marble layer (triangle symbol in stereoplot; 4027800N/359542E). **g)** Outcrop of dacite from cliff side of Athinios harbor (4027820N, 359381E). **h)** Quartz-calcite skarn lenses occuring along foliation of schistose conglomerate at Athinios harbour (dashed ellipse). The skarn style mineralization is associated with fluids from the dacite (4027944N, 358981E). **i)** Meta-rhyolite with deformed calcitic marble (CM) clast (4025605N, 360636E) **j)** Mica schist from Emporio with well-defined chevron folds (402562N, 360528E). **k)** Weakly deformed schist from upper section of saddle of Profitis Ilias (4025970N, 363135E).

scale shear bands indicate a top-to-SE directed sense of shear. The foliated rocks are deformed by SE-vergent chevron and kink folds, which nucleate along foliation-parallel low-angle faults. Proximal to the detachment surface, metaconglomerates from the footwall and marbles from the hanging wall record a strong proto- to ultracataclastic overprint. Because of the cataclastic nature of the detachment, determining the timing of deformation directly along this structure is difficult.

All metasedimentary and metavolcanic rocks north of Emporio and at Athinios are located structurally below the detachment, forming the footwall. The metamorphic layering of these rocks,

which preserves an earlier shear fabric and isoclinal folds with roughly N-S trending fold axes, dips shallowly to steeply towards the east to northeast (Schneider et al., 2018). This variability is caused by folding with NNW-SSE trending fold axes and subhorizontal axial surfaces, along which isolated top-to-SSE shear zones are localized. Top-to-SSE shearing is preserved throughout all lithotypes (Figure 3), but the intensity of mylonitization increases towards higher structural levels where the rocks are partly overprinted by SSE-vergent chevron and kink folds (Schneider et al., 2018). Deformation is exhibited by stretched quartz grains and fine-grain white mica ribbons that define the main foliation in thin section. Quartz also displays bulging grain boundaries indicating temperatures and pressures consistent with the greenschist facies metamorphic assemblage of Ms-Chl-Ab±Bt (Figure 4). At the uppermost exposed structural level of Athinios, the rocks are strongly overprinted by low-angle brittle-ductile shear zones and brittle faults with several centimeter-scale zones of ultracataclasites. This brittle overprint is likely due to proximity to the detachment although the detachment itself was not observed at Athinios (Schneider et al., 2018). The caldera walls of Athinios are composed primarily of mylonitic quartzite, schist, conglomerate, and metabasite with marble interlayers. Outcrops are strongly foliated with a NE-SW foliation and abundant kinematic indicators document a top-to-S directed shear. This foliation was strongest in the most mica-rich rocks whereas quartzite and marble appear to be mylonitic.

Two igneous bodies were mapped within the metasedimentary rocks below the detachment (Schneider et al., 2018). At Athinios, a dacite was exposed halfway up the cliff (Figure 3). Blocky in outcrop, the weakly-foliated dacite exhibits an irregular contact that cross-cuts the foliation of the surrounding metasedimentary rocks. The rock (sample ALS03) is composed of porphyritic plagioclase and quartz with minor amounts of chlorite in a fine-grained matrix of Bt+Ms+Chl+Pl (Figure 4). Previously referred to as an I-type granite (Skaperlis et al., 1992), the texture observed

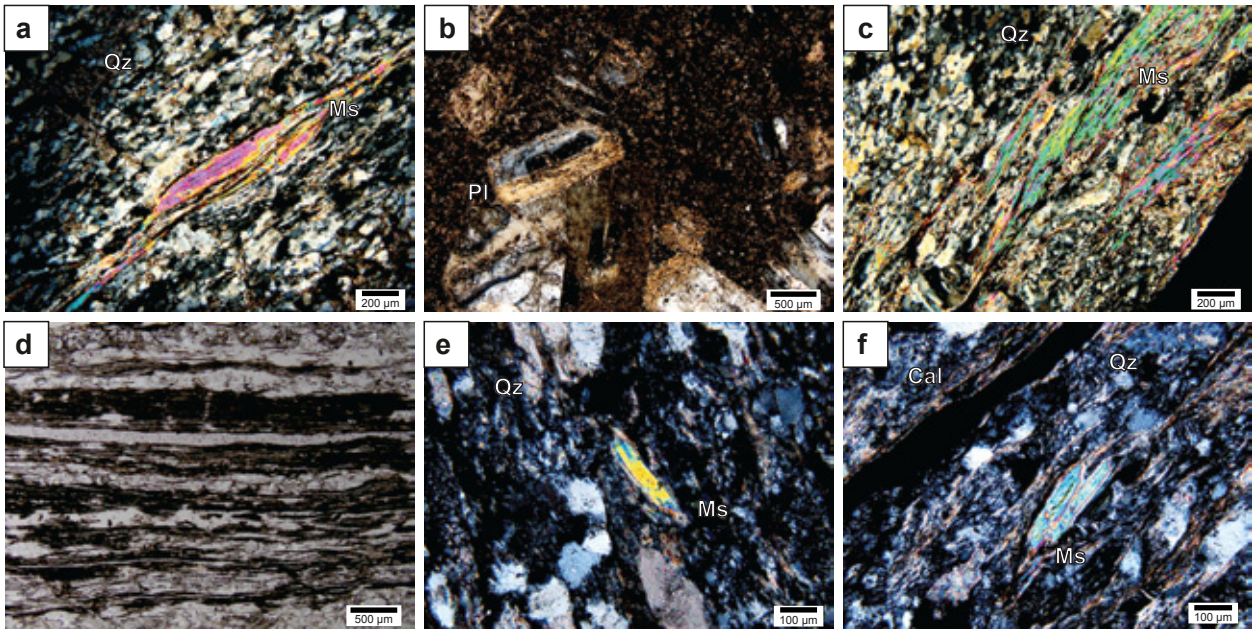

Figure 4: a) Cross polarized thin section photo of quartzite (ALS02) from Athinios demonstration alternating bands of foliation-defining muscovite (Ms) with bulging and stretched quartz grains (Qz). **b**) Cross polarized photo of dacite (ALS03) from Athinios showing porphyritic plagioclase (Pl) in very fine grain matrix of Wm+Bt+Chl+Pl+Qz. **c**) Cross polarized photo of quartzite (ALS08) from Emporio showing similar alternating banding of muscovite (Ms) and stretched and bulging quartz (Qz) as was observed in samples from Athinios. **d**) Plain polarized photo of rhyolite (ALS11) from Emporio showing eutaxitic texture. Remnant flow bands have been altered to fine grained biotite and white mica. **e**) Cross polarized photo of sample ALS17 from saddle of Profitis Ilias showing weakly deformed metasedimentary rock with large, blocky muscovite grain (Ms) which is slightly discordant to foliation. **f**) Cross polarized photo from sample ALS17 from saddle of Profitis Ilias exhibiting weak deformation showing muscovite (Ms) grain possessing thin corroded rim.

in thin section has led the author to classify this granitoid as a dacite. Within the sedimentary units of Emporio is a metamorphosed rhyolite (sample ALS11) that is deformed in a similar manner to the adjacent metasedimentary rocks with well-developed foliation and top-to-SSE shear (Figure 3). The meta-rhyolite possesses muscovite and stretched quartz defining a slightly weaker foliation than the sedimentary samples but with the same Ms-Chl-Ab±Bt greenschist facies mineral assemblage. The rock also contains clasts of proximal sedimentary units, predominantly marble. Relict flow banding (eutaxitic texture) is preserved in thin section whereas the outcrop displays strong to moderately developed schistosity (Figures 3). The sedimentary rocks surrounding the meta-rhyolite are similar in composition to those of Athinios and consist mainly of mica schists and schistose conglomerate with marble interlayers.

Above the detachment system, Profitis Ilias and Mesa Vouno are comprised of weakly-metamorphosed calcitic and dolomitic marble, bounding a metaflysch sequence in the core of a syncline (Schneider et al., 2018). The marble contains well-preserved, large (up to 30 cm) Upper Triassic *Megalodon* fossils and stromatolitic lamination with bird's-eye structures in dolomite layers (Figure 3). The low-grade metaflysch is composed of phyllite, sandstone, and conglomerate (Figure 3) with hectometer-scale chert-bearing marble blocks interpreted to be olistoliths (Schneider et al., 2018). Deformation in the metaflysch is mainly controlled by dissolution-precipitation, and crystal-plastic deformation has only been observed in calcitic marble but not in quartzite components, indicative of temperatures <300°C. The rock package forms a tight, W-vergent synform, which has been superposed into a large-scale fold possessing ESE-dipping fold axes (Schneider et al., 2018). The marble-metaflysch contact was clearly (re)folded but, due to the rheological contrast, ductile shear zones with oblique top-to-SE shear sense localized in the marbles and the metaflysch. The entire hanging wall is deformed by brittle, shallow SE-dipping

faults with top-to-SE kinematics associated with multiple generations of ultracataclasites and polished slip surfaces. A 10 m-thick brittle detachment with multi-generational ultracataclasites is exposed at Monolithos, east of the airport (Schneider et al., 2018). Sub-vertical ENE- and WSW-striking antithetic brittle faults are mechanically linked to subhorizontal slickensides and deform the protocataclastic hanging wall into co-rotating blocks (bookshelves).

The clastic metasedimentary rocks from the saddle of Profitis Ilias appear in thin section to be similar in composition as those from the footwall. At the macroscale, these rocks are much less deformed with muscovite weakly aligned along the foliation planes. The majority of muscovite in thin section was finer grained and weakly aligned in thinly dispersed ribbons. A small subset of large (~100-300 μm) isolated muscovite grains are also present in the rock occurring oblique to the foliation with thin corroded rims. A slight foliation is defined primarily by Qz+Ms ±Chl.

Methodology

Sample preparation

Conventional procedures were used to extract and select the most appropriate minerals from rock samples in preparation for (U-Th)/He, $^{40}Ar/^{39}Ar$ and U-Pb geochronology. Each sample was cleaned with a wire brush and water to remove any surface contamination. The sample was allowed to air dry and was then crushed to a size fraction of ≤1 cm with the use of a standard jaw crusher. The material was then passed through a series of sieves to obtain grain size fractions >250 μm, 63-250 μm and <63 μm. The 63-250 μm fraction was then rinsed through a decantation process to remove any remaining fine powder adhering to the grains and dried for 24 h at a temperature of 30°C using a heat lamp. Heavy mineral separation was then conducted using

methylene iodide (SG: 3.3 g/cm^3 and 2.9 g/cm^3) in order to obtain a more concentrated fraction of zircon and apatite. The heavy mineral separates were then individually passed through a Frantz magnetic mineral separator as needed to further isolate apatite and zircon. White mica was obtained from the >250 µm size fraction using a mortar and pestle to further crush the sample while preserving the integrity of the mica. Samples were sieved to obtain a 150 µm-250 µm size fraction. White mica and zircon grains were then picked using tweezers under a binocular microscope. The samples did not contain sufficient and large, unbroken apatite grains, thus this mineral was abandoned.

Whole rock geochemistry

Samples were first crushed with a jaw crushed then further reduced to fine powder using a ceramic pulverizer. A total of seven samples were powdered, and 20 g of powder of each sample was sent to Acme Labs (Vancouver, Canada) for analysis. Samples were dissolved using a lithium borate fusion with major elements analyzed with ICP-ES and trace elements using ICP-MS. Internal standards and blanks were run along with samples as well as a duplicated analysis for ALS03.

U-Pb geochronology

A JEOL 6610LV Scanning Electron Microscope (SEM; University of Ottawa, Canada) was used to characterize the zircon and to identify the internal structure of the mineral or rim overgrowths on the zircon using cathodoluminescence imaging. A Resonetics M-50 193 nm ArF Excimer laser ablation system coupled to an Agilent 7700x quadrupole ICP-MS system (University of Ottawa, Canada) was utilized for the zircon U-Pb analyses, following the protocol

of McFarlane and Luo (2012) and the common lead correction of Andersen (2002). Single spot analyses were completed with the laser operated at a repetition rate of 6 Hz, spot size of 32 μm, and pulse energy of 4.72 J/cm^2. Reference material 91500 zircon (U-Pb: 1065.4 ± 0.3 Ma; Wiedenbeck et al., 1995) was analyzed as a standard under the same conditions as the unknowns. A secondary standard Plesovice zircon (U-Pb: 337.1 ± 0.4 Ma; Slama et al., 2008) was also used to correct for analytical drift. All data was reduced and drift corrected using Glitter v4.4.4, with reference material uncertainty calibrated to 1%. The final corrected data were plotted using Isoplot v4 (Ludwig, 2012) for both sedimentary and igneous samples. For all results, $^{206}Pb/^{238}U$ ages are reported for ages <1 Ga and $^{207}Pb/^{206}Pb$ ages are reported for ages of >1 Ga. Only the results that were <20% discordant were considered. This is a generous cut off but designed to reduce bias in the dataset (cf. Gehrels, 2012).

$^{40}Ar/^{39}Ar$ geochronology

In conjunction with $^{40}Ar/^{39}Ar$ dating, in situ mineral chemical compositional maps of white mica for a suite of 10 elements (Al_2O_3, FeO, MgO, K_2O, Na_2O, SiO_2, MnO, TiO, Cr_2O_3, and CaO) were determined from all samples using the JEOL JXA-8230 SuperProbe at the University of Ottawa (Ottawa, Canada). Wavelength dispersive spectrometer (WDS) spot analyses were conducted with an accelerating voltage of 20 kV and a beam current of 40 nA using a spot size of 1 μm to create pixel maps up to ~500 x 150 pixels with a 2 μm pixel size and a 200 ms dwell time on each pixel. Cation site distribution was calculated according to Vidal et al. (2001) and Parra et al. (2002). Each map was background corrected using a mean atomic number background correction and each pixel was converted to wt% oxides using a full matrix correction. Following acquisition, the colour spectrum of each map was scaled to highlight the compositional variation

within the mapped muscovite grain using ImageJ open source image processor. ImageJ was also used to extract pixel values to determine composition of muscovite grains.

Once samples were characterized, all $^{40}Ar/^{39}Ar$ analytical work was performed at the University of Manitoba (Winnipeg, Canada) using a multi-collector Thermo Fisher Scientific ARGUS VI mass spectrometer, linked to a stainless steel Thermo Fisher Scientific extraction/purification line and Photon Machines (55 W) Fusions 10.6 CO_2 laser. Argon isotopes (from mass 40 to 37) were measured using Faraday detectors with low noise 1 x 10^{12} Ω resistors and mass 36 was measured using a compact discrete dynode detector. The sensitivity for argon measurements is ~6.312 x 10^{17} moles/fA as determined from measured aliquots of Fish Canyon Sanidine (Dazé et al., 2003, Kuiper et al., 2008).

Standards and unknowns were placed in 2 mm deep wells in 18 mm diameter aluminum disks, with standards placed strategically so that the lateral neutron flux gradients across the disk could be evaluated. Planar regressions were fit to the standard data, and the $^{40}Ar/^{39}Ar$ neutron fluence parameter, J, interpolated for the unknowns. Uncertainties in J are estimated at 0.1-0.2% (1s), based on Monte Carlo error analysis of the planar regressions (Best et al., 1995). All specimens were irradiated in the cadmium-lined, in-core CLICIT facility of the Oregon State University TRIGA reactor. The duration of irradiation was 12 h and using the Fish Canyon sanidine (Kuiper et al., 2008) and GA1550 biotite (Spell and McDougall, 2003) standards.

Irradiated samples were placed in a Cu sample tray, with a KBr cover slip, in a stainless steel high vacuum extraction line and baked with an infrared lamp for 24 h. Single crystals were either fused or step-heated using the laser, and reactive gases were removed, after ~3 min, by three GP-50 SAES getters (two at room temperature and one at 450°C) prior to being admitted to an ARGUS VI mass spectrometer by expansion. Five argon isotopes were measured simultaneously

over a period of 6 min. Measured isotope abundances were corrected for extraction-line blanks, which were determined before every sample analysis. Line blanks averaged ~5 fA for mass 40 and ~0.022 fA for mass 36.

Mass discrimination was monitored by online analysis of air pipettes which during two separate sessions, gave mean values of D: 1.0063 ± 0.0001 and D: 1.0089 ± 0.0005 per amu, based on 67 aliquots interspersed with the unknowns. A value of 295.5 was used for the atmospheric $^{40}Ar/^{36}Ar$ ratio (Steiger and Jäger, 1977) for the purposes of routine measurement of mass spectrometer discrimination using air aliquots, and correction for atmospheric argon in the $^{40}Ar/^{39}Ar$ age calculation. Corrections are made for neutron-induced ^{40}Ar from potassium, ^{39}Ar and ^{36}Ar from calcium, and ^{36}Ar from chlorine (Roddick, 1983, Renne et al., 1998, Renne and Norman, 2001).

(U-Th)/He geochronology

After mineral separation and selection, the analytical portion of the low-temperature geochronological experiments was conducted at the Thermochronology Research and Instrumentation Laboratory (TRaIL) (U-Th)/He facility at the University of Colorado (Boulder, USA). Individual mineral grains are handpicked using a Leica M165 binocular microscope equipped with a calibrated digital camera and capable of both reflected and transmitted, polarized light. The grains were screened for quality, including crystal shape and the presence of inclusions. The dimensions of the crystals are measured and converted to equivalent spherical radius (ESR) as this value is more readily incorporated into the equations that govern the diffusion of He throughout the grain; from this point forward in the paper references to grain size are measurements of ESR. After characterization, grains are placed into small Nb tubes that are then

crimped on both ends. This Nb packet is then loaded into an ASI Alphachron He extraction and measurement line. The packet is placed in the UHV extraction line (~$3x10^{-8}$ torr) and heated with a diode laser to ~800-1100°C for 5 to 10 m to extract the radiogenic ^{4}He. The degassed ^{4}He is then spiked with approximately 13 ncc of pure ^{3}He, cleaned via interaction with two SAES getters, and analyzed on a Balzers PrismaPlus QME 220 quadrupole mass spectrometer. Degassed grains are then removed from the line, and taken to a Class 10 clean lab for dissolution. Apatite grains, still enclosed in the Nb tubes, are placed in 1.5 mL Cetac vials, spiked with a ^{235}U-^{230}Th tracer in HNO_3, capped, and baked in a lab oven at 80°C for 2 h. Zircon are dissolved using Parr large-capacity dissolution vessels in a multi-step acid-vapor dissolution process. Grains (including the Nb tube) are placed in Ludwig-style Savillex vials, spiked with a ^{235}U-^{230}Th tracer, and mixed with 200 µl of Optima grade HF. The vials are then capped, stacked in a 125 mL Teflon liner, placed in a Parr dissolution vessel, and baked at 220°C for 72 h. After cooling, the vials are uncapped and dried down on a 90°C hot plate until dry. The vials then undergo a second round of acid-vapor dissolution, this time with 200 µl of Optima grade HCl in each vial that is baked at 200°C for 24 h. Vials are then dried down a second time on a hot plate. Once dry, 200 µl of a 7:1 HNO_3:HF mixture is added to each vial, the vial is capped, and cooked on the hot plate at 90°C for 4 h. Once the minerals are dissolved, regardless of the dissolution process, they are diluted with 1 to 3 mL of doubly-deionized water, and taken to the ICP-MS lab for analysis. Mineral standards of Durango apatite (31.5 Ma) and Fish Canyon Tuff zircon (28.2 Ma) are routinely analyzed (degassed and dissolved) in conjunction with the samples with each run to ensure data integrity. Sample solutions, along with standards and blanks, are analyzed for U, Th, and Sm content using a Thermo Element 2 magnetic sector mass spectrometer. Once the U, Th, and Sm contents have

been measured, He dates and all associated data are calculated on a custom spreadsheet made by TRaIL staff.

Analytical Results

Whole Rock Geochemistry

Major and trace element geochemistry was performed on seven samples in order to determine the chemistry of the igneous samples and to compare the sedimentary units across the detachment. A summary of major elements is in Table 1 with full results in Appendix A. Spider plot of REE elements for all samples (Figure 5) and a discrimination diagram for igneous samples (Figure 6) were also produced. Samples ALS02 (quartzite) and ALS05 (conglomerate) were chosen from Athinios as they were the two most prevalent rock types. As expected for a quartzite, ALS02 was dominantly composed of SiO_2 with high CaO due to interlayers of calcite. In the case of ALS05, only schistose material from the matrix of the conglomerate was used for the geochemical analysis (Table 1). ALS08 (quartzite) was the only sedimentary sample chosen from Emporio which, similar to the other quartzite, is dominantly composed of SiO_2. All three of these samples show relative enrichment in light rare earth elements (REE) with negatively sloped profiles which tapers to a relatively flat trend of heavy REE (Figure 5). There also appears to be a negative Eu anomaly across all samples. ALS13, a conglomerate, and ALS17, a phyllite, were collected from within the saddle of Profitis Ilias, with ALS13 sampled from the bottom of the saddle near Perissa and ALS17 collected near the top of the saddle. Both were relatively enriched in Fe_2O_3, Al_2O_3, K_2O and MgO compared to sedimentary samples from the footwall (Table 1). However, these two samples follow the same REE trend as the sedimentary samples from the

Table 1. Major (wt%) oxide element data for rocks from Thera (Santorini), Greece

Sample	ALS02	ALS03a	ASL05	ALS08	ALS11	ALS13	ALS17
	quartzite	dacite	conglomerate	quartzite	meta-rhyolite	conglomerate	phyllite
SiO_2	83.35	68.56	73.28	91.81	52.27	52.56	65.30
Al_2O_3	3.69	14.59	3.45	3.58	5.15	7.01	12.88
Fe_2O_3	1.63	1.98	2.10	1.39	2.11	2.96	5.56
MgO	0.32	1.32	0.72	0.59	0.56	2.00	4.15
CaO	4.71	2.53	9.93	0.18	20.15	17.07	1.80
Na_2O	0.04	1.80	0.42	0.14	1.32	0.95	1.71
K_2O	0.93	5.18	0.61	0.86	0.70	1.20	2.42
TiO_2	0.31	0.29	0.29	0.24	0.32	0.29	0.63
P_2O_5	0.03	0.08	0.05	0.05	0.09	0.07	0.11
MnO	0.07	0.05	0.05	0.02	0.05	0.14	0.07
Cr_2O_3	0.00	0.01	0.00	0.00	0.01	0.03	0.04
LOI	4.80	3.40	9.00	1.10	17.20	15.60	5.10
Sum	99.96	99.89	99.95	99.98	99.92	99.91	99.86

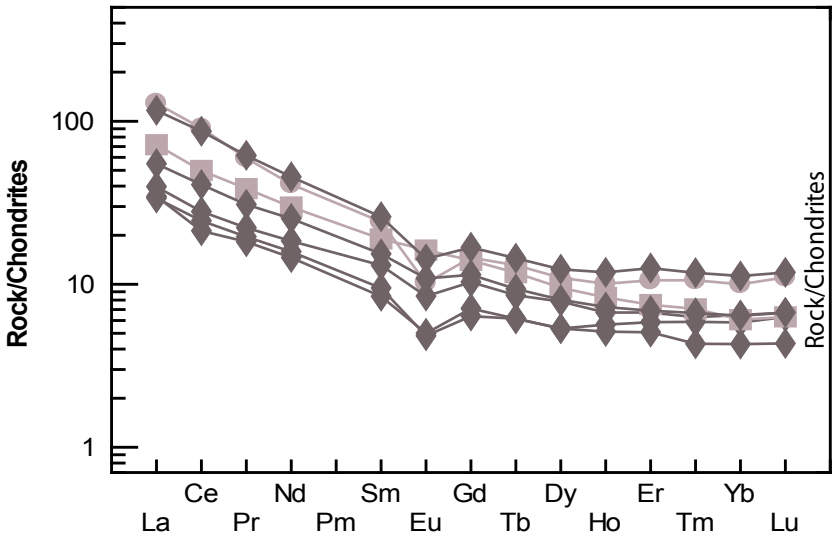

Figure 5: REE plot normalized to chondrite values based on Sun and Mcdonough (1989). Sedimentary samples are shown by dark grey diamonds while light grey circle (ALS03) and square (ALS11) correspond to the two igneous samples. Both sedimentary and igneous samples all follow similar trend with slight enrichment in LREE and relatively flat HREE profile. See Table 1 and Appendix A for analytical data.

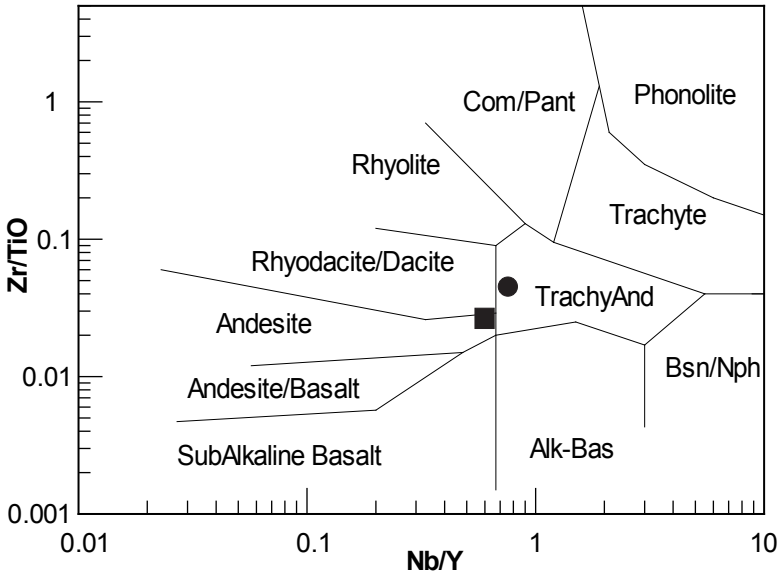

Figure 6: Zr/TiO vs. Nb/Y discriminant diagram based on Winchester and Floyd's (1977) classification of igneous rocks. ALS03 dacite (circle) falls on line separating dacite and trachyandesite and has been referred to as a dacite due to texture observed in thin section. ALS11 meta-rhyolite (square) lies just within the andesite boundary but has been referred to as a rhyolite. This is primarily due to two reasons; textural similarities to similar aged rhyolites in Driovouno (Anders et al., 2007) and due to the high amount of clastic material within the rhyolite in outcrop which may have contaminated the geochemical signature of the rhyolite.

footwall (Figure 5). ALS13 also had elevated (17 wt%) CaO as it contained interlayers calcitic marble.

The two igneous samples ALS03 (dacite) from Athinios and ALS11 (meta-rhyolite) from Emporio were classified according to the Nb/Y vs. Zr/Ti diagram (Figure 6) of Winchester and Floyd (1977). The dacite (circle) appears within the trachyandesite field near the border of rhyolite/dacite. ALS11 (square) was seen to diverge from the rhyolite field and instead occurs much lower on the diagram straddling the andesite and dacite fields. The igneous samples followed a similar REE trend as the sedimentary samples although they are less steeply sloping with less tapered HREE profiles. In the case of ALS03, the HREE form a slight positive slope.

U-Pb zircon geochronology

In order to determine sediment provenance and detrital age signatures, six metasedimentary rock samples were collected for detrital zircon geochronology. Complete analytical results are available in Appendix B with sample locations present in Figure 2; Figure 7 presents a small subset of representative CL images for each sample with complete sample images available in Appendix C and Figure 8 highlights detrital zircon populations from analysis. In addition, two igneous rock bodies (ALS03, ALS11) from within the footwall of the detachment were sampled to determine their crystallization age (Figure 9), which will further help with tectonostratigraphic correlations.

Below the detachment, two samples from Athinios (ALS02, ALS05) and one sample from Emporio (ALS08) were used for detrital U-Pb dating. A set of 98 zircon grains were sampled from ALS02, a mylonitic quartzite. Grains were rounded to elongate with lengths varying between 100-250 μm (length: width ratio 1:1 to 3:1) and oscillatory zoning occurs in less than half of zircon analyzed (Figure 7). Zircon U-Pb ages range from 3570-29 Ma, with the dominant age population

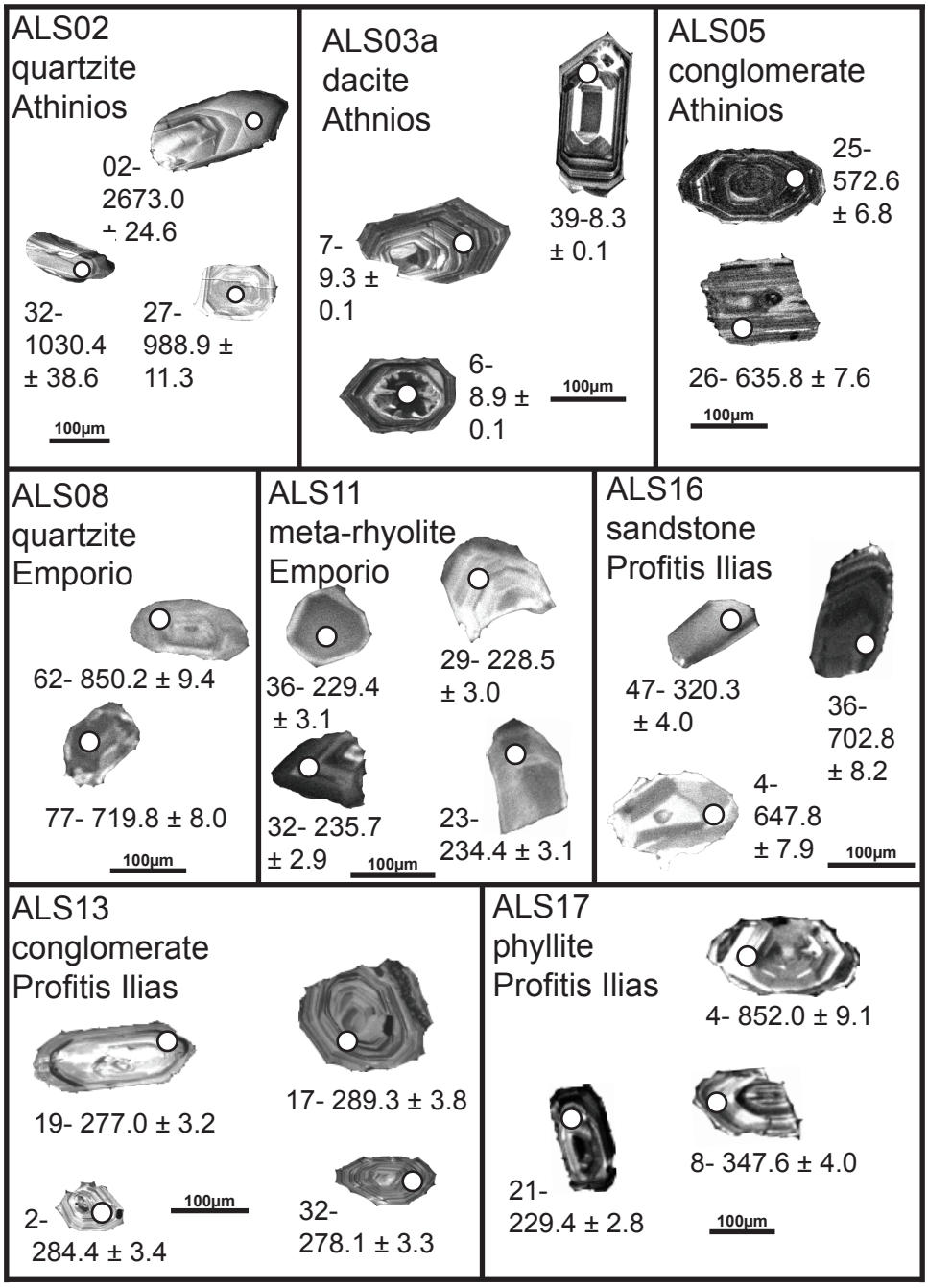

Figure 7: Representative zircon grains for each sample analyzed for U-Pb geochronology by LA-ICP-MS. Zircon grains were imaged using Cathode Luminescence (CL) via a scanning electron microprobe (SEM) with laser spot locations (white circles) and resultant ages. See Appendix C for full sample CL images.

occurring at ca. 634 Ma with 23 grains yielding ages between 655-590 Ma. Minor peaks occur at ca. 980 and ca. 2520 Ma (Figure 8). Two grains yielded ages of ca. 29 Ma but did not vary in their physical properties from the other zircon analyzed. Th/U values ranged from 0.01-2.19 with the majority of grains having values between 0.25-0.70.

A set of 62 zircon were taken from the matrix of metaconglomerate ALS05. The zircon are equant to rounded in shape and typically 100-200 μm long (length: width ratio of 1:1 to 2:1; Figure 7). U-Pb analyses yielded ages ranging from 2630-28 Ma and the predominant population occurs at ca. 640 Ma with lesser peaks at ca. 750, 905 and 2485 Ma (Figure 8). One grain yielded an age of 28 Ma with the next youngest zircon grain at an age of 357 Ma. This young grain was more prismatic in morphology and slightly larger (~300 μm) than the rest of the sample set. The Th/U values vary between 0.01-1.5 with only two analyses providing values greater than 1.0, which give relatively old ages of 1080 and 2096 Ma.

Sample ALS08, a quartzite, was the only sedimentary sample from Emporio used for detrital U-Pb analysis. The zircon are mostly rounded, equant grains that are 100-200 μm long (length: width ratio of 1:1 to 2:1) with oscillatory zoning common (Figure 7). A set of 100 zircon grains yielded ages between 2712-526 Ma with one grain giving an age of 28 Ma. A dominant age population occurs at ca. 600 Ma with subordinate peaks occurring at 750 and 998 Ma (Figure 8). Th/U values range between 0.02-2.85 with the only two grains giving values greater than 2.0, which had U-Pb ages of 651 and 2712 Ma.

Three sedimentary samples were taken from above the detachment within the topographic saddle of Profitis Ilias for U-Pb dating: ALS13, ALS16 and ALS17 (Figure 2). A set of 96 zircon grains were analyzed from the matrix of metaconglomerate sample ALS13. Zircon grains are prismatic to rounded that are 100-250 μm long (length: width ratio of 1:2 to 1:3) with majority of

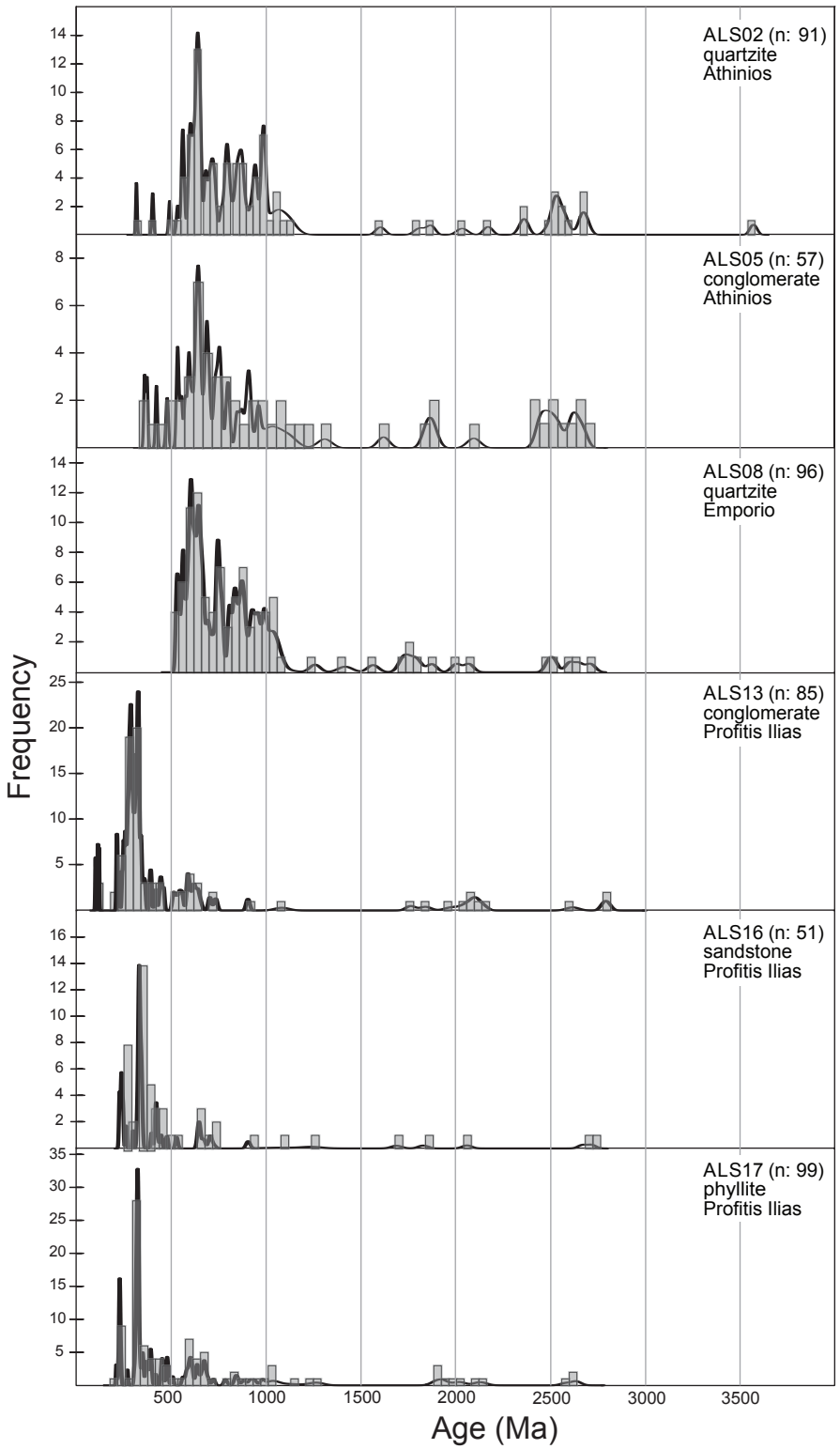

Figure 8: Probability density diagrams of LA-ICP-MS detrital single grain zircon U-Pb analysis data from metasedimentary rocks of Thera. Samples from the footwall (upper three samples) show dominant Pan-African (>500 Ma) signature, whereas samples in hanging wall (lower three) dominated by ca. 240 Ma age peak. See map (figure 2) for locations and Appendix B for analytical data.

grains featuring oscillatory zoning (Figure 7). Zircon yielded ages between 2750-99 Ma with a single analysis giving an age of 28 Ma. The dominant population occurs at ca. 320 Ma with a subordinate population occurring at 580 Ma and a small subset of six grains giving ages between 120-99 Ma (Figure 8). Th/U values vary between 0.02-1.75 with the youngest seven grains having Th/U values between 0.35-0.80.

Sample ALS16, a weakly metamorphosed sandstone, was sampled from the upper section of the saddle. Zircon grains were rounded to elongate in shape and typically 100-200 μm long (length: width ratio of 1:1 to 2:1) with rare oscillatory zoning present (Figure 7). A set of 52 zircon yielded ages between 2710-150 Ma with the dominant population occurring at ca. 330 Ma with subordinate populations at 240 and 420 Ma (Figure 8). Th/U values vary between 0.07-1.00 with two grains having values of 1.64 and 10.10, yielding ages of 151 and 1081 Ma, respectively.

A phyllite sample (ALS17) was taken from the top of the saddle of Profitis Ilias. Zircon grains are mostly prismatic and ~200 μm in length (length: width ratio of 2:1) with common oscillatory zoning (Figure 7). A set of 112 zircon yielded ages between 2660-210 Ma with the dominant population occurring at ca. 324 Ma with subordinate peaks at 230 and 600 Ma (Figure 8). Th/U values vary between 0.04-1.88.

For additional stratigraphic constraints, two igneous samples were also dated. Dacite sample ALS03 was sampled from amongst the cliff face overlooking Athinios harbor (Figure 2). Zircon are subhedral and prismatic and between 100-300 μm long (length: width ratio of 1:1 to 3:1). Most zircon also possess concentric internal structure characteristic of igneous zircon (Figure 7). A total of 26 analyses were conducted, the eighteen most concordant grains yielded a weighted mean $^{206}Pb/^{238}U$ age of 8.52 ± 0.17 Ma (MSWD: 7.1) and a Concordia intercept of 8.62 ± 0.33 Ma

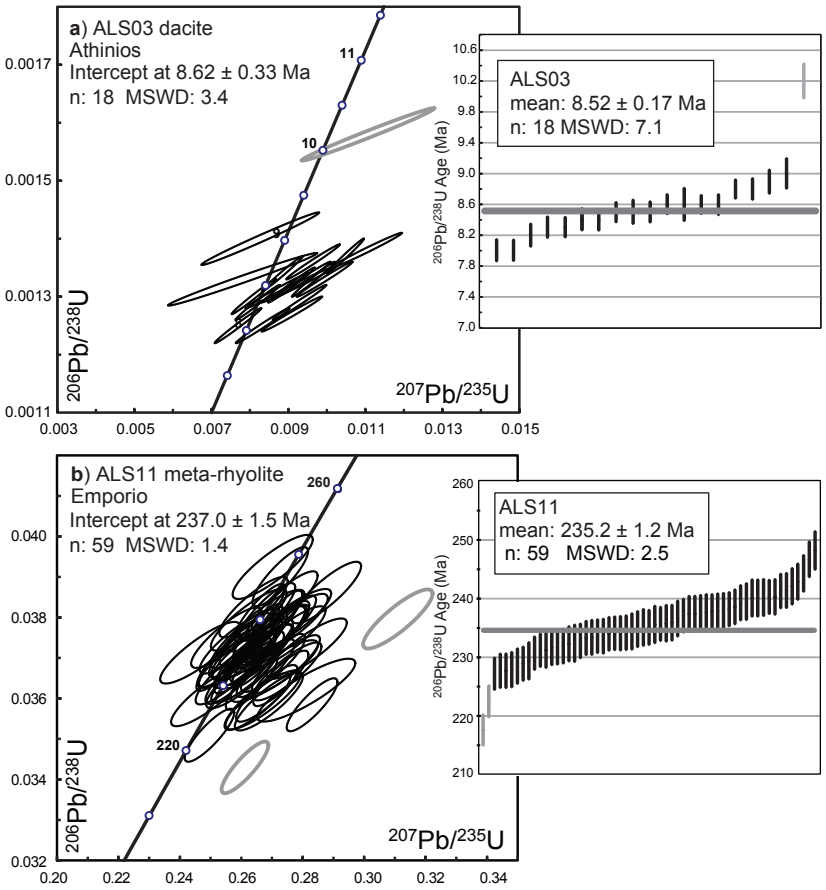

Figure 9: LA-ICP-MS zircon U-Pb data from a) meta-rhyolite and b) dacite. Ages reported on Concordia and weighted average diagrams at 1 sigma. Grey analyses were not used in calculations. Sample ALS11 meta-rhyolite is at the top of the CBU stratigraphic package near Emporio, and sample ALS03 is a dacite that is exposed within the CBU near Athinios. See map (figure 2) for locations and Appendix B for analytical data.

(MSWD: 3.4, Figure 9). Th/U values range from 0.19-0.85 with a single inherited grain providing an age of 312 Ma.

A meta-rhyolite (ALS11) was sampled from Emporio (Figure 2). Zircon show rounded and fractured morphology with most grains containing concentric zoning with sizes ranging from 50-150 μm (length: width ratio of 1:1; Figure 7). Zircon U-Pb data from the meta-rhyolite yielded a dominant Triassic signature with two-thirds of the analyses giving ages between 249-217 Ma and a weighted mean $^{206}Pb/^{238}U$ age of 59 concordant analyses of 235.2 ± 1.2 Ma (MSWD: 2.5) and a Concordia intercept of 237.0 ± 1.5 Ma (MSWD: 1.4; Figure 9). The remaining analyses range from ca. 3437-540 Ma and possess a similar distribution as the nearby sedimentary samples (Figure 8). Th/U values range from 0.01-1.5.

$^{40}Ar/^{39}Ar$ white mica geochronology

Multiple single-grain fusion $^{40}Ar/^{39}Ar$ dating was conducted as a quick and efficient means to assess the range of bulk grain ages in samples from Santorini. The key advantage of this approach is that it constrains age heterogeneity within a sample and, at larger scales, by taking multiple samples from across the pre-volcanic rocks. Sample locations are shown in Figure 2 and results highlighted in Figure 10 with complete results available in Appendix D. Compositional maps were generated for five samples from representative white mica grains, highlighted in Figure 11, with all maps available in Appendix E. Compositional data is also plotted on a ternary diagram to determine mica chemistry (Figure 12) with results presented in Table 2.

Up to eleven single muscovite grains from each of the seven samples across the island (Figure 10) were dated via the total fusion method to resolve the timing of deformation of Thera. The same two meta-sedimentary units (ALS02, ALS05) from Athinios that were dated using the

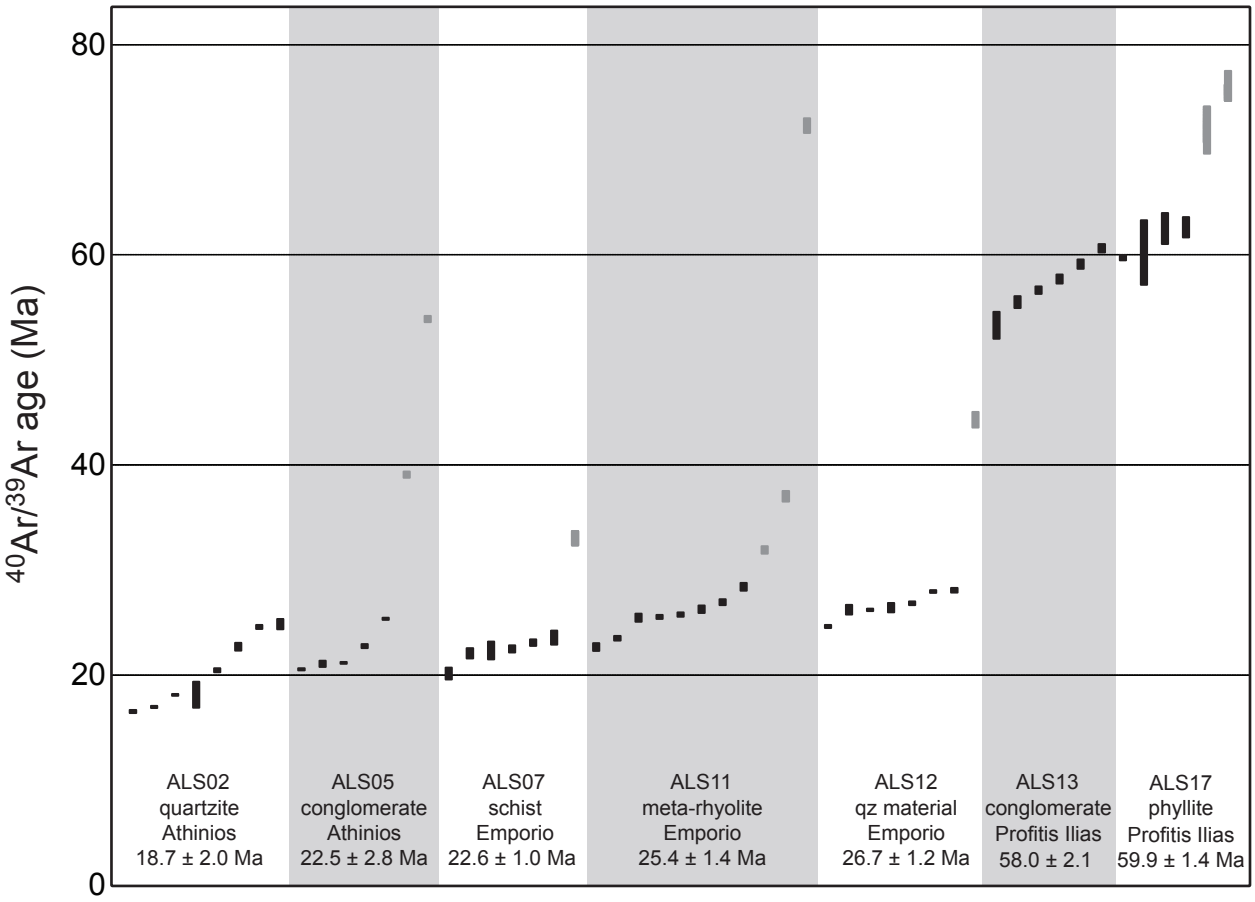

Figure 10: Weighted average 40Ar/39Ar age diagram of single grain muscovite analyses from seven samples across Santorini, sample names and weighed averages are at the bottom of each column. Analyses in grey were not used in the calculation of the weighted average sample age; see map (Figure 2) for locations. Not shown are three analyses with weighted average of 225 Ma from ALS05 and two analyses of 198 and 131 Ma from sample ALS17. Sample ALS12 taken from quartzitic material within marble. See Appendix D for analytical data.

U-Pb technique were also chosen for $^{40}Ar/^{39}Ar$ dating. The muscovite chosen for analysis were derived from bands of foliation-defining muscovite (Figure 4). The single-grain fusion $^{40}Ar/^{39}Ar$ dating technique necessitated using muscovite grains of at least 150 µm in size with no grain exceeding 500 µm although the average grain was much closer to ~200 µm. To determine white mica composition, two grains from both ALS02 and ALS05 were selected to generate compositional maps (Figure 11, Appendix E). The chemical data illustrates Tschermak and pyrophyllitic substitutions (Figure 12), suggesting a dominantly homogeneous muscovite chemistry. A total of 18 grains between the two samples were analyzed with the ages ranging from 54-16 Ma with weighted averages of 18.7 ± 2.0 and 22.5 ± 2.8 Ma from ALS02 and ALS05, respectively (Figure 10). Two grains, both from ALS05, returned dates of 54 and 39 Ma but were not regressed into the weighted averages, and three grains, also in ALS05, yielded a weighted average age of 225.9 ± 2.9 Ma and were treated as their own population. These are likely partially reset and detrital components, respectively.

Muscovite from two samples, ALS07 (mica schist) and ALS11 (meta-rhyolite), were analyzed from Emporio. As with the samples from Athinios, these muscovite grains were derived from foliation-defining bands of mica. A total of seven grains were analyzed from ALS07 and eleven grains from ALS11 giving sample weighted average ages of 22.6 ± 1.0 and 25.6 ± 1.3 Ma, respectively (Figure 10). One grain from ALS07 returned a date of 33 Ma and three grains from ALS11 returned dates of 32, 37 and 72 Ma, which were not regressed into the averages. No grains from ALS07 were selected to generate compositional maps, however a muscovite grain from the proximal ALS08 was mapped as a proxy as were two grain maps from ALS11 (Figure 11, Appendix E). As with previous samples, two muscovite grains, one from ALS08 and ALS11, were seen to be compositionally homogeneous with thin alteration halos along grain edges. One grain

ALS11-1 contains elevated NaO and SiO_2 and low Al_2O_3 compared to other grains while also possessing low concentrations of K_2O. This single grain was determined to be compositionally paragonite and was the only grain observed that did not reside in the muscovite composition field (Figure 12).

Sample ALS12 was taken from quartzitic material contained within the marble of the quarry on the western edge of Profitis Ilias, which contained the observed *Megalodon* fossils. The material from which this sample was taken was a few tens of meters stratigraphically above the footwall. As such, this sample was dated in an effort to determine the timing of the detachment. A total of eight grains were analyzed, returning dates ranging from 28-24 Ma yielding a weighted average age of 26.7 ± 1.2 Ma, a slightly older age than samples from Athinios (Figure 10). One grain returned a date of 44 Ma which was not regressed into the average. No compositional maps were generated for this sample as it was not possible to cut a thin section due to the disjointed nature of the sample.

Two samples (ALS13, ALS17) from the saddle of Profitis Ilias were chosen for $^{40}Ar/^{39}Ar$ analysis. The six grains analyzed from ALS13 returned dates ranging from 61-53 Ma with a weighted average age of 58.0 ± 2.1 Ma (Figure 10). In ALS17, eight grains were analyzed with six of the grains returning dates ranging from 76-60 Ma and the four youngest grains giving a weighted average age 59.9 ± 1.5 Ma (Figure 10). Two grains returned much older ages of 131 and 198 Ma. Although no compositional maps were generated for ALS13, five maps were generated for ALS17, all of which show homogeneous grains with thin altered rims, with the grains being chemically consistent with muscovite (Figure 11, Appendix E).

Table 2. Major element (wt%) data from analysis of white mica from Thera (Santorini), Greece

Sample	SiO_2	Na_2O	K_2O	FeO	Cr_2O_3	MgO	CaO	Al_2O_3	MnO	TiO	Total
ALS02-1	43.65	1.01	10.60	1.48	0.07	0.82	0.01	33.39	0.01	0.86	91.88
ALS02-2	45.37	0.41	10.23	1.33	0.07	1.18	0.00	34.02	0.00	0.85	93.47
ALS05-1	44.09	1.41	8.95	1.40	0.09	0.73	0.00	35.78	0.29	0.91	93.65
ALS05-2	42.75	0.47	10.48	2.08	0.09	0.61	0.00	34.32	0.10	0.82	91.73
ALS08-1	47.98	0.23	8.65	1.86	0.00	2.96	0.00	26.73	0.01	0.14	88.57
ALS11-1	66.48	12.00	0.00	0.14	0.01	0.00	0.00	19.44	0.00	0.01	98.09
ALS11-2	47.49	0.12	10.26	4.54	0.00	2.14	0.00	26.93	0.00	0.04	91.52
ALS17-1	46.93	0.64	9.27	1.78	0.08	2.76	0.01	28.29	0.00	0.41	90.17
ALS17-2	47.36	0.35	11.03	3.57	0.05	2.12	0.00	27.22	0.00	0.27	91.97
ALS17-3	47.36	1.25	9.85	4.00	0.04	1.93	0.00	27.71	0.10	0.48	92.71
ALS17-4	44.79	0.66	10.19	4.09	0.12	1.30	0.00	28.58	0.19	0.17	90.09
ALS17-5	48.58	0.64	9.64	2.66	0.00	2.14	0.00	28.69	0.10	0.40	92.85

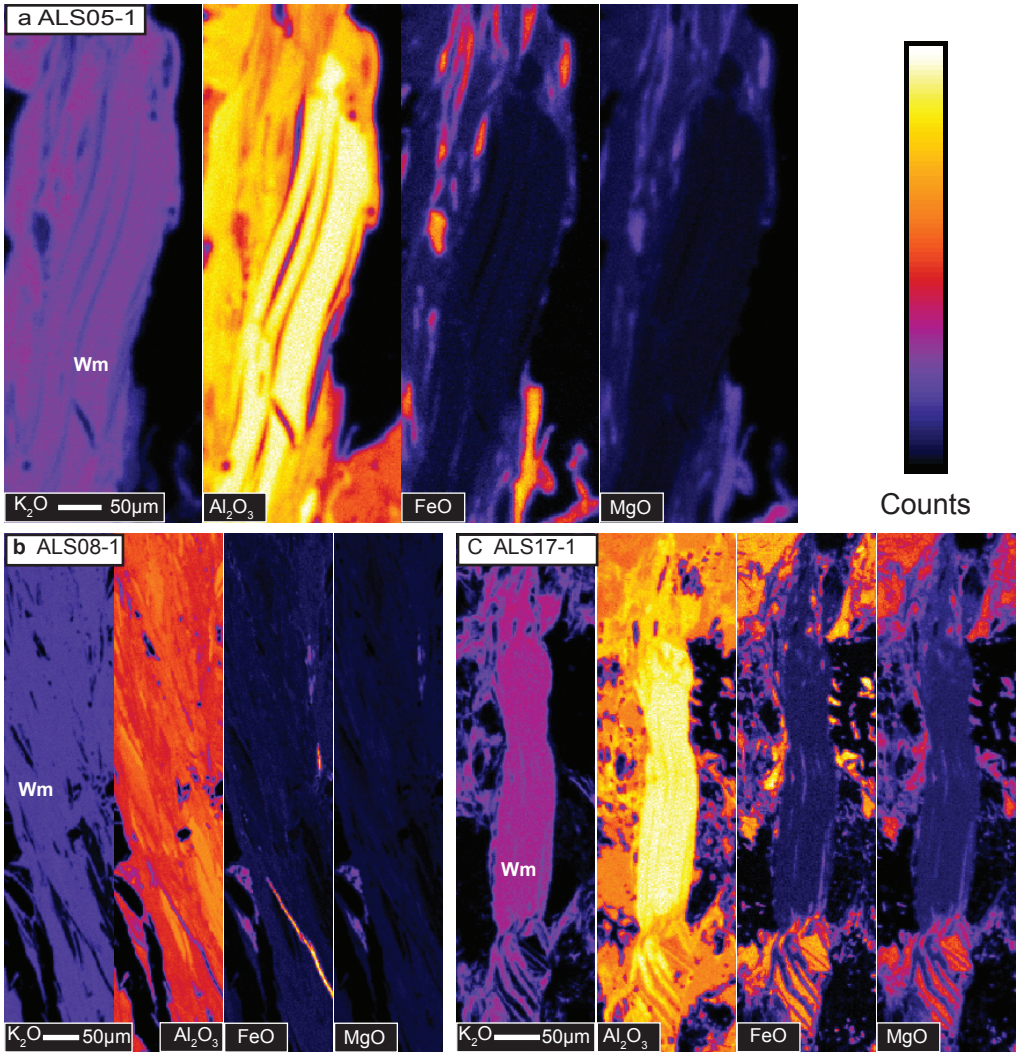

Figure 11: Representative WDS chemical maps of select muscovite grains from samples from Santorini. Elemental K2O, Al2O3, FeO and MgO maps from one sample from **a**) Athinios (ALS02), **b**) Emporio (ALS08) and **c**) Profitis Ilias (ALS17) are shown with additional maps in appendix E. Cool colors are low concentrations and warm colors are higher concentrations. Chemical maps show minor depletion in most elements near rim of muscovite grains with the interior of the grains being relatively homogeneous. See Table 2 for analytical results and Appendix E for additional WDS chemical maps.

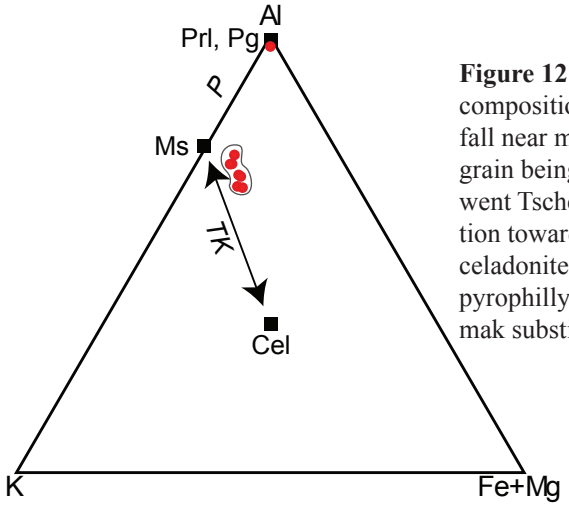

Figure 12: Ternary diagrams of all white mica that were used for WDS compositional maps, see Table 2 for compositional data. Majority of grains fall near muscovite field along the line of Tschermak substitution with one grain being compositionally paragonite, position indicates grains underwent Tschermak substitution, evolving from phengite/celadonite composition towards muscovite. Abbreviations are as follows: Al: aluminum, Cel: celadonite, Fe + Mg: iron+magnesium, K: potassium, Ms: muscovite, P: pyrophillytic substitution, Pg: paragonite, Prl: pyrophyllite, TK: Tschermak substitution. See Table 2 for analytical results.

(U-Th)/He geochronology

The (U-Th)/He system in zircon is a useful tool for analyzing low temperature deformation of an area. The system records crustal cooling at temperatures through the ~180°C isotherm with the exact closure temperature varying on grain size, cooling rates and radiation damage (Reiners et al., 2002, 2004, Harrison and Zeitler, 2005). This system is particularly useful in documenting the low temperature brittle deformational history or shallow crustal unroofing experienced by a package of rocks. For all samples selected for (U-Th)/He thermochronology, the most euhedral, prismatic and inclusion-free zircon were chosen from among the heavy mineral separate for analysis as lattice defects and inclusion can affect the apparent ages (Reiners et al., 2002, 2004). Sample results are highlighted in Figure 13 with complete results available in Appendix F. The three samples from Athinios that were processed for $^{40}Ar/^{39}Ar$ and U-Pb dating were also utilized for (U-Th)/He geochronology (Figure 2). Six zircon from ALS02 (quartzite) were analyzed yielding ages between 10.9-7.8 Ma with a weighted average age of 8.7 ± 1.2 Ma (Figure 13). Grains were clear, semi-rounded to fragments of prismatic grains, 130-200 μm in length and relatively inclusion free with the exception of a few small inclusions in three of the six grains.

Six grains were also analyzed from sample ALS03 (dacite) to determine the difference in crystallization (U-Pb) and cooling ((U-Th)/He) ages and to calculate the rate at which the footwall cooled. Grains yielded ages ranging from 7.8-6.9 Ma with a weighted average of 7.3 ± 0.4 Ma (Figure 13). The zircon were clear, prismatic and euhedral, 160-260 μm in length and relatively free of inclusions.

Eight grains were analyzed from the schistose matrix of ALS05 (conglomerate) with ages ranging from 7.8-6.9 Ma giving a weighted average of 7.7 ± 0.5 Ma (Figure 13). Grains were semi-clear, rounded to stubby, 135-195 μm in length with some grains possessing small inclusions.

ALS08 (quartzite) was the only sample from Emporio to be dated via (U-Th)/He methods. Six zircon yielded a weighted mean age of 11.0 ± 1.7 Ma with ages ranging from 13.2-9.2 Ma (Figure 13). Grains were clear, stubby to elongated, 160-275 μm in length and mostly free of inclusions.

Samples ALS13 and ALS17 were chosen from the saddle within Profitis Ilias. Eight zircon grains were analyzed for each, producing a weighted age average of 17.3 ± 1.5 Ma for ALS13 with ages ranging from 21-15.1 Ma (Figure 13). Grains were clear, rounded to elongated, 125-198 μm in length with most grains containing small inclusions. For ALS17, two age populations were determined with weighted mean ages of 19.0 ± 2.7 and 31.7 ± 6.1 Ma. The older population was slightly smaller in size (136-160 μm) than the younger grains (122-177 μm) but otherwise grains were all stubby to elongate, relatively clear with minor amounts of inclusions. Mean ages for each sample were plotted against effective uranium (eU), a proxy for uranium damage to the crystal lattice, as these two factors largely control He diffusion (Figure 13). Unfortunately no discernable patterns were observed. This likely indicates that these grains did not reside for any extended period of time in the helium partial retention zone (200-120°C) but rather cooled quickly (Reiners 2005, Wolfe and Stockli, 2010).

Discussion

Differences in metamorphic grade, deformation style, detrital zircon age spectra, $^{40}Ar/^{39}Ar$ ages and (U-Th)/He ages revealed the existence of two tectonically different units as proposed by Kilias et al. (1998). These units are separated by a recently discovered detachment fault system (Schneider et al., 2018) exposed north of Emporio. The top-to-S detachment separates the footwall

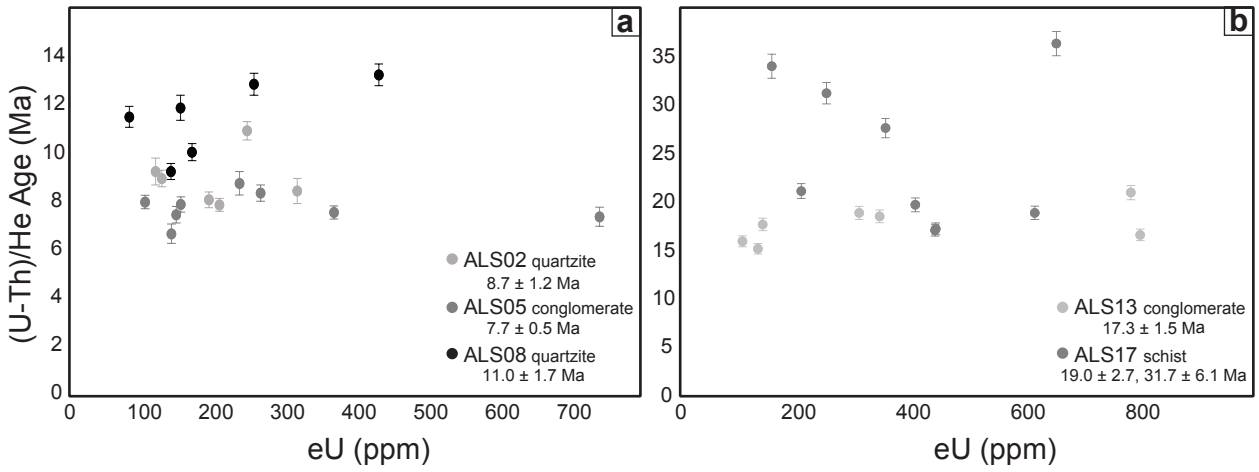

Figure 13: Plot of (U-Th)/He age vs eU (effective uranium) of zircon from samples of the **a**) footwall and **b**) hanging wall. Effective uranium is a proxy measurement for the amount of radiation damage in the crystal lattice of the zircon grain which will affect helium diffusion. The relatively large dispersion in eU values possessing the same date suggests relatively rapid cooling through the partial retention zone. Not pictured is ALS03 (dacite) which had eU values of 1676-3128 ppm and gave a weighted mean age of 7.3 ± 0.4 Ma. High eU values reflect high concentrations of U+Th, however, relatively young ages which correlate to U-Pb crystallization age of 8.5 Ma, remain unaffected. See Appendix F for analytical data.

rocks of Athinios and Emporio from those of Profitis Ilias, which compose the hanging wall (Figure 2). Below, the distinguishing characteristics between these two units are discussed.

Footwall Rocks of Athinios and Emporio

Basement ages and tectonostratigraphy

Detrital zircon U-Pb ages from rocks in the footwall can be correlated with packages of rocks on Milos, Folegandros, Naxos, Paros, Ios, Sifnos, Syros, Sikinos, Crete and the Peloponnese, whereby an African provenance for the sediments has been demonstrated (Keay and Lister, 2002; Photiades and Keay, 2003; Marsellos et al., 2012; Zulauf et al., 2015). These datasets show several prominent populations of detrital ages notably ca. 550-650, 800-1000, 2000-2050, 2450-2500 Ma, and a paucity of analyses between 1000-1600 Ma, which can be linked to large magmatic events on the Pan-African continent. The study of Marsellos et al. (2012) in particular featured one sample from Athinios on Thera with pre-Carboniferous detrital ages (n: 24). Detrital zircon results from this current study (Figure 8) correlate with published results: 95% of data are pre-Carboniferous dates with the predominant age population across all three footwall samples occurring between 600-650 Ma, with subordinate peaks at 750, 900-1000 and 2450-2550 Ma. The youngest single zircon detrital age of ca. 314 Ma with the next two youngest (357 Ma, 370 Ma) can be used as an indicator for the maximum age of deposition of the sediments, which would indicate the sediments are likely Carboniferous in age. This is consistent with most of the data reported from the Cycladic islands north of Thera (Keay and Lister, 2002; Photiades and Keay, 2003; Marsellos et al., 2012), and illustrates a strong tectonostratigraphic connection. A Carboniferous age has been attributed to the CBU, whereas the PQU is considered to be late-Carboniferous to Triassic (Anders et al., 2007; Bröcker and Pidgeon, 2007; Jolivet and Brun, 2010; Marsellos et al., 2012). Therefore, based

on the age spectra and the maximum depositional age, the footwall rocks of Thera are equivalent to the Cycladic Blueschist Unit.

The meta-rhyolite dated in this study at 235.2 ± 1.2 Ma (Figure 9) is analogous to volcanic units intercalated in the CBU on other islands such as Andros, Ios and Sifnos, as well as on continental Greece yielding ages between 245-237 Ma (Mountrakis et al., 1987; Pe-Piper and Piper, 2002; Anders et al., 2007; Bröcker et al., 2007; Liati et al., 2013). The age of the meta-rhyolite serves to better constrain the age of the footwall sedimentary rocks. As the meta-rhyolite occurs at structurally higher sections of the footwall, in conjunction with detrital zircon U-Pb ages, it serves to further constrain the sediments to Middle Triassic to Carboniferous in age which is consistent is with the CBU elsewhere (Dürr et al., 1978; Ring and Layer, 2003; Jolivet and Brun, 2010; Grasemann et al., 2017).

A detrital zircon study from the western Cyclades (Seman et al., 2017) also illustrates an African provenance for the CBU, although also differentiating between two age distributions of detrital zircon: one with an early Jurassic-Triassic and the other a Cretaceous-Jurassic maximum depositional age. A sample from Folegandros (Photiades and Keay, 2003) also has a Triassic maximum depositional age. The disparity in ages obtained by Seman et al. (2017) in relation to the other studies (Keay and Lister, 2002; Photiades and Keay, 2003; Marsellos et al., 2012) may be related to geometry of the sediment packages within the subduction trench, which are now separated by the Trans Cycladic Thrust (TCT; Figure 1). At Thera, it is unlikely that the rocks of the footwall are analogues of the Upper Cycladic Nappe (UCN) of the CBU as the rocks were not subjected to high metamorphic conditions that characterize the UCN elsewhere (Davis and Bastas, 1978; Skarpelis and Liati 1990; Grasemann et al., 2017). The lack of post-Carboniferous ages in the detrital zircon age spectra from the footwall of Thera may indicate that these rocks originated

from the lower stratigraphic section of the Lower Cycladic Nappe (LCN) or that the sediment input varied at the time of deposition. Nonetheless, the zircon age spectra is significantly different then the hanging wall exposed on Thera (see below).

A small subset of U-Pb zircon analyses from both structural levels yielded an intriguing age of ca. 30 Ma, which broadly correlates with the oldest $^{40}Ar/^{39}Ar$ mica age recorded in the footwall. These Eocene-Oligocene zircon may represent statistical outliers with no geological relevance or could be interpreted as being metamorphic or hydrothermally-altered grains, reflecting the transition from blueschist to greenschist facies conditions, as has been shown on Serifos and Syros (Tomaschek et al., 2003; Schneider et al., 2011; Seman et al., 2017). The grains themselves do not significantly differ from other grains in their morphology or Th/U values, and any interpretation is highly speculative, yet captivating.

The dacite at Athinios was dated at 8.52 ± 0.17 Ma (Figure 9), and is likely an extension of the granitic body that was previously reported at depth in drill core from Megalochori, south of Athinios (Figure 2, Skarpelis et al., 1992). The authors of that study dated the drill core granitoid that yielded a K-Ar biotite age of 9.2 ± 0.2 Ma. The reported age is slightly older than the U-Pb date, possibly because the K-Ar system is more susceptible to thermal resetting and excess daughter isotope (McDougall and Harrison, 1999). Consequently, the K-Ar date may not be as reliable as the U-Pb age of zircon. New geochemical results are also consistent with those reported in Skarpelis et al. (1992) and, as plotted on the discrimination diagram of Winchester and Floyd (1977), the rock is determined to be compositionally dacitic (Figure 6). This classification is also supported by petrographic analysis that shows porphyritic quartz and plagioclase in a fine-grained matrix, a common texture of extrusive or hypabyssal rocks (Figure 4). The dacite is likely a surface expression of the granitoid sampled in drill core, which would explain the similar chemistry and

slight variation in texture. Although it is possible the dacite may be a separate intrusive body than one in the drill core, the proximity, chemistry and age point towards the two being at a minimum cogenetic but likely of the same magmatic body. Nonetheless, the ages are broadly similar and suggest Santorini possess some of the youngest extension-related magmatism in the Cyclades (along with Lavrion, Berger et al., 2013).

The longstanding interpretation is that the footwall rocks exposed at Athinios and Emporio belong to the PQU (Kilias et al., 1998; Craddock et al., 2009; Marsellos et al., 2012). However, based on the new geochronology and the observation that the rocks at Athinios experienced high-pressure/low-temperature conditions overprinted by greenschist facies metamorphism (Skarpelis and Liati, 1990), I suggest that these rocks belong to the CBU. Strikingly similar lithotypes are exposed on many other Cycladic islands, and the peak metamorphic conditions on Santorini of 350-380°C at 11-12 kbar (Davis and Bastas, 1978; Skarpelis and Liati, 1990) fall in the range of the broader CBU, notably the LCN (Grasemann et al., 2017). Furthermore, the intrusion of the granite at c. 8.5 Ma and its associated Ca-Fe-Mg skarn and Pb-Zn-Ba mineralization shares many parallels with Miocene intrusions of the CBU below the West Cycladic Detachment System (Marinos, 1951; Murad and Hubberten, 1975; Bonsall et al., 2011; Berger et al., 2013; Ducoux et al., 2017). Based on these observations, together with the Miocene deformation ages discussed below, I suggest that the footwall rocks below the Santorini detachment belong to the CBU.

Deformation and cooling

The footwall rocks are characterized by being highly sheared with foliation defined by aligned muscovite ribbons and stretched quartz, and is the result of E-W folding along which top-to-SE shearing is observed. Shearing is observed in most lithotypes, however those lithologies that

are more mineralogically homogeneous such as the quartzites and marbles have deformed primarily through mylonitization. The widespread SE-directed shear evinces a greenschist facies metamorphic overprint on Thera, clearly demonstrated by the dominant Ms-Chl-Ab±Bt mineral assemblage defining the shear fabric of the footwall rocks (Figure 4). This greenschist metamorphism is overprinting an early blueschist facies metamorphism which occurred during subduction of these sedimentary rocks (Skarpelis and Liati, 1990). When dated via $^{40}Ar/^{39}Ar$ methods, muscovite records consistently late Oligocene-Miocene ages (Figure 10) that can potentially be interpreted as either cooling ages, crystallization ages or deformation ages. Davis and Bastas (1978) present evidence that the basement rocks at Athinios have witnessed metamorphic conditions of up to 380°C and 11-12 kbar that was associated with regional subduction during the Eocene (Jolivet and Brun, 2010; Ring et al., 2010; Grasemann et al., 2017). Muscovite may undergo partial resetting at temperatures of 250°C (McDougall and Harrison, 1999), although a relatively higher closure temperature of 400°C has also been suggested (Harrison et al., 2009). That these grains do not record Eocene ages despite the rocks having undergone sufficient metamorphic conditions to prompt resetting indicate that the muscovite must have been affected by later processes. This would also preclude the interpretation that these grains record the timing of primary crystallization. Rather, these ages must record a later deformation event. The occurrence of Tschermak substitution (Figure 12) indicates that these grains have undergone chemical substitution and re-equilibration from high-pressure phengite phases (Parra et al., 2002; Cossette et al., 2015). This process has resulted in relatively homogenous muscovite grains (Figure 11) indicating that these grains have been completely recrystallized as they as no longer chemical consistent with phengite. Miocene defomration and low-temperature metamorphism is the likely mechanism behind this recrystallization as the footwall $^{40}Ar/^{39}Ar$ ages reported in this study

correspond to the Oligocene-Miocene muscovite dates obtained throughout the Cyclades which has been attributed to Miocene extension and deformation (Thomson et al., 2010; Grasemann et al., 2012; Bröcker et al., 2013; Cossette et al., 2015).

A population of older $^{40}Ar/^{39}Ar$ muscovite analyses at ca. 225 Ma from sample ALS05 was also obtained from the footwall rocks of Athinios. These grains may represent a detrital component as the dates are similar to those obtained from zircon U-Pb analysis from the meta-rhyolite. Alternatively, these older dates and may represent a partially reset component in which case these ages have little geological significance.

The timing of Miocene magmatism in the footwall of 8.5 Ma coincides with the new zircon (U-Th)/He ages from the same area, which preserved cooling dates ranging from ca. 11-7 Ma in Athinios and ca. 11 Ma at Emporio (Figure 13). Since the zircon (U-Th)/He system can be affected by 120-200°C temperatures (Reiners, 2005; Wolfe and Stockli, 2010), the thermal aureole from the Miocene intrusion may have reset or partially reset the (U-Th)/He ages, but given the unknown size of the dacitic body at depth it is unlikely that the thermal aureole could have affected the entirety of the footwall. Most Cycladic islands document apatite (20-8 Ma) and zircon (22-10 Ma) fission-track ages for footwall rocks, for which closure temperatures are ~120°C and 240-280°C, respectively (Brichau et al., 2006, 2007, 2008, 2010; Ring et al., 2003, 2010; Thompson et al., 2009). The footwall of the West Cycladic Detachment system exposed along four islands (Figure 1) preserves Miocene (U-Th)/He dates, as well (Grasemann et al., 2012). Many of these published cooling ages are interpreted to document low-temperature cooling and deformation, and this is likely also the case of Thera where deformation and metamorphism occurred during Miocene extension as recorded by $^{40}Ar/^{39}Ar$ ages, which is consistent with the detachment itself shown to have developed under ductile-brittle processes (Figure 3).

Hanging wall rocks of Profitis Ilias

Composed dominantly of calcitic marble, the rocks of Profitis Ilias also contain a sequence of clastic sedimentary rocks interpreted to be a Paleogene flysch sequence (Figure 3, Tataris, 1964). These clastic rocks differ slightly in chemistry than those of the footwall (Table 1) but show similar REE patterns (Figure 5). Large *Megalodon* fossils within the marbles indicate that the carbonate sequence is Triassic in age (Papastamatiou, 1958). This fossil bearing marble may represent a passive margin carbonate platform sequence that is stratigraphically overlain by Paleocene and Eocene flysch sediments (Faupl et al., 1999).

Sampled for U-Pb dating of detrital zircon (Figure 8), the sediments within the flysch contain a much younger detrital zircon signature than those of the footwall, with 24% of analyses yielding Triassic ages and an additional 44% of Carboniferous to Cambrian ages. With a maximum depositional age of ca. 112 Ma, the detrital signature of the flysch sediments are similar to those reported by Seman et al. (2017, Figure 8). Although these hanging wall sediments certainly do not belong to the CBU they may involve a component of sediment recycling derived from within the Hellinides (cf. Seman et al., 2017) Additionally, Triassic magmatism has been shown to be widespread throughout the Cyclades (Bröcker and Pidgeon, 2007; Schneider et al., 2011; Liati et al., 2013; Bröcker et al., 2015), which may have contributed to the flysch sediments and may account for the relatively large percentage of Triassic ages.

$^{40}Ar/^{39}Ar$ muscovite analyses from the flysch yield ages of 60-50 Ma with a small subset of older ages. As was the case with the $^{40}Ar/^{39}Ar$ ages from the footwall, these ages may record crystallization or cooling, or be detrital in nature. The hanging wall muscovite present in the flysch differ from those observed in footwall rocks as the mica does not define the strong planar structure

of the rocks. By contrast, the somewhat larger white mica grains were observed to be indiscriminately oriented (Figure 4) within a weak to moderate foliation. Chemically these grains fall within the muscovite field (Figure 12) with relatively homogeneous chemistry although containing corroded rims when observed in thin section (Figures 4, 11). The older $^{40}Ar/^{39}Ar$ dates establish that these rocks did not experience elevated temperatures during the Miocene, as was the case in the footwall; instead the dates could be recording a retrograde P-T path following the end of Eocene subduction (Jolivet and Bun, 2010; Grasemann et al., 2012, 2017). The fact that these grains also plot along the Tschermak substitution trend indicates that these grains may have been altered along the retrograde P-T path from higher pressure variants of white mica (i.e., phengite). The calcitic marble that envelops the flysch sediments however, has not been affected by high-pressure metamorphism and is only seen to be weakly deformed (Figure 3, 4; Schneider et al., 2018). As such, if these grains are recording a retrograde P-T path, this metamorphism was not experience by the rocks of the hanging wall, indicating these white mica grains must have originated elsewhere. Given the morphology of the muscovite and clastic nature of the rock, the $^{40}Ar/^{39}Ar$ dates are interpreted as detrital with the ages of these grains constraining a Paleocene to Eocene age of the flysch sediments as first suggested by Tataris (1964).

The rocks of the hanging wall have been exposed to minimal deformation in comparison with those of the footwall. As was seen both at the outcrop and thin section scale, the rocks of the hanging wall exhibit low-temperature brittle deformation (Figures 3, 4). Strain in the rocks of the hanging wall is based on proximity to the detachment with those more proximal localities displaying stronger deformation, as demonstrated by sample ALS12 from the quarry near the fault that records Miocene $^{40}Ar/^{39}Ar$ ages (Figure 10). Although this sample was affected by Miocene metamorphism, temperatures across the hanging wall were insufficient to affect the

geochronometers. Zircon (U-Th)/He analyses yield primarily early Miocene ages (22-15 Ma) which correspond to the regional greenschist facies metamorphism, similar to the white mica $^{40}Ar/^{39}Ar$ ages in the footwall. This would indicate that during this period, the hanging wall was cooling through ~200°C temperatures. An older population of (U-Th)/He ages (ca. 31 Ma) from sample ALS17 (Figure 11) demonstrates that not all zircon were reset, and that cooling was likely rapid. The combined thermochronology data highlights the differences in the temperature regime of the hanging wall, and predominance of brittle deformation, compared to the ductile-brittle evolution of the footwall.

Conclusions

The presence of a newly discovered low-angle top-to-SE detachment system on the island of Thera has forced a re-evaluation of the tectonic setting of the Cyclades. Whereas the geodynamic significance and the kinematics of the Naxos-Paros (Urai et al., 1990; Buick, 1991), the North- (Jolivet et al., 2010) and the West-Cycladic Detachment systems (Grasemann et al., 2012) are generally accepted (Figure 1), the importance of S-directed shear sense in the southern Cyclades, particularly on Ios, is contentious (Lister et al., 1984; Forster and Lister, 2009; Huet et al., 2009; Thomson et al., 2009; Ring et al., 2011; Mizera and Behrmann, 2016). Most of the detachment systems in the Cyclades, including new observations from Thera, are localized in ultramylonitic rock structurally below cataclasites and juxtapose tectonic units with markedly different thermal histories. A major reason for the debate in the southern Cyclades is that the S-directed kinematics either record distributed extensional deformation that cuts into deeper tectonic units, or were active under Eocene high-pressure conditions and are unrelated to Miocene extension.

New detrital zircon age spectra presented here for pre-volcanic rocks, in conjunction with a meta-rhyolite date, constrain the age of the footwall as Middle Triassic to Carboniferous, an age consistent with the Cycladic Blueschist Unit. The CBU is juxtaposed against Pelagonian marbles capped by an Eocene flysch, and confirms the long-postulated detachment with an S-directed shear sense at the southern margin of the Cycladic plateau (Vandenberg and Lister, 1996; Ring et al., 2011). Ios, which also records S-directed kinematics, lacks the presence of a detachment or a hanging wall, and is composed entirely of the CBU. I therefore propose that Ios belong to a deeper portion of the footwall of the Santorini detachment (Figure 1).

The Santorini detachment system furthermore strengthens arguments for the bivergent nature of Miocene extension in the Cyclades (Thomson et al., 2009; Grasemann et al., 2012) as new geochronology indicates it was coeval with the Naxos-Paros, North-, and West-Cycladic Detachment systems and ends with late kinematic intrusion of granitoids (e.g., Iglseder et al., 2009; Denèle et al., 2011). The dacite at Athinios, along with granites from Lavrion and Serifos (Figure 1) mark some of the youngest intrusions in the Hellenides and is the southernmost exposure of extension-related Miocene magmatism (Jolivet et al., 2015). Oligocene-Miocene $^{40}Ar/^{39}Ar$ muscovite ages document greenschist facies deformation related to this extension, which is further resolved with the lower-temperature (U-Th)/He zircon geochronology. These results firmly establish Thera within the Cycladic realm, document Miocene deformation, and change the geologic map of the Hellenides.

References

Altherr, R., Schliestedt, M., Okrusch, M., Seidel, E., Kreuzer, H., Harre, W., Lenz, H., Wendt, I., and Wagner, G.A., 1979. Geochronology of high-pressure rocks on Sifnos (Cyclades, Greece). Contributions to Mineralogy and Petrology, v. 70, p. 245-255.

Anders, B., Reischmann, T., and Kostopoulos, D., 2007. Zircon geochronology of basement rocks from the Pelagonian Zone, Greece: constraints on the pre-Alpine evolution of the westernmost Internal Hellenides. International Journal of Earth Sciences/Geologische Rundschau, v. 96, p. 639-661.

Berger, A., Schneider, D., Grasemann, B., and Stockli, D., 2013. Footwall mineralization during Late Miocene extension along the West Cycladic Detachment System, Lavrion, Greece. Terra Nova, v. 25, p. 181-191.

Best, M.G., Christiansen, E.H., Deino, A.L., Grommé, C.S., and Tingey, D.G., 1995. Correlation and emplacement of a large, zoned, discontinuously exposed ash flow sheet; the $^{40}Ar/^{39}Ar$ chronology, paleomagnetism, and petrology of the Pahranagat Formation, Nevada. Journal of Geophysical Research, v. 100, p. 24593-24609.

Black, L.P., Kamo, S.L., Allen, C.M., Aleinikoff, J.N., Davis, D.W., Korsch, R.J. and Foudoulis, C., 2003. TEMORA 1: a new zircon standard for Phanerozoic U-Pb geochronology. Chemical Geology, v. 200, p. 155-170.

Bolhar, R., Ring, U., and Allen, C.M., 2010. An integrated zircon geochronological and geochemical investigation into the Miocene plutonic evolution of the Cyclades, Aegean Sea, Greece: Part 1—Geochronology. Contributions to Mineralogy and Petrology, v. 160, p. 719-742.

Bonneau, M., 1984. Correlation of the Hellenide nappes in the south-east Aegean and their tectonic reconstruction, in Dixon, J.E., and Robertson, A.H.F., eds., The Geological Evolution of the Eastern Mediterranean: Geological Society [London], Special Publications, p. 517-527.

Bonsall, T., Spry, P., Voudouris, P., Tombros, S., Seymour, K., and Melfos, V., 2011. The geochemistry of carbonate-replacement Pb-Zn-Ag mineralization in the Lavrion District, Attica, Greece: Fluid inclusion, stable isotope, and rare earth element studies. Economic Geology, v. 106, p. 619-651.

Brichau, S., Ring, U., Ketcham, R., Carter, A., Stockli, D., and Brunel, M., 2006. Constraining the long-term evolution of the slip rate for a major extensional fault system in the central Aegean, Greece, using thermochronology. Earth and Planetary Science Letters, v. 241, p. 293-306.

Brichau, S., Ring, U., Carter, A., Monié, P., Bolhar, R., Stockli, D., and Brunel., M., 2007. Extensional faulting on Tinos Island, Aegean Sea, Greece: How many detachments? Tectonics, v. 26, doi:10.1029/2006TC001969.

Brichau, S., Ring, U., Carter, A., Bolhar, R., Monié, P., Stockli, D., and Brunel, M., 2008. Timing, slip rate, displacement and cooling history of the Mykonos detachment footwall, Cyclades, Greece, and implications for the opening of the Aegean Sea basin. Journal of the Geological Society, London, v. 165, p. 263-277.

Brichau, S., Thomson, S., Ring, U., 2010. Thermochronometric constraints on the tectonic evolution of the Serifos detachment, Aegean Sea, Greece. International Journal of Earth Sciences, v. 99, p. 379-393.

Bröcker, M. and Keasling, A., 2006. Ion probe U–Pb zircon ages from the high-pressure/low temperature mélange of Syros, Greece: age diversity and the importance of pre-Eocene subduction. Journal of Metamorphic Geology, v. 24, p. 625-631.

Bröcker, M., and Pidgeon, R.T., 2007. Protolith ages of meta-igneous and metatuffaceous rocks from the Cycladic Blueschist Unit, Greece: results of a reconnaissance U-Pb zircon study. The Journal of Geology, v. 115, p. 83-98.

Bröcker, M., Baldwin, S., and Arkudas, R., 2013. The geological significance of $^{40}Ar/^{39}Ar$ and Rb-Sr white mica ages from Syros and Sifnos, Greece: A record of continuous (re)crystallization during exhumation? Journal of Metamorphic Geology, v. 31, p. 629-646.

Brun, J.-P., Faccenna, C., Gueydan, F., Sokoutis, D., Philippon, M., Kydonakis, K., and Gorini, C., 2016. The two stage Aegean extension, from localized to distributed, a result of slab rollback acceleration. Canadian Journal of Earth Sciences, v. 53, p. 1142-1157.

Buick, I., 1991. Mylonitic fabric development on Naxos. Journal of Structural Geology, v. 13, p. 643-655.

Cossette, É., Schneider, D.A., Warren, C.J., and Grasemann, B., 2015. Lithological, rheological, and fluid infiltration control on $^{40}Ar/^{39}Ar$ ages in polydeformed rocks from the West Cycladic detachment system, Greece. Lithosphere, v. 7, p. 189-205.

Craddock, J., Klein, T., Kowalczyk, G., and Zulauf, G., 2009. Calcite twinning strains in Alpine orogen flysch: Implications for thrust-nappe mechanics and the geodynamics of Crete. Lithosphere, v. 1, p. 174-191.

Davis, E., and Bastas, C., 1978. Petrology and geochemistry of the metamorphic system of Santorini, in Doumas, C., eds., Proceedings of the Second International Congress "Thera and the Aegean World,": The Thera Foundation [London], p. 61-79.

Dazé, A., Lee, J.K.W., and Villeneuve, M., 2003. An intercalibration study of the Fish Canyon sanidine and biotite $^{40}Ar/^{39}Ar$ standards and some comments on the age of the Fish Canyon Tuff. Chemical Geology, v. 199, p. 111-127.

Denèle, Y., Lecomte, E., Jolivet, L., Lacombe, O., Labrousse, L., Huet, B., and Le Pourhiet, L., 2011. Granite intrusion in a metamorphic core complex: The example of the Mykonos laccolith (Cyclades, Greece). Tectonophysics, v. 501, p. 52-70.

Dickinson, W.R., and Gehrels, G.E., 2009. Use of U–Pb ages of detrital zircons to infer maximum depositional ages of strata: A test against a Colorado plateau Mesozoic database. Earth Planetary Science Letters, v. 288, p. 115-125.,

Druitt, T., Edwards, L., Mellors, R., Pyle, D., Sparks, R. Lanphere, M., Davies, M., and Barriero, B., 1999. Santorini Volcano. Geological Society Publishing House [London], 165 pp.

Ducoux, M., Branquet, Y., Jolivet, L., Arbaret, L., Grasemann, B., Rabillard, A., Gumiaux, C., and Drufin, S., 2017. Synkinematic skarns and fluid drainage along detachments: The West Cycladic Detachment System on Serifos Island (Cyclades, Greece) and its related mineralization. Tectonophysics, v. 695, p. 1-26.

Dürr, S., Altherr, R., Keller, J., Okrusch, M., and Seuidel, E., 1978. The Median Aegean Crystalline Belt: stratigraphy, structure, metamorphism, magmatism, in Cloos, H., Roeder, D., and Schmidt, K., eds., Alps, Apennines, Hellenides. Schweizerbart, Stuttgart, p. 455-477.

Faupl, P., Pavlopoulos, A., and Migiros, G., 1999. The Paleogene history of the Pelagonian Zone s.l. (Hellenides, Greece): Heavy mineral study from terrigenous flysch sediments. Geologica Carpathica, v. 50, p. 449-458.

Forster, M.A., and Lister, G.S., 2005. Several distinct tectono-metamorphic slices in the Cycladic eclogite-blueschist belt, Greece. Contributions to Mineralogy and Petrology, v. 150, p. 523-545.

Forster, M., and Lister, G., 2009. Core-complex-related extension of the Aegean lithosphere initiated at the Eocene-Oligocene transition. Journal of Geophysical Research, v. 114, doi:10.1029/2007JB005382.

Gehrels, G., 2012. Detrital zircon U-Pb geochronology: current methods and new opportunities, in Busby, C., and Azor, A., eds., Tectonics of Sedimentary Basins: Recent Advances. Blackwell publishing, p. 47-62.

Grasemann, B., Schneider, D., Stockli, D., and Iglseder, C., 2012. Miocene bivergent crustal extension in the Aegean: Evidence from the western Cyclades (Greece). Lithosphere, v. 4, p. 23-39.

Grasemann, B., Huet, B., Schneider, D., Rice, A.H.N., Lemmonnier, N., and Tschegg, C., 2017. Miocene post-orogenic extension of the Eocene synorogenic imbricated Hellenic subduction channel: New constraints from Milos (Cyclades, Greece). Geological Society of America Bulletin, v. 130, p. 238-262.

Harrison, T. M., and Zeitler, P.K., 2005. Fundamentals of noble gas thermochronometry. Reviews in Mineralogy & Geochemistry, v. 58, p. 123-149

Harrison, T.M., Célérier, J., Aikman, A.B., Hermann, J., Heizler, M.T., 2009. Diffusion of ^{40}Ar in muscovite. Geochimica et Cosmochimica Acta, v. 73, p. 1039-1051.

Huet, B., Labrousse, L., and Jolivet, L., 2009. Thrust or detachment? Exhumation processes in the Aegean: Insight from a field study on Ios (Cyclades, Greece). Tectonics, v. 28, doi:10.1029/2008TC002397.

Iglseder, C., Grasemann, B., Schneider, D.A., Petrakakis, K., Miller, C., Klötzli, U., Thöni, M., Zámolyi, A., Rambousek, C., 2009. Tertiary I- and S-type plutonism on Serifos, Western Cyclades, Greece. Tectonophysics, v. 473, p. 69-83.

Jacobshagen, V., 1986. Geologie von Griechenland. Gebrueder Borntraeger [Berlin], 636 pp.

Jolivet, L., Goffé, B., Monié, P., Truffert-Luxey, C., Patriat, M., and Bonneau, M., 1996. Miocene detachment in Crete and exhumation P-T-t paths of high-pressure metamorphic rocks. Tectonics, v. 15, p. 1129-1153.

Jolivet, L., and Brun, J.-P., 2010. Cenozoic geodynamic evolution of the Aegean. International Journal of Earth Sciences, v. 99, p. 109-138.

Jolivet, L., Lecomte, E., Huet, B., Denèle, Y., Lacombe, O., Labrousse, L., Le Pourhiet, L., and Mehl, C., 2010. The North Cycladic Detachment System. Earth and Planetary Science Letters, v. 289, p. 87-104.

Jourdan, F., Verati, C., and Féraud, G., 2006. Intercalibration of the Hb3gr $^{40}Ar/^{39}Ar$ dating standard. Chemical Geology, v. 231, p. 77-189.

Keay, S., and Lister, G., 2002. African provenance for the metasediments and metaigneous rocks of the Cyclades, Aegean Sea, Greece. Geology, v. 30, p. 235-238.

Kilias A., Mountrakis D., Tranos M., and Pavlides S., 1998. The prevolcanic metamorphic rocks of Santorini island: Structural evolution and kinematics during the Tertiary (South Aegean, Greece), in Casale, R., Fytikas, M., Sigvaldasson, G., and Vougioukalakis, G., eds., Volcanic risk. The European laboratory volcanoes, 2nd Workshop, p. 23-36.

Kuiper, K.F., Deino, A., Hilgen, F.J., Krijgsman, W., Renne, R., and Wijbrans, J.R., 2008. Synchronizing Rock Clocks of Earth History. Science, v. 320, p. 500-504.

Liati, A., Skarpelis, N., and Fanning, M.C., 2013. Late Permian–Early Triassic igneous activity in the Attic Cycladic Belt (Attica): New geochronological data and geodynamic implications. Tectonophysics, v. 595-596, p. 140-147.

Lips, A.L.W., Wijbrans, J.R,, and White, S.H., 1999. New insights from $^{40}Ar/^{39}Ar$ laser probe dating of white mica fabrics from the Pelion Massif, Pelagonian Zone, Internal Hellenides, Greece: implications for the timing of metamorphic episodes and tectonic events in the Aegean region. Geological Society of London Special Publication, v. 156, p. 457-474.

Lister, G.S., Banga, G., Feenstra, A., 1984. Metamorphic core complexes of cordilleran type in the Cyclades, Aegean Sea, Greece. Geology, v. 12, p. 221-225.

Ludwig, K.R., 2012. Isoplot 3.75: A Geochronological Toolkit for Microsoft Excel. Berkeley Geochronological Centre Special Publication no 5.

Marinos, G., 1951. Geology and metallogenesis of Seriphos island. The mineral wealth of Greece, volume I [Athens], Institute for Geology and Subsurface Research, p. 95-127.

Marsellos, A.E., Kidd, W.S.F., Garver, J.I., and Kyriakopoulos, K.G., 2012. Exhumation of HP-rocks accompanied by low-angle normal faulting and associated detachment fault of Milos Island—Evidence from zircon fission track thermochronology. Geochemistry, Mineralogy, and Petrology, v. 49, p. 49-46.

Marsellos, A.E., Foster, D., Kamenov, G. and Kyriakopoulos, K.G., 2012. Detrital zircon U-Pb data from the Hellenic south Aegean belts: Constraints on the age and source of the South Aegean basement, in Skourtsos, E., and Lister, G.S., eds., The Geology of Greece, Journal of the Virtual Explorer, Electronic Edition, v. 42, doi:10.3809/jvirtex.2011.00284.

Maruyama, S., Liou, J. G., and Terabayashi, M., 1996. Blueschists and eclogites of the world and their exhumation. International geology review, v. 38, p. 485-594.

McDougall, I., and Harrison, T.M., 1999. Geochronology and thermochronology by the 40ar/39ar method. 2nd ed, United States, Oxford University Press, 269 p.

McFarlane, C.R.M., and Luo, Y., 2012. U-Pb geochronology using 193 nm Excimer LA-ICP-MS optimized for in situ accessory mineral dating in thin sections. Geoscience Canada, v. 39, p. 158-172.

Mizera, M., and Behrmann, J., 2016. Strain and flow in the metamorphic core complex of Ios Island (Cyclades, Greece). International Journal of Earth Sciences, v. 105, p. 2097-2110.

Mountrakis, D., Eleftheriadis, G., Christofides, G., Kilias, A., and Sapountzis, E., 1987. Silicic metavolcanics in the Western Pelagonian Margin of Greece related to the opening of Neo-Tethys. Chemie der Erde, v. 47, p. 167-179.

Murad, E., and Hubberten, H.-W., 1975. Sulfide mineralization in phyllites from the Island of Thera, Santorini Archipelago, Greece. Neues Jahrbuch für Mineralogie Monatshefte, v. H7, p. 300-308.

Okrusch, M., and Bröcker, M., 1990. Eclogites associated with high-grade blueschists in the Cyclades archipelago, Greece: a review. European Journal of Mineralogy, v. 2, p. 451-478.

Papastamatiou, J., 1958. Sur l'âge des calcaire cristillins de I'île de Thera (Santorin). Bulletin of the Geological Society of Greece, v. 3, p. 104-113.

Parra, T., Vidal, O., and Agard, P., 2002. A thermodynamic model for Fe-Mg dioctahedral K white micas using data from phase-equilibrium experiments and natural pelitic assemblages. Contributions to Mineralogy and Petrology, v. 143, p. 706-732.

Pasqualon, N.G., Santos, K.N.S., Marsellos, A.E., and Kyriakopoulos, K.G., 2016. Implications of petrography and geochemistry of Athinios metamorphic units using PXRF and GIS

analyses in Thera (Santorini, Greece). Bulletin of the Geological Society of Greece, v. 50, p. 1980-1988.

Paton, C., Hellstrom, J., Paul, B., Woodhead, J., and Hergt, J., 2011. Iolite: Freeware for the visualisation and processing of mass spectrometric data. Journal of Analytical Atomic Spectrometry, v. 26, p. 2508-2518.

Pe-Piper, G., Piper, D.J.W., 2002. The Igneous Rocks of Greece: The Anatomy of an Orogen. Berlin, Gebruder Borntraeger, 573 p.

Petrus, J.A., and Kamber, B.S., 2012. VizualAge: A novel approach to laser ablation ICP-MS UPb geochronology data reduction. Geostandards and Geoanalytical Research, v. 36, p. 247-270.

Photiades, A., and Keay, S., 2003. Geological and geochronological data for Sikinos and Folegandros metamorphic units (Cyclades, Greece): Their tectono-stratigraphic significance. Bulletin of the Geological Society of Greece, v.35, p. 35-45.

Reiners, P.W., Farley. K.A., and Hickes, H., 2002. He diffusion and (U–Th)/He thermochronometry of zircon: Initial results from Fish Canyon Tuff and Gold Butte. Tectonophysics, v. 349, p. 297-308.

Reiners, P.W., Spell, T.L., Nicolescu, S., and Zanetti K.A., 2004. Zircon (U-Th)/He thermochronometry: He diffusion and comparisons with $^{40}Ar/^{39}Ar$ dating. Geochimica et Cosmochimica Acta, v. 68, p. 1857-1887.

Reiners, P.W., 2005. Zircon (U-Th)/He thermochronometry. Reviews in Mineralogy and Geochemistry, v. 58, p. 151-179.

Renne P.R., Swisher C.C., Deino A.L., Karner D.B., Owens T.L., and DePaolo D.J., 1998. Intercalibration of standards, absolute ages and uncertainties in $^{40}Ar/^{39}Ar$ dating. Chemical

Geology, v. 145, p. 117-152.

Renne, P.R., and Norman, E.B., 2001. Determination of the half-life of ^{40}Ar by mass spectrometry. Physics Review C, v. 63, doi: 10.1103/PhysRevC.63.047302.

Ring, U., Layer, P.W., and Reischmann, T., 2001. Miocene high-pressure metamorphism in the Cyclades and Crete, Aegean Sea, Greece: evidence for large-magnitude displacement on the Cretan detachment. Geology, v. 29, p. 395-398.

Ring, U., and Layer, P.W., 2003. High-pressure metamorphism in the Aegean, eastern Mediterranean: underplating and exhumation from the Late Cretaceous until the Miocene to recent above the retreating Hellenic subduction zone. Tectonics, v. 22, doi:10.1029/2001TC001350.

Ring, U., Will T., Glodny, J., Kumerics, C., Gessner, K., Thomson, S., Güngör, T., Monié, P., Okrusch, M., and Drüppel, K. 2007. Early exhumation of high-pressure rocks in extrusion wedges: Cycladic blueschist unit in the eastern Aegean, Greece, and Turkey. Tectonics v. 26, doi:10.1029/2005TC001872.

Ring, U., Thomson, S.N., and Rosenbaum, G., 2009. Timing of the Amorgos detachment system and implications for detachment faulting in the southern Aegean Sea, Greece. Geological Society, London Special Publication, v. 321, p. 169-177.

Ring, U., Glodny, J., Will, T., and Thomson, S., 2010. The Hellenic subduction system: High-pressure metamorphism, exhumation, normal faulting, and large-scale extension. Annual Review of Earth and Planetary Sciences, v. 38, p. 45-76.

Ring, U., Glodny, J., Will, T., and Thomson, S., 2011. Normal faulting on Sifnos and the South Cycladic Detachment System, Aegean Sea, Greece. Journal of the Geological Society, v. 168, p. 751-768.

Robertson, A.H.F., Clift, P.D., Degnan, P.J., and Jones, G., 1991. Paleogeographic and paleotectonic evolution of the eastern Mediterranean Neotethys. Palaeogeography, Palaeoclimatology, Palaeoecology, v. 87, p. 289-343.

Roddick, J.C., 1983. High precision intercalibration of ^{40}Ar-^{39}Ar standards. Geochimica Cosmochimica et Acta, v. 47, p. 887-898.

Seman, S., Stockli, D.F., and Soukis, K., 2017. The provenance and internal structure of the Cycladic Blueschist Unit revealed by detrital zircon geochronology, Western Cyclades, Greece, Tectonics, v. 36, p. 1407-1429.

Schneider, D.A., Senkowski, C., Vogel, H., Grasemann, B., and Iglseder, C., 2011. Eocene tectonometamorphism on Serifos (Western Cyclades) deduced from zircon depth profiling geochronology and mica thermochronology. Lithos, v. 125, p. 151-172.

Schneider, D.A., Grasemann, B., Lion, A., Soukis, K., and Draganits, E., 2018. Geodynamic significance of the Santorini Detachment System (Cyclades, Greece). Terra Nova, v. 30, p. 414-422.

Shaked, Y., Avigad, D., and Garfunkel, Z., 2000. Alpine high-pressure metamorphism at the Almyropotamos window (southern Evia, Greece). Geological Magazine, v. 137, p. 367-380.

Sherlock, S., Kelley, S.P., Inger, S., Harris, N., and Okay, A.I., 1999. $^{40}Ar/^{39}Ar$ and Rb-Sr geochronology of high-pressure metamorphism and exhumation history of the Tavsanli Zone, NW Turkey. Contributions to Mineralogy and Petrology, v. 137, p. 46-58.

Skarpelis, N., and Liati, A., 1990. The prevolcanic basement of Thera at Athinios: Metamorphism, plutonism and mineralization, in Hardy, D., eds., Proceedings of the Third International Congress "Thera and the Aegean World," The Thera Foundation [London], p.

172-182.

Skarpelis, N., Kyriakopoulos, K., and Villa, I., 1992. Occurrence and $^{40}Ar/^{39}Ar$ dating of a granite in Thera (Santorini, Greece). Geologische Rundschau, v. 81, p. 729-735.

Slama, J., Kosler, J., Condon, D.J., Crowley, J.L., Gerdes, A., Hanchar, J.M., Horstwood, M., Morris, G.A., Nasdala, L., Norberg, N., Schaltegger, U., Schoene, B., Tubrett, M.N., and Whitehouse, M.J., 2008. Plesovice zircon - a new natural reference material for U-Pb and Hf isotopic microanalysis. Chemical Geology, v. 249, p. 1-35.

Steiger R.H., and Jäger E., 1977. Subcommission on geochronology: convention on the use of decay constants in geo- and cosmochronology. Earth Planetary Science Letters, v. 36, p. 359-362.

Spell T.L., and McDougall, I., 2003. Characterization and calibration of $^{40}Ar/^{39}Ar$ dating standards. Chemical Geology, v. 198, p. 189-211.

Sun, S.S., and McDonough, W.F., 1989. Chemical and isotopic systematics of oceanic basalts: implications for mantle composition and processes. Geological Society of London Special Publication, v. 42, p. 313–345.

Tataris, A., 1964. The Eocene in the semi-metamorphosed basement of Thera island. Bulletin of the Geological Society of Greece, v. 6, p. 232-238.

Thomson, S., Stöckhert, B., and Brix, M.R., 1998. Thermochronology of the high-pressure metamorphic rocks of Crete, Greece: implications for the speed of tectonic processes. Geology, v. 26, p. 259-262.

Thomson, S.N., Stöckhert, B., and Brix, M.R., 1999. Miocene high-pressure metamorphic rocks of Crete, Greece: rapid exhumation by buoyant escape. Geological Society of London Special Publication, v. 154, p. 87-108.

Thomson, S., Ring, U., Brichau, S., Glodny, J., and Will, T., 2009. Timing and nature of formation of the Ios metamorphic core complex, southern Cyclades, Greece, in Ring, U., and Wernicke, B., eds., Extending a continent: Architecture, rheology and heat budget. Geological Society [London], Special Publications, p. 139-167.

Tomaschek, F., A. Kennedy, I. Villa, M. Lagos, and C. Ballhaus, 2003. Zircons from Syros, Cyclades, Greece—Recrystallization and mobilization of zircon during high-pressure metamorphism. Journal of Petrology, v. 44, p. 1977-2002.

Urai, J., Schuiling, R., and Jansen, J., 1990. Alpine deformation on Naxos (Greece), in Knipe, R.J., and Rutter, E.H., eds., Deformation mechanisms, rheology and tectonics. Geological Society [London], Special Publications, p. 509-522.

Vandenberg, L. and Lister, G., 1996. Structural analysis of basement tectonites from the Aegean metamorphic core complex of Ios, Cyclades, Greece. Journal of Structural Geology, v. 18, p. 1437-1454.

Wiedenbeck, M., Allen, P., Corfu, F., Griffin, W.L., Meier, M., Oberli, F., Von Quadt, A., Roddick, J.C., and Spiegel, W., 1995. Three natural zircon standards for U-Th-Pb, Lu-Hf, trace element and REE analyses. Geostandards and Geoanalystical Research, v. 19, p. 1-23.

Winchester, J.A., and Floyd, P.A., 1977. Geochemical discrimination of different magma series and their differentiation products using immobile elements. Chemical Geology, v. 20, p. 325-343.

Wolfe, M. R., and Stockli, D.F., 2010. Zircon (U–Th)/He thermochronometry in the KTB drill hole, Germany, and its implications for bulk He diffusion kinetics in zircon. Earth and Planetary Science Letters. 295, v. p. 69-82.

Zulauf, G., Dörr, W., Fisher-Spurlock, S.C., Gerdes, A., Chatzaras, V., and Xypolias, P., 2015. Closure of the Paleotethys in the External Hellenides: Constraints from U–Pb ages of magmatic and detrital zircons (Crete). Gondwana Research, v. 28, p. 642-667.

Appendix A. Major (wt%) and trace (ppm) element data for rocks from Thera (Santorini), Greece

Sample	ALS02	ALS03	ASL05	ALS08	ALS11	ALS13	ALS17
	quartzite	dacite	conglomerate	quartzite	meta-rhyolite	conglomerate	schist
SiO_2	83.35	68.56	73.28	91.81	52.27	52.56	65.30
Al_2O_3	3.69	14.59	3.45	3.58	5.15	7.01	12.88
Fe_2O_3	1.63	1.98	2.10	1.39	2.11	2.96	5.56
MgO	0.32	1.32	0.72	0.59	0.56	2.00	4.15
CaO	4.71	2.53	9.93	0.18	20.15	17.07	1.80
Na_2O	0.04	1.80	0.42	0.14	1.32	0.95	1.71
K_2O	0.93	5.18	0.61	0.86	0.70	1.20	2.42
TiO_2	0.31	0.29	0.29	0.24	0.32	0.29	0.63
P_2O_5	0.03	0.08	0.05	0.05	0.09	0.07	0.11
MnO	0.07	0.05	0.05	0.02	0.05	0.14	0.07
Cr_2O_3	0.00	0.01	0.00	0.00	0.01	0.03	0.04
LOI	4.80	3.40	9.00	1.10	17.20	15.60	5.10
Sum	99.96	99.89	99.95	99.98	99.92	99.91	99.86
Ba	218	946	241	143	156	257	318
Ni	BDL	BDL	BDL	BDL	BDL	73	144
Sc	4	6	4	3	4	7	13
Be	BDL	3	BDL	BDL	BDL	BDL	3
Co	3.8	3.8	6.0	5.7	5.8	10.1	14.5
Cs	2.2	2.0	1.7	1.4	1.0	2.1	3.1
Ga	6.6	15.4	4.3	4.6	5.2	6.1	13.2
Hf	4.0	3.8	3.5	2.3	2.1	2.0	3.7
Nb	5.9	12.5	4.9	5.2	7.9	4.5	12.6
Rb	47.2	193.4	23.5	28.3	24.3	42.8	93.3
Sn	33	15	3	3	2	2	77
Sr	49.6	236.3	137.5	6.5	341.1	226.5	50.7
Ta	0.5	1.5	0.3	0.3	0.5	0.3	0.9
Th	3	22.2	2.6	2.5	6.8	3.4	7.8
U	0.9	7.6	0.9	0.5	1.2	0.8	2.1
V	36	30	44	28	39	52	106
W	1.4	2.5	1.1	0.6	1.1	BDL	1.4
Zr	161.4	131.0	140.9	93.9	84.8	80.7	142.3
Y	8.2	16.5	11.1	8.1	13.2	11.8	17.2
La	8.0	30.5	9.4	8.2	17.0	13.0	27.6
Ce	15.0	55.5	17.1	13.0	30.5	25.0	53.1
Pr	1.86	5.64	2.11	1.73	3.67	2.93	5.86
Nd	7.4	19.2	8.6	6.8	13.9	11.8	21.3
Sm	1.45	3.70	2.00	1.29	2.90	2.35	3.97
Eu	0.28	0.59	0.49	0.29	0.94	0.63	0.83
Gd	1.31	2.99	2.12	1.46	2.88	2.35	3.46
Tb	0.23	0.49	0.32	0.23	0.44	0.35	0.54
Dy	1.36	2.78	1.99	1.36	2.42	2.04	3.14

Appendix A. Major (wt%) and trace (ppm) element data for rocks from Thera (Santorini), Greece

Sample	ALS02	ALS03	ASL05	ALS08	ALS11	ALS13	ALS17
	quartzite	dacite	conglomerate	quartzite	meta-rhyolite	conglomerate	schist
Ho	0.32	0.57	0.38	0.29	0.47	0.41	0.67
Er	0.97	1.75	1.11	0.84	1.24	1.14	2.08
Tm	0.15	0.27	0.16	0.11	0.18	0.17	0.30
Yb	0.99	1.70	1.10	0.73	1.03	1.09	1.91
Lu	0.16	0.28	0.17	0.11	0.16	0.17	0.30
TOT/C	1.00	0.38	2.14	0.02	4.54	3.75	0.52
TOT/S	BDL	0.04	BDL	BDL	BDL	BDL	BDL
Mo	BDL	0.4	BDL	BDL	BDL	0.2	0.2
Cu	5.3	16.6	7.5	14.9	8.0	15.0	20.3
Pb	5.3	78.5	2.5	0.4	6.2	6.2	8.2
Zn	69	30	25	20	18	30	58
Ni	7.5	9.0	10.2	10.2	9.8	73.4	132.5
As	12.4	1.1	5.4	0.9	3.1	5.6	3.9
Cd	BDL	0.2	BDL	BDL	BDL	BDL	BDL
Sb	0.2	BDL	0.2	BDL	BDL	BDL	0.2
Bi	0.2	0.1	BDL	BDL	0.1	0.1	0.1
Ag	0.1	0.3	BDL	BDL	BDL	BDL	BDL
Au	BDL	0.5	1.2	BDL	16.6	2.3	1.3
Hg	BDL	BDL	BDL	BDL	BDL	0.0	0.1
Tl	BDL	0.1	BDL	BDL	BDL	BDL	BDL
Se	BDL	BDL	BDL	BDL	BDL	BDL	BDL

BDL = Below detection limits

TOT/C/S = Total carbon and sulphur (%)

Appendix B. Results of single grain zircon U-Pb ICP-MS analysis from Thera (Santorini), Greece

Grain no.	Measured ratios									Apparent ages (Ma)					
	$^{207}Pb/^{206}Pb$	1σ	$^{206}Pb/^{238}U$	1σ	$^{207}Pb/^{235}U$	1σ	$^{208}Pb/^{232}Th$	1σ	Discordance (%)	$^{207}Pb/^{206}Pb$	1σ	$^{206}Pb/^{238}U$	1σ	$^{207}Pb/^{235}U$	1σ
ALS02, quartzite, 359540 N, 4027830 E															
1	0.0700	0.0014	0.1454	0.0018	1.4029	0.0282	0.0460	0.0007	1.7	927.9	40.0	875.0	10.1	890.1	11.9
2a	0.1822	0.0027	0.4334	0.0052	10.8892	0.1703	0.1359	0.0020	8.3	2673.2	24.6	2321.0	23.6	2513.7	14.6
02b	0.1813	0.0026	0.5319	0.0063	13.2982	0.2027	0.1415	0.0020	1.8	2665.1	23.9	2749.3	26.6	2701.1	14.4
3	0.1635	0.0027	0.4496	0.0055	10.1360	0.1698	0.1312	0.0019	2.2	2492.2	27.1	2393.5	24.4	2447.3	15.5
5	0.0618	0.0020	0.1006	0.0014	0.8566	0.0277	0.0338	0.0006	1.7	666.1	68.4	617.8	8.1	628.3	15.2
6	0.0670	0.0019	0.0985	0.0013	0.9097	0.0251	0.0337	0.0006	8.5	837.5	56.7	605.5	7.6	656.9	13.4
7	0.0740	0.0012	0.1664	0.0020	1.6970	0.0283	0.0528	0.0007	1.5	1040.5	32.2	992.2	11.0	1007.4	10.7
8	0.0724	0.0012	0.1581	0.0019	1.5776	0.0262	0.0467	0.0007	1.6	997.0	32.3	946.0	10.5	961.4	10.3
9	0.1685	0.0025	0.4682	0.0056	10.8782	0.1700	0.1404	0.0019	1.5	2543.1	24.8	2475.4	24.7	2512.8	14.5
10	0.0666	0.0011	0.1389	0.0017	1.2750	0.0217	0.0444	0.0006	0.5	824.5	33.9	838.4	9.4	834.6	9.7
11	0.0601	0.0010	0.1031	0.0012	0.8541	0.0151	0.0315	0.0009	0.9	607.1	36.9	632.3	7.2	626.9	8.3
12	0.0614	0.0011	0.1010	0.0012	0.8549	0.0154	0.0304	0.0007	1.2	653.8	37.2	620.0	7.1	627.3	8.4
13	0.0631	0.0015	0.1175	0.0015	1.0218	0.0238	0.0393	0.0006	0.2	710.6	48.7	716.1	8.5	714.8	12.0
14	0.0603	0.0017	0.0862	0.0011	0.7165	0.0204	0.0275	0.0004	3.0	614.8	60.5	532.7	6.7	548.6	12.0
15	0.0621	0.0012	0.1027	0.0012	0.8791	0.0166	0.0316	0.0005	1.6	676.3	39.1	630.4	7.3	640.5	9.0
16	0.0586	0.0020	0.1157	0.0016	0.9356	0.0318	0.0376	0.0010	5.0	553.7	73.2	705.8	9.2	670.5	16.7
18	0.0703	0.0012	0.1528	0.0018	1.4819	0.0260	0.0486	0.0007	0.7	938.1	34.7	916.6	10.2	923.0	10.7
20	0.0687	0.0012	0.1432	0.0017	1.3556	0.0241	0.0459	0.0007	0.9	888.9	35.3	862.6	9.7	870.0	10.4
21	0.0714	0.0012	0.1657	0.0020	1.6317	0.0279	0.0518	0.0007	0.6	970.1	33.5	988.1	10.9	982.5	10.8
22	0.0683	0.0018	0.1319	0.0017	1.2420	0.0324	0.0446	0.0009	2.7	877.7	53.3	798.6	9.8	819.8	14.7
23	0.0665	0.0012	0.1286	0.0016	1.1779	0.0220	0.0410	0.0006	1.4	820.9	37.8	779.6	8.9	790.3	10.3
24	0.0587	0.0012	0.0915	0.0011	0.7412	0.0156	0.0295	0.0004	0.3	557.1	44.6	564.6	6.6	563.1	9.1
25	0.0649	0.0037	0.0964	0.0016	0.8626	0.0479	0.0308	0.0008	6.4	769.9	114.6	593.5	9.6	631.6	26.1
26	0.1836	0.0029	0.4875	0.0059	12.3398	0.1991	0.1402	0.0020	2.8	2685.4	25.6	2560.0	25.4	2630.6	15.2
27	0.0719	0.0014	0.1658	0.0020	1.6434	0.0333	0.0519	0.0009	0.2	982.7	40.3	988.9	11.3	987.0	12.8
29	0.0644	0.0019	0.1061	0.0014	0.9418	0.0275	0.0317	0.0008	3.6	753.1	60.9	650.3	8.3	673.8	14.4
30	0.0778	0.0017	0.1730	0.0022	1.8555	0.0414	0.0542	0.0009	3.6	1141.0	43.4	1028.4	12.2	1065.4	14.7
31	0.0625	0.0012	0.1195	0.0015	1.0302	0.0200	0.0385	0.0007	1.2	692.1	40.1	727.7	8.3	719.0	10.0
32	0.0736	0.0014	0.1738	0.0021	1.7632	0.0346	0.0533	0.0009	0.1	1030.4	38.6	1032.7	11.7	1032.0	12.7
33	0.0660	0.0022	0.1449	0.0020	1.3192	0.0425	0.0425	0.0010	2.1	806.8	66.7	872.5	11.3	854.1	18.6
34	0.0728	0.0012	0.1577	0.0019	1.5835	0.0262	0.0522	0.0009	2.1	1008.5	31.8	944.0	10.6	963.7	10.3
35	0.0717	0.0011	0.1572	0.0019	1.5533	0.0250	0.0510	0.0007	1.1	976.5	31.3	941.0	10.4	951.8	9.9
36	0.0727	0.0015	0.1702	0.0021	1.7069	0.0344	0.0510	0.0008	0.2	1006.6	39.9	1013.2	11.5	1011.1	12.9
37	0.1253	0.0022	0.2636	0.0032	4.5552	0.0807	0.0929	0.0015	15.4	2033.5	30.4	1508.1	16.5	1741.1	14.8
38	0.0626	0.0013	0.1173	0.0015	1.0125	0.0216	0.0390	0.0008	0.7	693.7	44.1	715.0	8.4	710.2	10.9
41	0.0593	0.0013	0.1050	0.0013	0.8587	0.0192	0.0332	0.0005	2.3	577.2	47.2	643.9	7.6	629.4	10.5
42	0.0735	0.0010	0.1112	0.0013	1.1272	0.0158	0.0363	0.0005	12.8	1027.9	25.8	679.7	7.6	766.4	7.6
43	0.1144	0.0014	0.2861	0.0034	4.5122	0.0611	0.0944	0.0013	6.9	1869.8	22.3	1621.8	16.9	1733.2	11.3
44	0.0685	0.0015	0.1404	0.0018	1.3264	0.0298	0.0478	0.0014	1.3	884.1	45.3	846.7	10.1	857.3	13.0
45	0.0702	0.0012	0.1489	0.0018	1.4426	0.0247	0.0360	0.0005	1.3	935.3	33.5	894.9	10.1	906.8	10.3
46	0.0718	0.0011	0.1643	0.0020	1.6270	0.0266	0.0512	0.0007	0.0	979.9	31.4	980.8	10.9	980.7	10.3
47	0.0749	0.0018	0.1737	0.0023	1.7935	0.0430	0.0564	0.0010	1.1	1064.8	47.3	1032.2	12.4	1043.1	15.6
48	0.0988	0.0014	0.2906	0.0035	3.9610	0.0577	0.0866	0.0012	1.1	1602.2	25.2	1644.5	17.3	1626.2	11.8
50	0.1667	0.0021	0.4379	0.0052	10.0664	0.1372	0.1294	0.0016	4.3	2524.5	21.0	2341.3	23.2	2440.9	12.6
51	0.0521	0.0010	0.0500	0.0006	0.3595	0.0071	0.0166	0.0002	0.9	289.6	43.6	314.8	3.7	311.9	5.3
54	0.0612	0.0020	0.1059	0.0015	0.8936	0.0293	0.0357	0.0008	0.1	645.9	69.3	648.7	8.5	648.3	15.7
56	0.1517	0.0020	0.3656	0.0043	7.6488	0.1067	0.1112	0.0014	9.1	2364.8	22.0	2008.6	20.5	2190.6	12.5
58	0.0665	0.0012	0.0791	0.0010	0.7252	0.0134	0.0358	0.0005	12.8	820.7	37.0	490.9	5.8	553.8	7.9
59	0.0933	0.0019	0.1035	0.0013	1.3307	0.0269	0.0465	0.0007	35.4	1492.9	37.3	634.7	7.6	859.2	11.7
61	0.0749	0.0016	0.1453	0.0019	1.5001	0.0328	0.0486	0.0007	6.4	1064.9	42.9	874.4	10.4	930.4	13.3
62	0.0590	0.0020	0.0909	0.0013	0.7395	0.0253	0.0285	0.0004	0.2	566.4	73.3	560.8	7.5	562.1	14.8
63	0.1505	0.0023	0.3569	0.0044	7.4092	0.1179	0.1238	0.0017	9.9	2351.9	25.8	1967.4	20.9	2162.1	14.2
64	0.1106	0.0018	0.3339	0.0041	5.0943	0.0859	0.1012	0.0013	1.2	1809.6	29.1	1857.3	19.9	1835.2	14.3
65	0.0680	0.0012	0.1407	0.0017	1.3200	0.0239	0.0449	0.0006	0.7	868.9	35.9	848.7	9.7	854.5	10.5
66	0.0659	0.0020	0.1363	0.0019	1.2396	0.0373	0.0448	0.0009	0.6	804.2	62.1	823.9	10.5	818.7	16.9
67	0.0807	0.0011	0.1018	0.0012	1.1335	0.0171	0.0405	0.0005	23.1	1214.4	27.5	625.1	7.1	769.4	8.1
68	0.1705	0.0025	0.5008	0.0062	11.7791	0.1794	0.1520	0.0019	1.2	2562.9	23.9	2617.2	26.4	2587.0	14.3
71	0.0696	0.0010	0.1555	0.0019	1.4914	0.0232	0.0485	0.0007	0.5	915.6	30.0	931.5	10.3	926.9	9.5
72	0.0616	0.0011	0.1144	0.0014	0.9715	0.0179	0.0362	0.0005	1.3	658.6	37.8	698.5	8.1	689.3	9.2
73	0.0597	0.0011	0.1037	0.0013	0.8534	0.0167	0.0338	0.0004	1.5	592.9	40.3	635.9	7.4	626.5	9.2
74	0.1727	0.0023	0.4584	0.0055	10.9154	0.1531	0.1290	0.0016	3.4	2583.5	21.6	2432.5	24.1	2516.0	13.1
75	0.0757	0.0015	0.1962	0.0024	2.0465	0.0401	0.0574	0.0010	2.0	1086.0	37.9	1154.6	13.1	1131.1	13.4
76	0.0738	0.0011	0.1254	0.0015	1.2756	0.0195	0.0434	0.0006	9.7	1035.5	28.8	761.4	8.6	834.9	8.7
80	0.0565	0.0017	0.1044	0.0014	0.8129	0.0241	0.0329	0.0005	5.6	470.2	64.7	640.0	8.1	604.1	13.5
81	0.0608	0.0013	0.0962	0.0012	0.8065	0.0174	0.0309	0.0004	1.4	631.2	45.0	592.3	7.0	600.5	9.8
82	0.0666	0.0012	0.1309	0.0016	1.2018	0.0218	0.0414	0.0006	1.0	824.2	36.2	793.1	9.1	801.4	10.1
85	0.0559	0.0015	0.0975	0.0013	0.7518	0.0202	0.0309	0.0006	5.1	447.8	58.3	599.9	7.4	569.2	11.7
86	0.0661	0.0011	0.1336	0.0016	1.2173	0.0208	0.0413	0.0006	0.0	808.7	34.0	808.3	9.2	808.5	9.5
88	0.0513	0.0029	0.0046	0.0001	0.0325	0.0018	0.0015	0.0000	10.2	256.0	123.7	29.5	0.5	32.5	1.8
89	0.0647	0.0021	0.1202	0.0017	1.0722	0.0352	0.0401	0.0012	1.1	763.7	68.2	731.9	9.6	739.8	17.2
90	0.0578	0.0058	0.1123	0.0025	0.8958	0.0890	-0.0062	0.0521	5.3	523.2	206.9	686.2	14.3	649.5	47.7
91	0.1669	0.0023	0.4226	0.0051	9.7260	0.1402	0.1264	0.0017	6.0	2526.9	22.5	2272.1	22.9	2409.2	13.3
93	0.0621	0.0011	0.1066	0.0013	0.9129	0.0162	0.0326	0.0005	0.8	676.8	36.2	653.2	7.5	658.6	8.6
94	0.0579	0.0010	0.0902	0.0011	0.7197	0.0126	0.0281	0.0004	1.1	525.1	36.8	556.5	6.4	550.5	7.4
95	0.0525	0.0020	0.0045	0.0001	0.0326	0.0012	0.0016	0.0000	12.4	305.1	83.7	29.0	0.4	32.6	1.2
96	0.1305	0.0017	0.2590	0.0031	4.6590	0.0660	0.0896	0.0011	18.5	2104.1	22.9	1484.7	15.7	1759.9	11.8
97	0.0607	0.0009	0.1029	0.0012	0.8611	0.0132	0.0236	0.0004	0.1	629.0	30.6	631.2	7.2	630.7	7.2
98	0.0650	0.0032	0.1043	0.0017	0.9354	0.0451	0.0327	0.0006	4.8	775.8	99.6	639.5	9.8	670.5	23.6
99	0.2723	0.0034	0.5002	0.0059	18.7819	0.2550	0.1286	0.0016	15.9	3319.3	19.4	2614.6	25.4	3030.7	13.1
100	0.3201	0.0040	0.6631	0.0079	29.2644	0.3974	0.1791	0.0022	5.6	3570.1	19.0	3279.2	30.5	3462.4	13.3
102	0.0633	0.0017	0.1112	0.0015	0.9706	0.0262	0.0361	0.0007	1.3	718.0	56.3	679.7	8.5	688.8	13.5
103	0.0612	0.0013	0.1001	0.0012	0.8442	0.0178	0.0335	0.0005	1.1	645.8	43.9	614.7	7.3	621.4	9.8
104	0.0666	0.0013	0.1426	0.0018	1.3091	0.0252	0.0474	0.0007	1.1	824.2	38.6	859.5	9.9	849.7	11.1
108	0.0688	0.0014	0.1641	0.0020	1.5571	0.0312	0.0513	0.0007	2.6	893.8	40.0	979.2	11.3	953.3	12.4
109	0.0619	0.0012	0.1061	0.0013	0.9063	0.0176	0.0369	0.0007	0.8	672.2	40.1	650.1	7.6	655.1	9.4
110	0.1672	0.0024	0.4644	0.0057	10.7055	0.1643	0.1394	0.0018	1.6	2529.9	24.1	2458.8	25.0	2497.9	14.3
111	0.1355	0.0019	0.2535	0.0030	4.7346	0.0702	0.1006	0.0014	21.8	2170.0	24.1	1456.4	15.6	1773.4	12.4
112	0.0621	0.0010	0.0903	0.0011	0.7726	0.0129	0.0312	0.0004	4.3	675.8	33.6	557.3	6.4	581.2	7.4
114	0.0609	0.0011	0.0641	0.0008	0.5387	0.0102	0.0226	0.0003	9.2	637.2	39.3	400.6	4.7	437.6	6.8

Appendix B. Results of single grain zircon U-Pb ICP-MS analysis from Thera (Santorini), Greece

Grain no.	Measured ratios									Apparent ages (Ma)					
	$^{207}Pb/^{206}Pb$	1σ	$^{206}Pb/^{238}U$	1σ	$^{207}Pb/^{235}U$	1σ	$^{208}Pb/^{232}Th$	1σ	Discordance (%)	$^{207}Pb/^{206}Pb$	1σ	$^{206}Pb/^{238}U$	1σ	$^{207}Pb/^{235}U$	1σ
116	0.0771	0.0012	0.1802	0.0022	1.9147	0.0313	0.0572	0.0008	1.7	1123.0	30.7	1067.9	11.8	1086.2	10.9
117	0.0848	0.0013	0.1643	0.0020	1.9195	0.0300	0.0550	0.0007	11.0	1309.8	28.5	980.4	10.9	1087.9	10.4
118	0.0732	0.0015	0.1779	0.0022	1.7954	0.0371	0.0543	0.0009	1.1	1019.6	40.5	1055.3	12.2	1043.8	13.5
119	0.0650	0.0014	0.1298	0.0016	1.1642	0.0254	0.0402	0.0005	0.4	775.3	44.6	787.0	9.3	783.9	11.9
125	0.0751	0.0011	0.1786	0.0021	1.8491	0.0285	0.0560	0.0009	0.4	1071.0	29.0	1059.3	11.7	1063.1	10.2
127	0.0790	0.0012	0.0963	0.0012	1.0497	0.0168	0.0348	0.0004	22.9	1172.7	29.8	592.9	6.8	728.7	8.3
128	0.0695	0.0012	0.1311	0.0016	1.2567	0.0226	0.0422	0.0006	4.1	914.2	35.4	794.1	9.1	826.4	10.2
129	0.0575	0.0016	0.0975	0.0013	0.7733	0.0214	0.0313	0.0007	3.0	511.2	60.1	599.7	7.5	581.6	12.3
130	0.0590	0.0010	0.1041	0.0013	0.8468	0.0143	0.0320	0.0005	2.4	567.1	34.6	638.4	7.3	622.9	7.8
ALS03a, dacite, 359381 N, 4027820 E															
6	0.0644	0.0022	0.0014	0.0000	0.0123	0.0004	0.0005	0.0000	39.3	755.9	71.7	8.9	0.1	12.4	0.4
7	0.0994	0.0028	0.0015	0.0000	0.0198	0.0006	0.0011	0.0000	114.0	1612.9	52.1	9.3	0.1	19.9	0.6
8	0.0555	0.0017	0.0014	0.0000	0.0105	0.0003	0.0005	0.0000	20.5	431.0	66.1	8.8	0.1	10.6	0.3
14	0.0483	0.0031	0.0013	0.0000	0.0087	0.0005	0.0005	0.0000	4.8	114.3	142.4	8.4	0.1	8.8	0.6
16	0.0447	0.0024	0.0013	0.0000	0.0077	0.0004	0.0006	0.0000	2.5	0.1	50.1	8.0	0.1	7.8	0.4
19	0.0621	0.0012	0.0497	0.0006	0.4258	0.0087	0.0226	0.0005	15.2	677.8	41.7	312.7	3.9	360.2	6.2
20	0.0527	0.0020	0.0013	0.0000	0.0097	0.0004	0.0005	0.0000	14.0	316.4	85.1	8.6	0.1	9.8	0.4
27	0.0424	0.0070	0.0013	0.0000	0.0078	0.0013	0.0005	0.0001	8.1	0.1	169.1	8.6	0.2	7.9	1.3
30	0.0818	0.0018	0.0013	0.0000	0.0149	0.0003	0.0006	0.0000	76.5	1240.9	41.2	8.5	0.1	15.0	0.3
34	0.0452	0.0021	0.0013	0.0000	0.0081	0.0004	0.0005	0.0000	2.4	0.1	67.4	8.4	0.1	8.2	0.4
36	0.0484	0.0027	0.0013	0.0000	0.0083	0.0005	0.0005	0.0000	5.0	117.6	126.9	8.0	0.1	8.4	0.5
39	0.0522	0.0026	0.0013	0.0000	0.0093	0.0005	0.0005	0.0000	13.3	293.4	110.0	8.3	0.1	9.4	0.5
41	0.0518	0.0030	0.0013	0.0000	0.0091	0.0005	0.0005	0.0000	12.2	275.6	128.3	8.2	0.1	9.2	0.5
46	0.0812	0.0023	0.0014	0.0000	0.0153	0.0004	0.0005	0.0000	76.1	1227.3	53.7	8.8	0.1	15.5	0.4
47	0.0460	0.0022	0.0013	0.0000	0.0082	0.0004	0.0004	0.0000	0.0	0.1	108.7	8.3	0.1	8.3	0.4
48	0.0508	0.0053	0.0016	0.0000	0.0111	0.0011	0.0007	0.0000	9.8	231.1	225.1	10.2	0.2	11.2	1.2
49	0.0497	0.0022	0.0013	0.0000	0.0091	0.0004	0.0005	0.0000	8.2	180.9	99.3	8.5	0.1	9.2	0.4
58	0.0507	0.0034	0.0013	0.0000	0.0092	0.0006	0.0005	0.0000	9.4	224.8	149.4	8.5	0.2	9.3	0.6
59	0.0478	0.0019	0.0013	0.0000	0.0089	0.0004	0.0005	0.0000	3.5	90.1	91.5	8.6	0.1	8.9	0.4
60	0.0512	0.0025	0.0013	0.0000	0.0094	0.0005	0.0005	0.0000	10.5	250.9	109.0	8.6	0.1	9.5	0.5
65	0.0514	0.0025	0.0014	0.0000	0.0096	0.0005	0.0005	0.0000	10.2	260.1	106.7	8.8	0.1	9.7	0.5
66	0.0709	0.0065	0.0014	0.0000	0.0139	0.0012	0.0004	0.0000	53.8	954.1	176.0	9.1	0.2	14.0	1.2
67	0.0429	0.0053	0.0014	0.0000	0.0083	0.0010	0.0005	0.0000	6.7	0.1	107.7	9.0	0.2	8.4	1.0
70	0.0543	0.0026	0.0013	0.0000	0.0099	0.0005	0.0006	0.0000	17.6	384.8	104.6	8.5	0.1	10.0	0.5
72	0.0735	0.0024	0.0013	0.0000	0.0132	0.0004	0.0005	0.0000	58.3	1027.8	65.5	8.4	0.1	13.3	0.4
73	0.0579	0.0032	0.0014	0.0000	0.0110	0.0006	0.0005	0.0000	24.7	523.8	118.0	8.9	0.2	11.1	0.6
ALS05, schist conglomerate, 358981 N, 4027944 E															
2	0.0641	0.0011	0.1120	0.0014	0.9893	0.0176	0.0394	0.0005	2.1	743.7	35.3	684.3	8.1	698.4	9.0
4a	0.0684	0.0013	0.1026	0.0013	0.9673	0.0185	0.0454	0.0007	9.2	880.3	37.5	629.5	7.6	687.1	9.6
4b	0.0617	0.0012	0.0990	0.0013	0.8418	0.0173	0.0355	0.0006	1.9	663.0	42.0	608.4	7.3	620.2	9.5
5	0.0667	0.0012	0.1514	0.0019	1.3934	0.0260	0.0524	0.0008	2.5	829.7	36.8	908.8	10.6	886.1	11.0
6	0.0952	0.0014	0.1011	0.0012	1.3260	0.0209	0.0513	0.0007	38.1	1531.0	27.3	620.6	7.2	857.1	9.1
7	0.0580	0.0012	0.0859	0.0011	0.6863	0.0148	0.0395	0.0030	0.1	527.8	45.7	531.1	6.4	530.6	8.9
8	0.0721	0.0011	0.1603	0.0020	1.5930	0.0255	0.0570	0.0008	0.9	987.5	29.9	958.7	11.0	967.5	10.0
9	0.0622	0.0017	0.0571	0.0008	0.4892	0.0132	0.0268	0.0005	13.0	679.4	56.2	357.8	4.6	404.4	9.0
10	0.1595	0.0023	0.4625	0.0057	10.1740	0.1572	0.1392	0.0019	0.0	2450.7	24.1	2450.5	24.9	2450.7	14.3
11	0.0623	0.0010	0.1043	0.0013	0.8962	0.0149	0.0362	0.0005	1.6	685.5	32.9	639.4	7.5	649.7	8.0
12	0.0700	0.0020	0.1093	0.0015	1.0555	0.0296	0.3339	0.0047	9.4	928.8	56.4	668.9	8.6	731.6	14.6
13	0.1689	0.0025	0.4514	0.0056	10.5125	0.1643	0.1486	0.0021	3.3	2546.9	24.2	2401.2	24.6	2481.0	14.5
14	0.1826	0.0026	0.5166	0.0064	13.0091	0.2032	0.1569	0.0022	0.2	2676.7	23.7	2684.9	27.3	2680.3	14.7
15	0.0576	0.0010	0.0893	0.0011	0.7089	0.0131	0.0316	0.0005	1.3	512.7	38.7	551.5	6.6	544.1	7.8
16	0.0770	0.0017	0.1690	0.0022	1.7944	0.0412	0.0621	0.0010	3.6	1121.0	44.5	1006.8	12.2	1043.4	15.0
17	0.0682	0.0010	0.1443	0.0018	1.3577	0.0220	0.0500	0.0007	0.2	875.9	30.9	868.8	10.0	870.9	9.5
18	0.1626	0.0026	0.4760	0.0060	10.6709	0.1794	0.1481	0.0027	0.6	2482.9	26.6	2509.6	26.1	2494.9	15.6
19	0.1752	0.0025	0.4278	0.0052	10.3335	0.1581	0.1317	0.0018	7.4	2607.8	23.4	2295.8	23.6	2465.1	14.2
21	0.0624	0.0022	0.0768	0.0011	0.6605	0.0235	0.0107	0.0011	7.9	687.1	74.7	477.0	6.6	514.9	14.4
23	0.0722	0.0027	0.1766	0.0026	1.7577	0.0648	0.0626	0.0013	1.8	990.7	73.9	1048.5	14.5	1030.0	23.9
25	0.0598	0.0010	0.0929	0.0011	0.7658	0.0133	0.0331	0.0005	0.8	596.2	35.4	572.6	6.8	577.4	7.7
26	0.0613	0.0012	0.1037	0.0013	0.8760	0.0171	0.0366	0.0006	0.5	649.4	39.9	635.8	7.6	638.8	9.3
27	0.0684	0.0025	0.1053	0.0015	0.9932	0.0360	0.0375	0.0011	8.6	882.0	73.7	645.1	9.0	700.4	18.3
30	0.1128	0.0017	0.3059	0.0038	4.7590	0.0759	0.1051	0.0015	3.3	1845.2	26.7	1720.7	18.5	1777.7	13.4
31	0.0998	0.0017	0.2837	0.0035	3.9027	0.0679	0.0998	0.0015	0.3	1619.7	30.5	1610.1	17.8	1614.2	14.1
32	0.0658	0.0016	0.1312	0.0017	1.1905	0.0286	0.0446	0.0009	0.2	800.8	48.9	794.5	9.8	796.2	13.3
33	0.0663	0.0023	0.1489	0.0022	1.3603	0.0471	0.0535	0.0013	2.5	814.6	71.1	894.7	12.1	872.0	20.2
34	0.1588	0.0026	0.4307	0.0054	9.4291	0.1596	0.1446	0.0022	3.1	2442.5	27.0	2309.0	24.2	2380.7	15.5
36	0.1098	0.0020	0.1141	0.0015	1.7268	0.0325	0.0616	0.0010	46.3	1795.6	32.8	696.4	8.4	1018.5	12.1
37	0.0663	0.0013	0.1402	0.0018	1.2805	0.0249	0.0455	0.0007	1.0	814.4	38.9	845.7	9.9	837.1	11.1
38	0.0755	0.0020	0.1799	0.0025	1.8721	0.0495	0.0599	0.0010	0.4	1080.8	51.9	1066.6	13.4	1071.3	17.5
39	0.0629	0.0014	0.1060	0.0014	0.9193	0.0205	0.0362	0.0009	1.9	703.9	45.9	649.7	7.9	662.0	10.8
40	0.1147	0.0019	0.2414	0.0030	3.8158	0.0648	0.0793	0.0012	14.5	1874.7	28.7	1393.7	15.6	1596.1	13.7
41	0.1675	0.0032	0.1168	0.0015	2.6975	0.0524	0.0723	0.0011	86.5	2533.0	31.7	712.0	8.8	1327.8	14.4
42	0.0666	0.0012	0.1241	0.0016	1.1389	0.0214	0.0418	0.0007	2.4	824.2	37.2	754.1	8.9	772.0	10.1
43	0.0718	0.0013	0.1692	0.0021	1.6756	0.0324	0.0638	0.0011	0.8	980.9	37.5	1007.8	11.8	999.3	12.3
45	0.0674	0.0016	0.1210	0.0016	1.1250	0.0270	0.0440	0.0009	4.0	851.5	48.5	736.1	9.1	765.3	12.9
46	0.1644	0.0026	0.4567	0.0057	10.3517	0.1716	0.1419	0.0021	1.7	2501.1	26.1	2425.1	25.0	2466.7	15.4
48	0.0644	0.0013	0.0959	0.0012	0.8513	0.0171	0.0302	0.0006	5.9	753.8	40.7	590.5	7.1	625.3	9.4
49	0.0621	0.0019	0.1129	0.0016	0.9664	0.0295	0.0425	0.0008	0.4	677.2	64.1	689.5	9.1	686.6	15.3
50	0.1476	0.0023	0.3088	0.0038	6.2852	0.1039	0.0999	0.0016	16.2	2318.4	26.5	1735.0	18.8	2016.4	14.5
51	0.1776	0.0028	0.5179	0.0064	12.6848	0.2096	0.1592	0.0024	1.3	2631.0	25.6	2690.3	27.2	2656.5	15.6
52	0.0544	0.0035	0.0043	0.0001	0.0321	0.0020	0.0016	0.0001	16.7	385.6	137.6	27.5	0.5	32.1	2.0
53a	0.0629	0.0013	0.1149	0.0015	0.9964	0.0208	0.0415	0.0007	0.1	704.6	42.7	701.1	8.4	702.0	10.6
53b	0.0677	0.0015	0.1232	0.0016	1.1497	0.0255	0.0464	0.0009	3.8	858.6	44.7	749.0	9.1	777.1	12.1
54	0.0705	0.0019	0.1518	0.0021	1.4768	0.0398	0.0605	0.0011	1.1	944.2	54.2	911.3	11.5	920.9	16.3
55	0.1148	0.0019	0.3243	0.0041	5.1351	0.0903	0.1050	0.0016	1.7	1877.2	30.0	1810.7	19.7	1841.9	14.9
56a	0.0603	0.0013	0.1123	0.0014	0.9341	0.0210	0.0369	0.0006	2.4	615.3	47.0	686.1	8.4	669.8	11.0
56b	0.0638	0.0016	0.0592	0.0008	0.5206	0.0129	0.0174	0.0003	14.8	735.3	51.2	370.6	4.7	425.6	8.6
57	0.0652	0.0016	0.0674	0.0009	0.6052	0.0148	0.0242	0.0004	14.3	779.2	50.0	420.3	5.3	480.5	9.3
58	0.0847	0.0016	0.1931	0.0025	2.2561	0.0450	0.0659	0.0012	5.3	1309.0	37.3	1138.3	13.3	1198.7	14.0
59	0.0587	0.0012	0.0863	0.0011	0.6980	0.0149	0.0309	0.0006	0.8	555.0	45.1	533.5	6.5	537.6	8.9
60	0.0639	0.0015	0.1253	0.0016	1.1043	0.0255	0.0455	0.0008	0.7	738.5	47.4	761.1	9.3	755.4	12.3

Appendix B. Results of single grain zircon U-Pb ICP-MS analysis from Thera (Santorini), Greece

Grain no.	Measured ratios									Apparent ages (Ma)					
	$^{207}Pb/^{206}Pb$	1σ	$^{206}Pb/^{238}U$	1σ	$^{207}Pb/^{235}U$	1σ	$^{208}Pb/^{232}Th$	1σ	Discordance (%)	$^{207}Pb/^{206}Pb$	1σ	$^{206}Pb/^{238}U$	1σ	$^{207}Pb/^{235}U$	1σ
61	0.0595	0.0012	0.1057	0.0013	0.8664	0.0179	0.0367	0.0008	2.2	583.9	43.1	647.6	7.8	633.6	9.7
63	0.0633	0.0014	0.1194	0.0016	1.0424	0.0238	0.0393	0.0010	0.2	719.8	47.0	726.8	8.9	725.1	11.8
65	0.0739	0.0014	0.1765	0.0022	1.7977	0.0341	0.0568	0.0009	0.3	1038.4	36.6	1047.6	12.1	1044.6	12.4
66	0.1783	0.0030	0.4485	0.0056	11.0217	0.1930	0.1201	0.0019	5.7	2636.8	27.6	2388.4	24.7	2525.0	16.3
67	0.0607	0.0012	0.0964	0.0012	0.8064	0.0167	0.0374	0.0016	1.2	628.1	43.0	593.1	7.2	600.4	9.4
68	0.0648	0.0012	0.1322	0.0017	1.1813	0.0227	0.0450	0.0008	1.1	768.0	38.6	800.4	9.4	791.9	10.6
70	0.0625	0.0013	0.1018	0.0013	0.8768	0.0185	0.0330	0.0006	2.3	689.6	43.5	625.1	7.6	639.3	10.0
71	0.1299	0.0026	0.3909	0.0051	7.0004	0.1414	0.1310	0.0021	0.7	2096.3	34.2	2127.0	23.7	2111.5	18.0
72	0.1664	0.0031	0.4856	0.0063	11.1381	0.2146	0.1430	0.0025	0.7	2521.4	31.1	2551.5	27.4	2534.8	18.0
ALS08, schist, 360641 N, 4025605 E															
1	0.0699	0.0011	0.1482	0.0018	1.4285	0.0229	0.0428	0.0006	1.1	925.4	30.8	890.8	10.0	900.9	9.6
2	0.0721	0.0012	0.1654	0.0020	1.6442	0.0282	0.0502	0.0007	0.0	987.8	33.1	986.9	11.1	987.3	10.8
4	0.0733	0.0014	0.1800	0.0022	1.8184	0.0350	0.0582	0.0009	1.4	1021.1	37.1	1067.0	12.2	1052.1	12.6
5	0.0679	0.0012	0.1225	0.0015	1.1468	0.0213	0.0386	0.0006	4.1	864.9	36.7	745.1	8.6	775.7	10.1
6	0.0662	0.0011	0.1264	0.0015	1.1536	0.0203	0.0531	0.0008	1.5	811.7	34.8	767.5	8.8	778.9	9.6
7	0.0739	0.0012	0.1689	0.0020	1.7209	0.0284	0.0509	0.0007	1.0	1038.3	31.3	1006.2	11.2	1016.4	10.6
8	0.0591	0.0018	0.1063	0.0014	0.8665	0.0256	0.0317	0.0004	2.7	570.6	63.1	651.4	8.3	633.7	13.9
9	0.0825	0.0012	0.1970	0.0024	2.2412	0.0341	0.0629	0.0008	3.0	1258.0	27.5	1159.0	12.7	1194.0	10.7
10	0.0594	0.0013	0.0892	0.0011	0.7310	0.0168	0.0284	0.0004	0.3	583.2	48.4	550.7	6.6	557.1	9.8
11	0.0731	0.0011	0.1689	0.0020	1.7013	0.0268	0.0514	0.0007	5.1	1015.3	29.8	1006.1	11.1	1009.0	10.1
12	0.0693	0.0015	0.1250	0.0016	1.1948	0.0256	0.0424	0.0006	2.8	908.6	42.7	759.2	9.0	798.2	11.8
13	0.0591	0.0012	0.1068	0.0013	0.8699	0.0184	0.0322	0.0007	1.0	570.6	44.3	653.9	7.7	635.5	10.0
14	0.0695	0.0015	0.1575	0.0020	1.5082	0.0338	0.0490	0.0009	1.5	912.2	44.9	942.8	11.1	933.7	13.7
15	0.0601	0.0010	0.0917	0.0011	0.7594	0.0137	0.0574	0.0016	0.1	606.5	37.1	565.3	6.6	573.7	7.9
16	0.0710	0.0009	0.1608	0.0019	1.5738	0.0225	0.0537	0.0007	3.0	956.8	26.8	961.2	10.6	959.9	8.9
17	0.0640	0.0017	0.1069	0.0014	0.9429	0.0249	0.0356	0.0007	2.3	741.3	54.6	654.5	8.1	674.4	13.0
18	0.0598	0.0010	0.0862	0.0010	0.7109	0.0121	0.0305	0.0007	5.6	596.2	34.8	533.1	6.1	545.3	7.2
19	0.0658	0.0019	0.1050	0.0014	0.9530	0.0268	0.0334	0.0006	3.3	800.9	57.8	643.6	8.1	679.6	13.9
20	0.0632	0.0016	0.1014	0.0013	0.8842	0.0222	0.0324	0.0006	7.5	715.8	52.1	622.8	7.6	643.3	12.0
21	0.0672	0.0012	0.1040	0.0013	0.9638	0.0183	0.0334	0.0005	2.6	844.7	37.9	637.7	7.4	685.3	9.5
22	0.0646	0.0013	0.1395	0.0017	1.2432	0.0259	0.0423	0.0007	2.6	761.6	42.3	842.1	9.8	820.3	11.7
24	0.0653	0.0012	0.1434	0.0018	1.2902	0.0250	0.0496	0.0008	3.9	782.4	39.0	863.7	10.0	841.4	11.1
25	0.0642	0.0018	0.1042	0.0014	0.9232	0.0255	0.0320	0.0005	0.9	749.4	57.2	639.1	8.0	664.0	13.5
26	0.0591	0.0011	0.0965	0.0012	0.7853	0.0150	0.0313	0.0005	0.0	568.8	40.0	593.6	6.9	588.5	8.6
28	0.0695	0.0012	0.1522	0.0019	1.4575	0.0263	0.0461	0.0007	4.3	912.2	35.4	913.2	10.4	913.0	10.9
29	0.0686	0.0018	0.1729	0.0023	1.6349	0.0431	0.0500	0.0013	0.4	886.0	53.4	1028.1	12.5	983.7	16.6
30a	0.0969	0.0015	0.2775	0.0034	3.7062	0.0611	0.0837	0.0010	17.2	1564.6	29.3	1578.8	17.0	1572.7	13.2
30b	0.0810	0.0012	0.1237	0.0015	1.3824	0.0217	0.0619	0.0008	4.3	1222.4	29.0	751.9	8.5	881.5	9.3
31	0.0723	0.0014	0.1439	0.0018	1.4350	0.0281	0.0493	0.0007	0.5	995.3	38.4	866.6	10.0	903.7	11.7
32	0.0647	0.0009	0.1238	0.0015	1.1045	0.0170	0.0389	0.0005	4.4	765.5	30.3	752.1	8.4	755.5	8.2
33	0.0576	0.0009	0.0851	0.0010	0.6756	0.0106	0.0271	0.0003		513.6	32.4	526.4	6.0	524.1	6.4
34	0.0896	0.0018	0.2180	0.0028	2.6935	0.0549	0.0693	0.0011	0.6	1417.3	37.8	1271.2	14.6	1326.7	15.1
35	0.0747	0.0010	0.1751	0.0021	1.8026	0.0269	0.0561	0.0007	0.5	1058.9	28.1	1040.2	11.4	1046.4	9.7
37a	0.1634	0.0020	0.4671	0.0055	10.5248	0.1421	0.1396	0.0016	2.6	2491.4	20.7	2470.8	24.1	2482.1	12.5
37b	0.1664	0.0021	0.4529	0.0053	10.3919	0.1400	0.1327	0.0015	0.7	2521.9	20.6	2408.3	23.5	2470.3	12.5
38	0.0666	0.0012	0.1331	0.0016	1.2225	0.0234	0.0413	0.0006	5.2	825.9	38.2	805.4	9.3	810.9	10.7
39	0.0736	0.0016	0.1450	0.0018	1.4712	0.0324	0.0525	0.0008	1.5	1030.4	43.5	872.8	10.3	918.6	13.3
40	0.0612	0.0009	0.0983	0.0012	0.8293	0.0130	0.0311	0.0004	0.1	645.8	31.5	604.4	6.9	613.2	7.2
42	0.0698	0.0015	0.1543	0.0019	1.4849	0.0318	0.0504	0.0008	0.9	921.7	42.7	925.3	10.8	924.2	13.0
44	0.0618	0.0011	0.1136	0.0014	0.9682	0.0182	0.0347	0.0005	3.0	667.6	38.5	693.7	8.0	687.5	9.4
46	0.0650	0.0012	0.1123	0.0014	1.0055	0.0184	0.0361	0.0006	1.4	772.8	36.7	685.9	7.9	706.6	9.3
47	0.0741	0.0011	0.1678	0.0020	1.7153	0.0272	0.0518	0.0008	1.2	1045.1	30.0	1000.0	11.1	1014.3	10.2
48	0.0698	0.0010	0.1468	0.0017	1.4123	0.0221	0.0461	0.0006	4.9	921.6	30.4	883.1	9.8	894.1	9.3
49	0.0543	0.0020	0.0854	0.0012	0.6398	0.0235	0.0281	0.0005	3.1	384.9	80.2	528.3	7.0	502.2	14.5
50	0.0699	0.0014	0.1380	0.0017	1.3303	0.0268	0.0427	0.0006	6.3	925.9	40.1	833.4	9.7	859.0	11.7
51	0.0639	0.0013	0.0916	0.0011	0.8066	0.0168	0.0301	0.0006	2.1	736.9	42.7	565.0	6.7	600.6	9.4
52	0.0618	0.0013	0.0990	0.0012	0.8432	0.0179	0.0314	0.0005	1.4	667.0	44.0	608.3	7.2	620.9	9.8
53	0.0607	0.0010	0.1098	0.0013	0.9187	0.0158	0.0337	0.0004	0.8	628.8	35.3	671.3	7.6	661.7	8.4
54a	0.0649	0.0011	0.1226	0.0015	1.0965	0.0192	0.0412	0.0007	0.1	769.7	34.8	745.5	8.6	751.7	9.3
54b	0.0666	0.0018	0.1372	0.0018	1.2601	0.0335	0.0419	0.0008	0.7	826.2	54.3	828.6	10.2	828.0	15.0
55	0.0601	0.0011	0.0953	0.0012	0.7890	0.0144	0.0298	0.0004	1.3	605.7	37.9	586.7	6.8	590.6	8.2
56	0.0609	0.0011	0.0974	0.0012	0.8183	0.0154	0.0311	0.0004	1.0	636.5	38.9	599.3	6.9	607.1	8.6
57	0.1068	0.0020	0.3031	0.0038	4.4605	0.0845	0.0932	0.0012	0.6	1744.6	33.6	1706.5	18.8	1723.7	15.7
58	0.0720	0.0012	0.1691	0.0020	1.6791	0.0294	0.0524	0.0009	0.4	987.2	33.6	1007.0	11.3	1000.7	11.1
59	0.0678	0.0020	0.1454	0.0020	1.3599	0.0390	0.0439	0.0008	0.0	863.2	58.5	875.2	11.0	871.8	16.8
60	0.0722	0.0013	0.1665	0.0020	1.6576	0.0301	0.0498	0.0007	5.4	991.5	35.4	992.9	11.2	992.5	11.5
61	0.1745	0.0024	0.4434	0.0053	10.6713	0.1556	0.1314	0.0016	0.1	2601.5	22.6	2366.0	23.8	2494.9	13.5
62	0.0675	0.0010	0.1410	0.0017	1.3115	0.0204	0.0420	0.0006	1.6	852.1	30.4	850.2	9.4	850.8	9.0
63	0.0709	0.0018	0.1689	0.0022	1.6516	0.0414	0.0516	0.0007	0.1	955.5	50.2	1005.8	12.1	990.1	15.8
64	0.0734	0.0013	0.1725	0.0021	1.7453	0.0320	0.0522	0.0006	6.4	1024.1	35.6	1026.1	11.6	1025.4	11.8
65	0.0646	0.0022	0.0950	0.0013	0.8462	0.0288	0.0307	0.0005	3.4	761.6	70.8	584.9	7.8	622.5	15.9
66	0.0680	0.0012	0.1268	0.0015	1.1895	0.0216	0.0403	0.0006	0.2	869.1	36.1	769.8	8.8	795.7	10.0
67	0.0602	0.0012	0.0981	0.0012	0.8143	0.0167	0.0313	0.0005	2.4	610.3	42.9	603.4	7.0	604.9	9.3
68	0.0621	0.0014	0.0995	0.0012	0.8517	0.0190	0.0310	0.0005	3.5	678.0	46.3	611.2	7.3	625.6	10.4
69	0.0561	0.0011	0.0905	0.0011	0.7003	0.0135	0.0285	0.0004	2.7	457.4	41.0	558.4	6.5	539.0	8.1
70	0.0609	0.0014	0.0909	0.0011	0.7635	0.0176	0.0288	0.0004	2.4	637.0	48.4	560.7	6.7	576.0	10.1
71	0.0725	0.0014	0.1548	0.0019	1.5483	0.0299	0.0503	0.0006	1.3	1001.0	37.9	927.9	10.6	949.8	11.9
72	0.0628	0.0013	0.1086	0.0014	0.9406	0.0198	0.0341	0.0005	6.8	701.9	43.3	664.5	7.9	673.2	10.3
73	0.0725	0.0013	0.1326	0.0016	1.3254	0.0245	0.0421	0.0006	4.1	1000.3	36.2	802.5	9.2	856.9	10.7
74	0.0677	0.0018	0.1216	0.0016	1.1349	0.0308	0.0383	0.0006	5.7	859.7	55.5	739.5	9.2	770.1	14.7
75	0.1078	0.0018	0.2734	0.0034	4.0649	0.0709	0.0937	0.0013	1.3	1762.8	30.6	1558.2	17.0	1647.3	14.2
76	0.0601	0.0013	0.1055	0.0013	0.8744	0.0186	0.0323	0.0005	1.0	608.6	44.7	646.3	7.6	637.9	10.1
77	0.0643	0.0009	0.1181	0.0014	1.0466	0.0162	0.0368	0.0005	4.3	750.1	30.7	719.8	8.0	727.2	8.0
78	0.0485	0.0027	0.0043	0.0001	0.0290	0.0016	0.0013	0.0000	1.9	124.0	127.3	27.9	0.4	29.1	1.6
79	0.0687	0.0013	0.1378	0.0017	1.3052	0.0258	0.0435	0.0006	9.6	889.3	39.5	832.2	9.7	848.0	11.4
80	0.1054	0.0015	0.2417	0.0028	3.5119	0.0515	0.0704	0.0009	5.1	1721.2	25.2	1395.3	14.8	1529.9	11.6
81	0.1101	0.0015	0.2848	0.0033	4.3241	0.0623	0.0850	0.0011	3.4	1801.3	24.4	1615.4	16.8	1698.0	11.9
82	0.0634	0.0010	0.1017	0.0012	0.8886	0.0151	0.0332	0.0005	1.9	719.9	34.2	624.6	7.1	645.6	8.1
83	0.0614	0.0016	0.0976	0.0013	0.8261	0.0217	0.0304	0.0005	0.4	653.9	55.4	600.0	7.4	611.5	12.1
84	0.0632	0.0014	0.1157	0.0014	1.0083	0.0218	0.0409	0.0008	0.3	715.7	44.8	705.5	8.3	708.0	11.0

Appendix B. Results of single grain zircon U-Pb ICP-MS analysis from Thera (Santorini), Greece

Grain no.	Measured ratios									Apparent ages (Ma)					
	$^{207}Pb/^{206}Pb$	1σ	$^{206}Pb/^{238}U$	1σ	$^{207}Pb/^{235}U$	1σ	$^{208}Pb/^{232}Th$	1σ	Discordance (%)	$^{207}Pb/^{206}Pb$	1σ	$^{206}Pb/^{238}U$	1σ	$^{207}Pb/^{235}U$	1σ
85	0.0620	0.0013	0.1088	0.0013	0.9305	0.0195	0.0331	0.0005	1.8	675.0	43.5	665.7	7.8	667.9	10.3
86	0.0749	0.0023	0.1694	0.0024	1.7494	0.0533	0.0506	0.0010	1.4	1065.2	60.6	1009.0	13.0	1026.9	19.7
87	0.0598	0.0012	0.1042	0.0013	0.8596	0.0171	0.0334	0.0005	0.6	597.6	41.6	638.9	7.5	629.9	9.3
88	0.0603	0.0022	0.0973	0.0014	0.8091	0.0296	0.0296	0.0006	4.9	615.0	78.0	598.5	8.1	601.9	16.6
90	0.0685	0.0019	0.1221	0.0016	1.1533	0.0321	0.0386	0.0008	0.6	884.6	56.7	742.4	9.3	778.8	15.1
91	0.0667	0.0012	0.1340	0.0016	1.2321	0.0225	0.0397	0.0007	7.2	827.9	36.6	810.7	9.2	815.3	10.2
92	0.0651	0.0012	0.0939	0.0011	0.8422	0.0156	0.0275	0.0004	0.5	776.0	37.5	578.5	6.7	620.4	8.6
93	0.0609	0.0013	0.1012	0.0013	0.8497	0.0181	0.0313	0.0005	0.5	635.7	44.6	621.4	7.3	624.5	9.9
95	0.0608	0.0013	0.1003	0.0013	0.8403	0.0187	0.0316	0.0005	18.8	631.3	46.9	616.0	7.3	619.3	10.3
96	0.1599	0.0022	0.3175	0.0038	7.0009	0.1024	0.1017	0.0013	1.0	2454.9	23.1	1777.4	18.4	2111.5	13.0
97a	0.1280	0.0019	0.3702	0.0044	6.5324	0.0999	0.1097	0.0014	10.3	2070.5	25.4	2030.1	20.7	2050.3	13.5
97b	0.1256	0.0018	0.3723	0.0045	6.4476	0.0999	0.1059	0.0015	1.2	2037.6	25.7	2040.0	21.1	2038.8	13.6
99	0.0827	0.0019	0.1595	0.0020	1.8196	0.0411	0.0547	0.0010	0.4	1263.2	43.2	954.0	11.3	1052.5	14.8
100	0.1866	0.0029	0.5194	0.0064	13.3638	0.2154	0.1448	0.0018	0.3	2712.6	25.3	2696.5	27.0	2705.7	15.2
102	0.0605	0.0022	0.1031	0.0014	0.8605	0.0303	0.0327	0.0006	2.5	623.1	75.0	632.4	8.4	630.4	16.6
103	0.1147	0.0017	0.3182	0.0038	5.0314	0.0762	0.0966	0.0013	3.6	1875.1	25.8	1780.8	18.3	1824.6	12.8
104	0.1798	0.0026	0.4716	0.0056	11.6925	0.1782	0.1384	0.0018	1.0	2651.1	24.0	2490.7	24.5	2580.1	14.3
105	0.0649	0.0017	0.1215	0.0016	1.0866	0.0292	0.0395	0.0007	6.3	769.5	55.6	739.3	9.1	746.9	14.2
106	0.1233	0.0018	0.3151	0.0037	5.3567	0.0817	0.0881	0.0011	0.3	2004.2	25.5	1765.9	18.3	1878.0	13.1
107	0.0585	0.0010	0.0873	0.0010	0.7036	0.0123	0.0276	0.0004	0.3	547.1	36.5	539.4	6.2	540.9	7.3
ALS11, meta-rhyolite, 360636 N, 4025605 E															
1	0.0497	0.0015	0.0374	0.0005	0.2563	0.0076	0.0127	0.0002	2.1	182.3	67.4	236.6	3.0	231.7	6.1
02a	0.0512	0.0011	0.0351	0.0004	0.2480	0.0052	0.0117	0.0002	1.1	250.4	46.6	222.5	2.7	225.0	4.2
02b	0.0524	0.0016	0.0378	0.0005	0.2732	0.0082	0.0117	0.0002	2.4	301.6	67.1	239.5	3.1	245.3	6.5
3	0.0514	0.0014	0.0366	0.0005	0.2594	0.0071	0.0122	0.0002	1.0	257.1	62.0	231.9	2.9	234.2	5.8
4	0.1139	0.0016	0.3420	0.0041	5.3730	0.0818	0.1072	0.0015	0.8	1863.0	25.7	1896.5	19.7	1880.6	13.0
5	0.0506	0.0011	0.0382	0.0005	0.2663	0.0059	0.0129	0.0002	0.7	224.1	49.9	241.4	2.9	239.7	4.8
7	0.0666	0.0019	0.0380	0.0005	0.3487	0.0100	0.0128	0.0002	26.4	825.1	58.7	240.3	3.2	303.8	7.5
8	0.0568	0.0011	0.0359	0.0004	0.2807	0.0053	0.0123	0.0002	10.6	481.2	40.8	227.2	2.7	251.2	4.2
9	0.0524	0.0012	0.0368	0.0005	0.2659	0.0061	0.0135	0.0002	2.8	304.4	50.2	232.8	2.9	239.4	4.9
10	0.0498	0.0013	0.0370	0.0005	0.2539	0.0065	0.0117	0.0002	1.9	184.3	57.8	234.2	2.9	229.8	5.2
11	0.0661	0.0013	0.1288	0.0016	1.1750	0.0231	0.0399	0.0006	1.0	810.8	39.7	781.3	9.1	789.0	10.8
12a	0.0674	0.0011	0.0947	0.0011	0.8803	0.0154	0.0370	0.0005	9.9	849.9	34.5	583.5	6.7	641.1	8.3
12b	0.0515	0.0009	0.0380	0.0005	0.2698	0.0051	0.0126	0.0002	1.0	264.4	41.5	240.3	2.9	242.6	4.1
13	0.0523	0.0016	0.0380	0.0005	0.2738	0.0085	0.0123	0.0002	2.3	299.5	69.6	240.1	3.1	245.7	6.8
15	0.0699	0.0014	0.1650	0.0021	1.5899	0.0325	0.0494	0.0008	1.9	925.0	40.6	984.5	11.4	966.2	12.7
18	0.0615	0.0010	0.1022	0.0012	0.8670	0.0140	0.0334	0.0005	1.0	657.1	32.7	627.4	7.1	633.9	7.6
19	0.0582	0.0023	0.0880	0.0013	0.7056	0.0280	0.0270	0.0007	0.3	535.7	85.9	543.6	7.6	542.1	16.7
20	0.0619	0.0011	0.1061	0.0013	0.9053	0.0165	0.0326	0.0005	0.7	671.0	37.3	649.9	7.5	654.5	8.8
21	0.0479	0.0016	0.0372	0.0005	0.2450	0.0084	0.0116	0.0002	5.4	90.6	80.5	235.1	3.1	222.5	6.8
22	0.0746	0.0013	0.1719	0.0021	1.7675	0.0321	0.0548	0.0008	1.1	1057.4	35.2	1022.4	11.6	1033.6	11.8
23	0.0503	0.0016	0.0370	0.0005	0.2568	0.0080	0.0120	0.0002	1.0	209.2	71.0	234.4	3.1	232.1	6.5
24	0.0622	0.0011	0.1187	0.0015	1.0174	0.0187	0.0366	0.0005	1.5	679.8	37.4	723.2	8.4	712.6	9.4
25	0.0710	0.0017	0.1502	0.0020	1.4693	0.0361	0.0463	0.0007	1.8	956.3	49.2	901.9	10.9	917.8	14.8
26	0.0502	0.0010	0.0381	0.0005	0.2641	0.0053	0.0122	0.0002	1.4	205.3	45.2	241.3	2.9	237.9	4.3
27	0.0517	0.0013	0.0371	0.0005	0.2646	0.0067	0.0120	0.0002	1.4	271.8	56.3	235.1	2.9	238.4	5.4
28	0.0512	0.0010	0.0370	0.0005	0.2611	0.0054	0.0120	0.0002	0.7	251.5	45.5	234.0	2.8	235.6	4.3
29	0.0498	0.0016	0.0361	0.0005	0.2477	0.0078	0.0120	0.0002	1.7	185.6	72.2	228.5	3.0	224.7	6.4
30	0.0496	0.0011	0.0369	0.0005	0.2521	0.0054	0.0120	0.0002	2.3	173.8	48.7	233.6	2.8	228.3	4.4
31	0.0819	0.0016	0.1089	0.0014	1.2287	0.0240	0.0649	0.0011	22.1	1241.9	36.8	666.3	7.9	813.8	10.9
32	0.0498	0.0010	0.0372	0.0005	0.2558	0.0053	0.0119	0.0002	1.9	187.5	46.1	235.7	2.9	231.3	4.3
33	0.0669	0.0014	0.1263	0.0016	1.1643	0.0244	0.0444	0.0013	2.3	834.6	42.3	766.4	9.0	783.9	11.4
34	0.0513	0.0010	0.0375	0.0005	0.2649	0.0052	0.0120	0.0002	0.6	253.6	43.2	237.1	2.8	238.6	4.2
35	0.0538	0.0011	0.0365	0.0005	0.2707	0.0058	0.0118	0.0002	5.2	361.6	46.8	231.2	2.8	243.3	4.6
36	0.0558	0.0021	0.0362	0.0005	0.2788	0.0103	0.0119	0.0002	8.8	444.9	80.9	229.4	3.1	249.7	8.2
37	0.1771	0.0027	0.4783	0.0058	11.6797	0.1844	0.1402	0.0020	2.3	2626.3	24.7	2519.9	25.4	2579.1	14.8
38	0.0527	0.0013	0.0369	0.0005	0.2683	0.0068	0.0122	0.0002	3.3	317.4	55.7	233.6	2.9	241.3	5.4
39a	0.0531	0.0018	0.0367	0.0005	0.2686	0.0092	0.0122	0.0002	4.0	332.6	76.4	232.4	3.1	241.6	7.4
39b	0.0490	0.0014	0.0375	0.0005	0.2534	0.0074	0.0124	0.0002	3.4	147.7	67.0	237.4	3.0	229.3	6.0
40	0.0640	0.0014	0.1131	0.0014	0.9980	0.0221	0.0378	0.0007	1.8	742.7	45.5	690.5	8.2	702.8	11.2
41	0.0762	0.0018	0.1800	0.0024	1.8911	0.0456	0.0530	0.0011	1.1	1101.3	47.2	1066.7	12.9	1078.0	16.0
42a	0.0570	0.0013	0.0903	0.0011	0.7098	0.0160	0.0284	0.0007	2.3	491.6	48.2	557.3	6.7	544.6	9.5
42b	0.0586	0.0010	0.0936	0.0011	0.7562	0.0129	0.0297	0.0009	0.9	552.3	35.3	576.9	6.6	571.8	7.5
43a	0.1762	0.0026	0.4955	0.0060	12.0365	0.1857	0.1390	0.0019	0.5	2617.6	24.0	2594.2	25.6	2607.3	14.5
43b	0.1805	0.0026	0.4946	0.0060	12.3078	0.1896	0.1437	0.0019	1.5	2657.6	23.8	2590.5	25.7	2628.2	14.5
44	0.0672	0.0011	0.1303	0.0016	1.2068	0.0212	0.0422	0.0006	1.8	843.5	34.7	789.6	9.0	803.7	9.7
45	0.0659	0.0017	0.0369	0.0005	0.3357	0.0086	0.0132	0.0002	25.7	804.1	52.7	233.9	3.0	293.9	6.6
46	0.2937	0.0045	0.7023	0.0086	28.4348	0.4591	0.1852	0.0028	0.1	3437.4	23.6	3429.4	32.7	3434.2	15.8
47	0.0520	0.0012	0.0377	0.0005	0.2701	0.0064	0.0122	0.0002	1.8	283.4	52.8	238.6	2.9	242.8	5.1
48	0.0517	0.0010	0.0370	0.0005	0.2635	0.0054	0.0121	0.0002	1.5	271.4	45.6	234.1	2.8	237.5	4.4
49	0.0513	0.0015	0.0365	0.0005	0.2582	0.0074	0.0118	0.0002	0.9	254.6	64.8	231.2	3.0	233.2	6.0
51	0.0505	0.0013	0.0376	0.0005	0.2615	0.0068	0.0119	0.0002	0.7	219.0	58.9	237.6	3.0	235.9	5.5
52	0.0588	0.0014	0.0380	0.0005	0.3079	0.0073	0.0125	0.0002	13.4	560.4	50.4	240.3	3.0	272.6	5.7
53	0.0509	0.0012	0.0369	0.0005	0.2585	0.0059	0.0120	0.0002	0.0	235.8	51.5	233.3	2.9	233.4	4.8
54	0.0543	0.0017	0.0373	0.0005	0.2789	0.0084	0.0117	0.0002	5.9	383.9	66.6	235.8	3.1	249.8	6.7
55	0.0536	0.0014	0.0369	0.0005	0.2723	0.0071	0.0118	0.0002	4.8	353.8	58.0	233.4	2.9	244.6	5.7
56	0.0497	0.0014	0.0383	0.0005	0.2620	0.0072	0.0122	0.0002	2.4	179.9	62.4	242.1	3.1	236.3	5.8
57	0.0503	0.0013	0.0366	0.0005	0.2537	0.0067	0.0119	0.0002	0.9	208.9	59.3	231.6	2.9	229.6	5.4
58	0.0528	0.0015	0.0376	0.0005	0.2733	0.0077	0.0121	0.0002	3.2	320.0	62.7	237.7	3.0	245.3	6.1
59	0.0519	0.0012	0.0376	0.0005	0.2690	0.0065	0.0120	0.0002	1.7	281.7	53.9	237.9	2.9	241.9	5.2
60	0.0522	0.0012	0.0378	0.0005	0.2721	0.0065	0.0121	0.0002	2.1	293.1	53.3	239.3	3.0	244.3	5.2
61	0.0708	0.0016	0.1510	0.0019	1.4748	0.0328	0.0474	0.0008	1.5	952.8	44.2	906.7	10.8	920.1	13.4
62	0.0508	0.0012	0.0370	0.0005	0.2592	0.0062	0.0119	0.0002	0.0	233.7	54.1	234.1	2.9	234.0	5.0
64	0.0622	0.0013	0.1141	0.0014	0.9779	0.0201	0.0366	0.0006	0.6	680.3	42.3	696.5	8.2	692.5	10.3
65	0.0661	0.0017	0.0990	0.0013	0.9023	0.0236	0.0314	0.0007	7.3	810.9	53.8	608.3	7.6	653.0	12.6
67	0.0508	0.0010	0.0377	0.0005	0.2634	0.0052	0.0123	0.0002	0.3	230.0	43.5	238.2	2.9	237.4	4.2
70	0.0519	0.0014	0.0376	0.0005	0.2687	0.0072	0.0119	0.0002	1.6	279.5	60.0	237.9	3.0	241.7	5.8
71	0.0498	0.0015	0.0380	0.0005	0.2605	0.0080	0.0130	0.0002	2.1	185.6	69.7	240.2	3.1	235.1	6.4
72	0.0710	0.0015	0.1089	0.0014	1.0649	0.0233	0.0325	0.0007	10.5	956.3	43.5	666.3	8.0	736.2	11.5
73	0.1717	0.0027	0.4398	0.0053	10.4060	0.1695	0.1228	0.0017	5.2	2573.9	25.6	2349.9	23.9	2471.6	15.1

Appendix B. Results of single grain zircon U-Pb ICP-MS analysis from Thera (Santorini), Greece

Grain no.	Measured ratios									Apparent ages (Ma)					
	$^{207}Pb/^{206}Pb$	1σ	$^{206}Pb/^{238}U$	1σ	$^{207}Pb/^{235}U$	1σ	$^{208}Pb/^{232}Th$	1σ	Discordance (%)	$^{207}Pb/^{206}Pb$	1σ	$^{206}Pb/^{238}U$	1σ	$^{207}Pb/^{235}U$	1σ
74	0.0496	0.0016	0.0393	0.0005	0.2681	0.0084	0.0121	0.0002	2.8	174.4	71.9	248.2	3.2	241.2	6.7
75	0.0506	0.0015	0.0373	0.0005	0.2599	0.0074	0.0118	0.0002	0.6	221.7	64.8	235.9	3.0	234.6	6.0
76	0.0539	0.0014	0.0360	0.0005	0.2669	0.0072	0.0118	0.0002	5.5	365.3	59.2	227.7	2.9	240.2	5.7
77	0.0510	0.0017	0.0372	0.0005	0.2618	0.0084	0.0120	0.0002	0.2	242.7	72.9	235.6	3.1	236.1	6.8
81	0.0646	0.0019	0.1187	0.0016	1.0559	0.0303	0.0413	0.0008	1.2	759.9	59.5	722.9	9.2	731.8	15.0
82	0.0640	0.0014	0.0972	0.0012	0.8568	0.0191	0.0319	0.0005	5.1	740.2	45.8	597.9	7.2	628.4	10.5
83	0.0520	0.0012	0.0376	0.0005	0.2693	0.0060	0.0122	0.0002	1.8	284.9	49.7	237.8	2.9	242.1	4.8
84	0.0675	0.0018	0.1645	0.0022	1.5301	0.0399	0.0506	0.0009	4.0	853.3	53.1	981.7	12.0	942.5	16.0
86	0.0566	0.0011	0.0935	0.0012	0.7291	0.0142	0.0298	0.0004	3.5	473.8	41.7	576.3	6.8	556.0	8.3
87	0.0521	0.0011	0.0364	0.0005	0.2615	0.0054	0.0117	0.0002	2.2	288.2	45.8	230.7	2.8	235.8	4.4
88	0.0718	0.0012	0.1602	0.0020	1.5839	0.0279	0.0531	0.0009	0.6	979.4	34.1	957.7	10.8	963.9	11.0
89	0.0536	0.0014	0.0386	0.0005	0.2853	0.0073	0.0126	0.0002	4.3	352.8	56.2	244.3	3.1	254.8	5.7
90	0.1215	0.0023	0.1987	0.0025	3.3271	0.0645	0.1163	0.0019	27.3	1978.3	33.4	1168.3	13.5	1487.4	15.1
91	0.0640	0.0018	0.0376	0.0005	0.3314	0.0095	0.0134	0.0002	22.2	741.1	59.5	237.8	3.1	290.7	7.2
92	0.0548	0.0010	0.0343	0.0004	0.2593	0.0049	0.0122	0.0002	7.6	404.0	40.4	217.6	2.6	234.1	4.0
93	0.0600	0.0013	0.1039	0.0013	0.8592	0.0186	0.0327	0.0005	1.2	603.0	45.5	637.4	7.6	629.7	10.2
94	0.0509	0.0016	0.0379	0.0005	0.2660	0.0081	0.0122	0.0002	0.2	234.8	68.9	240.1	3.1	239.5	6.5
97	0.0514	0.0013	0.0384	0.0005	0.2720	0.0069	0.0124	0.0002	0.6	257.8	57.0	242.9	3.1	244.3	5.5
99	0.0508	0.0012	0.0366	0.0005	0.2561	0.0062	0.0113	0.0002	0.1	231.7	54.0	231.7	2.9	231.5	5.0
100	0.0503	0.0011	0.0390	0.0005	0.2705	0.0058	0.0122	0.0002	1.5	209.3	48.4	246.7	3.0	243.1	4.7
101	0.0515	0.0014	0.0371	0.0005	0.2633	0.0073	0.0120	0.0002	1.1	263.6	62.3	234.8	3.0	237.3	5.9
102	0.0535	0.0016	0.0360	0.0005	0.2651	0.0079	0.0129	0.0002	4.8	347.8	66.2	227.9	3.0	238.8	6.4
103	0.0534	0.0013	0.0362	0.0005	0.2663	0.0065	0.0129	0.0002	4.7	347.1	53.0	228.9	2.9	239.7	5.2
104	0.0539	0.0014	0.0367	0.0005	0.2727	0.0072	0.0128	0.0002	5.4	368.5	58.1	232.3	3.0	244.9	5.8
105	0.0502	0.0014	0.0375	0.0005	0.2594	0.0073	0.0123	0.0002	1.3	202.8	63.6	237.4	3.0	234.2	5.9
106	0.0744	0.0015	0.1765	0.0022	1.8094	0.0378	0.0566	0.0010	0.1	1052.6	40.6	1047.7	12.2	1048.8	13.7
107	0.0531	0.0014	0.0360	0.0005	0.2633	0.0069	0.0123	0.0002	4.2	334.5	58.2	227.7	2.9	237.3	5.6
ALS13, conglomerate, 363067 N, 4025097 E															
1a	0.0641	0.0021	0.0823	0.0012	0.7265	0.0234	0.0305	0.0007	8.8	743.3	66.7	509.6	7.0	554.5	13.8
1b	0.0541	0.0012	0.0619	0.0008	0.4623	0.0103	0.0174	0.0007	0.4	376.4	47.8	387.4	4.9	385.9	7.1
2	0.0662	0.0015	0.1203	0.0016	1.0978	0.0251	0.0421	0.0008	2.7	812.2	45.9	732.3	9.1	752.3	12.1
3	0.0556	0.0019	0.0424	0.0006	0.3250	0.0112	0.0145	0.0003	6.8	437.6	75.3	267.5	3.7	285.8	8.6
5	0.0570	0.0015	0.0507	0.0007	0.3989	0.0105	0.0180	0.0004	6.8	491.5	56.9	319.1	4.2	340.9	7.6
6	0.1212	0.0026	0.3627	0.0048	6.0636	0.1321	0.1156	0.0022	0.5	1974.6	37.0	1994.9	22.6	1985.0	19.0
8	0.0548	0.0013	0.0626	0.0008	0.4731	0.0111	0.0218	0.0004	0.5	403.8	49.8	391.5	5.0	393.3	7.6
9	0.1759	0.0037	0.4737	0.0062	11.4881	0.2507	0.1447	0.0027	2.6	2614.4	34.6	2499.7	27.3	2563.6	20.4
11	0.0540	0.0045	0.0156	0.0003	0.1162	0.0095	0.0061	0.0002	11.7	369.7	177.6	99.9	2.0	111.6	8.7
12	0.0564	0.0013	0.0971	0.0013	0.7555	0.0176	0.0320	0.0005	4.4	468.6	50.2	597.6	7.4	571.4	10.2
13	0.0494	0.0010	0.0414	0.0005	0.2815	0.0061	0.0143	0.0002	3.6	165.4	48.4	261.2	3.3	251.8	4.8
14	0.0755	0.0015	0.1787	0.0023	1.8593	0.0380	0.0574	0.0010	0.6	1081.0	39.3	1059.9	12.6	1066.7	13.5
15	0.0374	0.0031	0.0044	0.0001	0.0229	0.0019	0.0015	0.0001	19.6	0.1	0.0	28.6	0.5	23.0	1.9
16	0.0583	0.0016	0.0878	0.0012	0.7056	0.0199	0.0306	0.0007	0.0	541.0	60.7	542.4	7.1	542.2	11.8
17	0.0570	0.0014	0.0704	0.0009	0.5530	0.0133	0.0246	0.0005	2.0	491.0	52.2	438.4	5.5	447.0	8.7
18	0.0602	0.0032	0.0155	0.0003	0.1286	0.0067	0.0064	0.0002	23.9	611.2	110.5	99.1	1.6	122.8	6.0
19	0.0503	0.0010	0.0468	0.0006	0.3248	0.0067	0.0157	0.0002	3.2	209.7	45.6	295.0	3.6	285.6	5.1
20	0.0538	0.0010	0.0465	0.0006	0.3450	0.0065	0.0160	0.0002	2.6	361.3	40.5	293.3	3.6	301.0	4.9
22	0.0493	0.0019	0.0175	0.0003	0.1187	0.0045	0.0067	0.0002	2.1	163.2	86.6	111.6	1.6	113.9	4.1
23	0.0599	0.0011	0.1150	0.0014	0.9490	0.0180	0.0376	0.0006	3.4	599.1	39.0	701.5	8.3	677.6	9.4
24	0.0521	0.0013	0.0509	0.0007	0.3653	0.0093	0.0181	0.0003	1.2	288.3	56.8	320.0	4.1	316.2	6.9
25	0.0542	0.0012	0.0516	0.0007	0.3857	0.0087	0.0167	0.0003	2.1	379.2	48.8	324.4	4.1	331.2	6.3
26	0.0553	0.0015	0.0495	0.0007	0.3771	0.0099	0.0177	0.0004	4.4	423.7	56.9	311.3	4.0	324.9	7.3
27	0.0516	0.0014	0.0353	0.0005	0.2511	0.0068	0.0130	0.0002	1.7	267.6	60.7	223.6	2.9	227.4	5.5
29	0.0527	0.0012	0.0515	0.0007	0.3741	0.0085	0.0192	0.0003	0.4	314.1	50.0	323.9	4.0	322.7	6.3
30	0.0532	0.0013	0.0513	0.0007	0.3766	0.0094	0.0151	0.0003	0.6	337.8	54.8	322.7	4.1	324.6	6.9
31	0.0484	0.0022	0.0182	0.0003	0.1216	0.0055	0.0057	0.0002	0.0	117.4	104.4	116.5	1.7	116.5	5.0
32	0.0595	0.0010	0.1012	0.0013	0.8303	0.0151	0.0317	0.0005	1.2	586.3	37.6	621.4	7.3	613.8	8.4
33	0.0521	0.0012	0.0405	0.0005	0.2911	0.0069	0.0137	0.0003	1.4	291.5	52.9	256.0	3.3	259.5	5.5
35	0.0619	0.0012	0.0516	0.0006	0.4401	0.0085	0.0188	0.0003	14.3	671.3	39.6	324.1	3.9	370.3	6.0
36	0.0534	0.0010	0.0520	0.0007	0.3824	0.0074	0.0176	0.0003	0.7	344.5	41.5	326.6	4.0	328.8	5.4
37	0.0528	0.0013	0.0393	0.0005	0.2860	0.0072	0.0136	0.0002	2.8	319.7	55.3	248.5	3.2	255.4	5.7
38	0.0531	0.0011	0.0535	0.0007	0.3914	0.0081	0.0181	0.0003	0.1	332.6	44.8	335.8	4.1	335.4	5.9
39	0.0532	0.0011	0.0574	0.0007	0.4208	0.0088	0.0196	0.0003	0.9	336.4	45.4	359.8	4.4	356.6	6.3
40	0.0552	0.0015	0.0478	0.0006	0.3642	0.0101	0.0151	0.0003	4.7	421.4	59.7	301.2	3.9	315.4	7.5
41	0.0575	0.0014	0.0666	0.0009	0.5279	0.0128	0.0327	0.0006	3.5	509.8	52.0	415.7	5.3	430.4	8.5
42	0.0506	0.0016	0.0378	0.0005	0.2636	0.0081	0.0127	0.0003	0.7	222.2	69.6	239.2	3.2	237.6	6.5
43	0.0504	0.0014	0.0390	0.0005	0.2706	0.0077	0.0140	0.0003	1.3	212.4	64.4	246.4	3.2	243.1	6.1
44	0.0518	0.0019	0.0478	0.0007	0.3414	0.0127	0.0155	0.0004	1.0	275.4	83.6	301.2	4.2	298.2	9.6
45	0.0603	0.0066	0.0289	0.0007	0.2402	0.0260	0.0124	0.0007	19.0	614.8	221.0	183.6	4.3	218.5	21.3
46	0.0562	0.0015	0.0404	0.0005	0.3129	0.0082	0.0115	0.0002	8.3	458.9	57.6	255.3	3.3	276.5	6.4
47	0.0545	0.0014	0.0498	0.0007	0.3738	0.0098	0.0165	0.0004	3.0	390.1	57.3	313.2	4.1	322.5	7.2
48	0.1269	0.0028	0.3965	0.0054	6.9366	0.1595	0.1210	0.0024	2.3	2055.0	39.0	2153.0	24.8	2103.3	20.4
49	0.0613	0.0013	0.0998	0.0013	0.8441	0.0188	0.0349	0.0006	1.3	651.1	46.3	613.4	7.5	621.4	10.4
51	0.0533	0.0019	0.0485	0.0006	0.3564	0.0122	0.0155	0.0003	1.4	342.7	76.4	305.2	3.8	309.5	9.1
52	0.0536	0.0016	0.0451	0.0006	0.3334	0.0095	0.0141	0.0003	2.7	353.8	63.9	284.4	3.4	292.1	7.3
53	0.1333	0.0018	0.3760	0.0042	6.9128	0.0976	0.1125	0.0014	2.1	2142.3	24.0	2057.6	19.7	2100.3	12.5
54	0.0804	0.0022	0.0524	0.0007	0.5810	0.0156	0.0224	0.0004	41.2	1205.8	53.0	329.4	4.1	465.1	10.0
55	0.0531	0.0022	0.0900	0.0012	0.6595	0.0269	0.0265	0.0006	7.5	334.5	90.8	555.7	7.2	514.3	16.5
56	0.0413	0.0022	0.0171	0.0002	0.0973	0.0052	0.0050	0.0001	13.7	0.1	0.0	109.2	1.5	94.2	4.8
57	0.0679	0.0026	0.0469	0.0006	0.4393	0.0164	0.0187	0.0004	25.0	865.0	76.9	295.7	3.9	369.7	11.6
58	0.0559	0.0012	0.0515	0.0006	0.3967	0.0082	0.0139	0.0002	4.9	449.0	45.1	323.4	3.7	339.2	6.0
59	0.1306	0.0017	0.3617	0.0040	6.5115	0.0874	0.1155	0.0014	2.9	2105.8	22.5	1990.4	19.1	2047.5	11.8
60	0.0549	0.0011	0.0736	0.0008	0.5564	0.0114	0.0229	0.0005	1.8	406.6	45.0	457.6	5.1	449.2	7.4
63	0.1124	0.0019	0.2801	0.0033	4.3417	0.0724	0.0878	0.0011	6.9	1838.8	29.7	1591.8	16.4	1701.3	13.8
64	0.0516	0.0008	0.0538	0.0006	0.3824	0.0059	0.0155	0.0002	2.6	266.5	34.3	337.7	3.7	328.8	4.3
65	0.0525	0.0012	0.0509	0.0006	0.3686	0.0085	0.0157	0.0003	0.5	307.7	52.1	320.2	3.6	318.6	6.3
66	0.0523	0.0009	0.0520	0.0006	0.3751	0.0062	0.0159	0.0002	1.0	299.2	36.6	326.8	3.6	323.4	4.6
67	0.0516	0.0013	0.0439	0.0005	0.3121	0.0075	0.0128	0.0002	0.4	265.7	54.7	277.0	3.2	275.8	5.8
68	0.0738	0.0011	0.1503	0.0017	1.5295	0.0241	0.0497	0.0007	4.4	1037.0	30.9	902.4	9.5	942.3	9.7
69	0.0621	0.0023	0.0459	0.0006	0.3929	0.0146	0.0169	0.0004	16.3	677.0	78.3	289.3	3.8	336.5	10.6
70	0.0505	0.0015	0.0423	0.0005	0.2945	0.0085	0.0129	0.0003	1.8	219.2	66.0	266.9	3.2	262.1	6.7

Appendix B. Results of single grain zircon U-Pb ICP-MS analysis from Thera (Santorini), Greece

Grain no.	Measured ratios									Apparent ages (Ma)					
	$^{207}Pb/^{206}Pb$	1σ	$^{206}Pb/^{238}U$	1σ	$^{207}Pb/^{235}U$	1σ	$^{208}Pb/^{232}Th$	1σ	Discordance (%)	$^{207}Pb/^{206}Pb$	1σ	$^{206}Pb/^{238}U$	1σ	$^{207}Pb/^{235}U$	1σ
71	0.0519	0.0020	0.0333	0.0004	0.2384	0.0092	0.0104	0.0003	2.7	280.4	86.9	211.3	2.7	217.1	7.5
72	0.0535	0.0009	0.0544	0.0006	0.4012	0.0065	0.0166	0.0002	0.2	348.4	35.5	341.7	3.7	342.5	4.7
73	0.0569	0.0033	0.0496	0.0008	0.3894	0.0219	0.0159	0.0005	7.0	488.3	122.0	312.1	4.6	333.9	16.0
74	0.0489	0.0015	0.0524	0.0006	0.3535	0.0105	0.0156	0.0003	6.6	144.7	68.7	329.2	3.9	307.4	7.9
75	0.0552	0.0012	0.0716	0.0008	0.5445	0.0122	0.0229	0.0004	0.9	419.4	48.7	445.5	5.0	441.4	8.0
77	0.0519	0.0016	0.0430	0.0005	0.3076	0.0094	0.0128	0.0002	0.4	282.2	68.8	271.2	3.3	272.3	7.3
78	0.0741	0.0010	0.0453	0.0005	0.4626	0.0065	0.0205	0.0003	35.1	1042.7	27.4	285.7	3.1	386.1	4.5
79	0.0487	0.0020	0.0455	0.0006	0.3060	0.0123	0.0145	0.0003	5.6	134.4	93.0	287.1	3.7	271.0	9.6
80	0.0557	0.0032	0.0443	0.0007	0.3405	0.0194	0.0143	0.0004	6.4	440.6	124.1	279.6	4.2	297.5	14.7
81	0.0547	0.0016	0.0446	0.0006	0.3368	0.0096	0.0136	0.0002	4.7	400.1	63.1	281.6	3.4	294.8	7.3
82	0.0538	0.0015	0.0441	0.0005	0.3268	0.0092	0.0135	0.0002	3.2	361.6	62.9	278.1	3.3	287.1	7.0
83	0.0542	0.0016	0.0441	0.0006	0.3297	0.0098	0.0140	0.0003	4.0	380.3	66.1	278.2	3.4	289.3	7.5
84	0.0395	0.0045	0.0443	0.0008	0.2412	0.0271	0.0133	0.0005	21.6	0.1	0.0	279.7	4.8	219.4	22.1
85	0.0553	0.0020	0.0458	0.0006	0.3485	0.0126	0.0147	0.0003	5.3	422.8	79.5	288.4	3.7	303.6	9.5
86	0.1076	0.0015	0.2451	0.0027	3.6374	0.0513	0.0841	0.0010	10.2	1759.8	24.9	1412.9	14.1	1557.7	11.2
87	0.1168	0.0021	0.1730	0.0021	2.7841	0.0504	0.0872	0.0012	31.4	1907.0	32.2	1028.4	11.3	1351.3	13.5
88	0.0525	0.0012	0.0495	0.0006	0.3583	0.0082	0.0156	0.0002	0.2	305.6	51.0	311.6	3.6	310.9	6.1
89	0.0585	0.0010	0.0947	0.0011	0.7639	0.0127	0.0324	0.0006	1.2	547.5	35.7	583.4	6.2	576.2	7.3
90	0.0593	0.0043	0.0850	0.0015	0.6939	0.0501	0.0266	0.0012	1.8	576.5	151.6	525.6	8.7	535.1	30.1
91	0.0598	0.0016	0.1037	0.0013	0.8549	0.0228	0.0312	0.0004	1.4	595.3	57.9	636.1	7.4	627.3	12.5
92	0.0581	0.0013	0.0953	0.0011	0.7635	0.0174	0.0283	0.0004	1.9	532.5	49.5	587.0	6.7	576.0	10.0
93	0.0508	0.0014	0.0432	0.0005	0.3029	0.0084	0.0130	0.0002	1.5	233.3	63.5	272.8	3.2	268.7	6.6
94	0.0595	0.0011	0.0452	0.0005	0.3705	0.0071	0.0164	0.0003	12.4	586.3	40.7	284.7	3.2	320.0	5.2
95	0.1967	0.0026	0.4851	0.0054	13.1528	0.1786	0.1366	0.0017	5.5	2798.7	21.3	2549.5	23.5	2690.7	12.8
96	0.0569	0.0017	0.0560	0.0007	0.4393	0.0126	0.0163	0.0003	5.2	485.9	63.5	351.4	4.2	369.8	8.9
97	0.1946	0.0025	0.5214	0.0057	13.9867	0.1847	0.1352	0.0016	1.6	2781.2	20.7	2705.1	24.3	2748.8	12.5
100	0.0483	0.0025	0.0335	0.0005	0.2234	0.0112	0.0101	0.0002	3.7	114.4	115.5	212.6	2.9	204.7	9.3
101	-0.0241	0.0572	0.0187	0.0036	-0.0612	0.1450	0.0224	0.0091	153.6	0.1	0.0	119.5	23.0	-64.1	156.8
102	0.0660	0.0042	0.1059	0.0018	0.9636	0.0607	0.0338	0.0010	5.6	807.3	128.3	648.6	10.3	685.1	31.4
103	0.0524	0.0022	0.0494	0.0007	0.3564	0.0149	0.0163	0.0004	0.4	301.6	94.1	310.6	4.1	309.5	11.2
104	0.0521	0.0013	0.0452	0.0005	0.3245	0.0082	0.0139	0.0002	0.2	289.0	56.7	284.9	3.3	285.4	6.3
105	0.1298	0.0017	0.3952	0.0044	7.0732	0.0970	0.1066	0.0014	1.2	2095.4	23.1	2147.0	20.4	2120.7	12.2
115	0.1272	0.0021	0.3209	0.0040	5.6272	0.0989	0.0779	0.0012	7.0	2059.4	29.3	1794.2	19.4	1920.3	15.2
116	0.0742	0.0018	0.0405	0.0006	0.4148	0.0102	0.0206	0.0004	37.6	1047.9	47.6	256.1	3.4	352.3	7.3
ALS16, quartzite, 363102 N, 4025730 E															
3	0.0580	0.0058	0.0367	0.0008	0.2931	0.0289	0.0123	0.0007	12.5	528.1	204.9	232.1	4.6	261.0	22.7
4	0.0566	0.0013	0.1057	0.0014	0.8248	0.0193	0.0378	0.0007	5.7	474.1	50.2	647.8	7.9	610.7	10.7
5	0.0661	0.0013	0.1095	0.0014	0.9974	0.0203	0.0395	0.0007	4.9	807.9	40.6	669.8	8.1	702.5	10.3
6	0.0599	0.0014	0.0853	0.0011	0.7039	0.0164	0.0351	0.0006	2.6	598.4	48.6	527.5	6.5	541.1	9.8
7	0.0523	0.0016	0.0357	0.0005	0.2571	0.0077	0.0128	0.0002	2.9	297.9	66.8	225.9	3.0	232.4	6.3
8	0.0561	0.0010	0.0676	0.0008	0.5232	0.0094	0.0228	0.0004	1.3	455.5	37.3	421.9	5.0	427.3	6.3
13	0.0818	0.0022	0.1898	0.0026	2.1395	0.0581	0.0703	0.0014	3.7	1239.5	52.0	1120.2	14.2	1161.7	18.8
14	0.0755	0.0038	0.1738	0.0030	1.8090	0.0891	0.0597	0.0008	1.5	1081.4	97.0	1032.8	16.3	1048.7	32.2
15	0.0515	0.0015	0.0526	0.0007	0.3735	0.0109	0.0189	0.0004	2.4	263.8	64.9	330.3	4.3	322.3	8.0
16	0.0516	0.0020	0.0474	0.0007	0.3371	0.0127	0.0182	0.0004	1.2	265.8	84.7	298.6	4.1	295.0	9.7
17	0.1270	0.0018	0.3814	0.0047	6.6806	0.1028	0.1363	0.0020	0.6	2057.0	24.9	2083.0	21.9	2070.1	13.6
21	0.0554	0.0012	0.0517	0.0007	0.3953	0.0090	0.0183	0.0003	4.1	428.7	48.4	325.1	4.1	338.3	6.6
22	0.1863	0.0025	0.4882	0.0060	12.5420	0.1831	0.1477	0.0019	3.2	2709.7	21.7	2562.8	26.0	2645.9	13.7
23	0.0547	0.0009	0.0524	0.0007	0.3952	0.0070	0.0199	0.0003	2.8	400.1	37.5	329.1	4.0	338.2	5.1
30	0.0714	0.0028	0.0378	0.0006	0.3725	0.0145	0.0160	0.0004	34.3	968.1	78.2	239.4	3.5	321.5	10.7
32	0.0584	0.0015	0.0767	0.0010	0.6174	0.0162	0.0279	0.0006	2.4	542.8	56.0	476.6	6.0	488.2	10.2
33	0.0614	0.0014	0.1046	0.0014	0.8849	0.0204	0.0385	0.0006	0.4	652.1	47.6	641.1	7.9	643.6	11.0
34	0.0560	0.0019	0.0517	0.0007	0.3989	0.0133	0.0173	0.0005	5.0	452.5	72.4	324.6	4.4	340.9	9.6
35	0.0594	0.0064	0.1172	0.0026	0.9600	0.1016	0.0398	0.0037	4.3	582.5	217.0	714.1	15.3	683.3	52.6
36	0.0630	0.0010	0.1152	0.0014	1.0013	0.0168	0.0382	0.0006	0.2	709.6	33.2	702.8	8.2	704.5	8.5
37	0.0688	0.0012	0.1504	0.0019	1.4261	0.0262	0.0502	0.0007	0.3	892.3	35.8	902.9	10.5	899.9	11.0
39	0.0566	0.0011	0.0670	0.0008	0.5222	0.0106	0.0232	0.0004	2.1	473.4	43.3	417.9	5.1	426.6	7.1
40	0.0576	0.0015	0.0543	0.0007	0.4312	0.0110	0.0186	0.0003	6.9	515.8	54.6	340.6	4.3	364.0	7.8
41	0.0541	0.0010	0.0634	0.0008	0.4727	0.0088	0.0213	0.0003	0.7	375.4	39.8	396.0	4.7	393.1	6.1
42	0.0572	0.0010	0.0531	0.0007	0.4187	0.0075	0.0187	0.0003	6.6	499.8	36.9	333.2	4.0	355.1	5.4
43	0.0509	0.0013	0.0555	0.0007	0.3896	0.0098	0.0179	0.0004	4.0	237.9	56.3	348.0	4.4	334.1	7.2
44	0.0760	0.0017	0.0684	0.0009	0.7170	0.0165	0.0330	0.0006	28.7	1094.8	44.6	426.6	5.4	548.9	9.8
45	0.0535	0.0011	0.0544	0.0007	0.4017	0.0086	0.0178	0.0003	0.4	351.1	46.2	341.6	4.2	342.9	6.2
46a	0.0532	0.0017	0.0538	0.0007	0.3946	0.0124	0.0187	0.0004	0.1	335.5	69.8	338.0	4.5	337.7	9.1
46b	0.0531	0.0013	0.0531	0.0007	0.3884	0.0098	0.0186	0.0003	0.0	332.0	55.4	333.3	4.2	333.2	7.2
47	0.0553	0.0013	0.0509	0.0007	0.3884	0.0091	0.0171	0.0003	4.0	423.9	50.1	320.3	4.0	333.2	6.7
52	0.1032	0.0016	0.2192	0.0027	3.1196	0.0509	0.0954	0.0014	12.5	1682.3	27.9	1277.9	14.4	1437.5	12.5
53	0.0536	0.0013	0.0534	0.0007	0.3944	0.0097	0.0183	0.0003	0.7	352.7	53.7	335.3	4.2	337.6	7.1
54	0.0539	0.0010	0.0544	0.0007	0.4041	0.0076	0.0186	0.0003	1.0	367.3	40.0	341.2	4.1	344.6	5.5
55	0.0595	0.0010	0.1054	0.0013	0.8655	0.0157	0.0375	0.0005	2.0	586.8	37.0	646.1	7.6	633.1	8.5
56	0.0539	0.0018	0.0386	0.0005	0.2863	0.0097	0.0136	0.0003	4.8	364.4	74.6	243.9	3.3	255.7	7.7
61	0.0520	0.0010	0.0527	0.0007	0.3778	0.0073	0.0208	0.0003	1.8	283.1	42.0	331.3	4.0	325.4	5.4
62	0.0495	0.0015	0.0372	0.0005	0.2540	0.0076	0.0159	0.0003	2.5	170.0	68.1	235.7	3.1	229.9	6.2
63	0.1809	0.0024	0.5203	0.0064	12.9801	0.1920	0.1861	0.0025	0.8	2661.4	22.2	2700.3	27.0	2678.2	13.9
64	0.0531	0.0011	0.0550	0.0007	0.4024	0.0083	0.0192	0.0003	0.4	333.3	44.5	344.8	4.2	343.4	6.0
65	0.0516	0.0015	0.0527	0.0007	0.3749	0.0109	0.0189	0.0003	2.3	269.2	65.3	330.8	4.3	323.3	8.1
66	0.0532	0.0013	0.0526	0.0007	0.3862	0.0093	0.0199	0.0004	0.3	338.7	52.9	330.5	4.2	331.6	6.8
67	0.0519	0.0018	0.0378	0.0005	0.2699	0.0092	0.0154	0.0003	1.6	279.1	75.7	238.8	3.2	242.6	7.3
68	0.0562	0.0011	0.0525	0.0007	0.4071	0.0080	0.0206	0.0003	5.2	461.0	41.6	329.8	4.0	346.8	5.8
72	0.0511	0.0010	0.0415	0.0005	0.2926	0.0059	0.0143	0.0002	0.6	245.1	43.8	262.3	3.2	260.6	4.6
73	0.0509	0.0016	0.0377	0.0005	0.2644	0.0084	0.0132	0.0003	0.1	235.1	71.6	238.5	3.2	238.2	6.7
76	0.0548	0.0013	0.0524	0.0007	0.3956	0.0093	0.0177	0.0003	2.8	402.7	50.7	329.1	4.1	338.4	6.8
77	0.1114	0.0016	0.2561	0.0032	3.9363	0.0615	0.0997	0.0014	10.3	1823.0	26.0	1470.1	16.2	1621.2	12.7
81	0.0496	0.0011	0.0238	0.0003	0.1626	0.0036	0.0083	0.0001	1.1	178.0	49.5	151.4	1.9	153.0	3.1
82	0.0537	0.0009	0.0668	0.0008	0.4946	0.0084	0.0233	0.0004	2.1	357.7	35.8	416.9	5.0	408.1	5.7
83	0.0573	0.0011	0.0717	0.0009	0.5660	0.0109	0.0291	0.0006	2.1	501.6	39.8	446.2	5.4	455.4	7.1
84	0.0531	0.0012	0.0390	0.0005	0.2859	0.0068	0.0149	0.0002	3.4	333.1	51.9	246.9	3.1	255.3	5.4
ALS17, schist, 363135 N, 4025970 E															
1	0.0568	0.0014	0.0735	0.0009	0.5754	0.0141	0.0227	0.0004	0.9	481.4	53.8	457.4	5.3	461.5	9.1
2	0.0517	0.0011	0.0512	0.0006	0.3642	0.0078	0.0161	0.0003	1.9	269.8	48.6	321.6	3.7	315.4	5.8

Appendix B. Results of single grain zircon U-Pb ICP-MS analysis from Thera (Santorini), Greece

Grain no.	Measured ratios									Apparent ages (Ma)					
	$^{207}Pb/^{206}Pb$	1σ	$^{206}Pb/^{238}U$	1σ	$^{207}Pb/^{235}U$	1σ	$^{208}Pb/^{232}Th$	1σ	Discordance (%)	$^{207}Pb/^{206}Pb$	1σ	$^{206}Pb/^{238}U$	1σ	$^{207}Pb/^{235}U$	1σ
3	0.0534	0.0014	0.0518	0.0006	0.3816	0.0099	0.0172	0.0003	0.8	346.0	58.0	325.7	3.8	328.2	7.3
4	0.0686	0.0012	0.1413	0.0016	1.3356	0.0242	0.0442	0.0007	1.1	885.4	36.8	852.0	9.1	861.3	10.5
5	0.0713	0.0014	0.1398	0.0016	1.3737	0.0269	0.0434	0.0006	4.1	965.5	39.5	843.2	9.2	877.7	11.5
6	0.0621	0.0011	0.1112	0.0013	0.9527	0.0166	0.0333	0.0005	0.1	678.1	36.5	679.9	7.3	679.5	8.6
7	0.0616	0.0014	0.1109	0.0013	0.9415	0.0208	0.0332	0.0006	0.7	658.6	46.9	678.2	7.6	673.7	10.9
8	0.0538	0.0012	0.0554	0.0007	0.4112	0.0093	0.0168	0.0003	0.6	364.1	50.4	347.6	4.0	349.8	6.7
9	0.0562	0.0011	0.0774	0.0009	0.5994	0.0114	0.0234	0.0004	0.8	458.5	41.2	480.6	5.3	476.9	7.2
10	0.0565	0.0013	0.0486	0.0006	0.3783	0.0086	0.0148	0.0003	6.6	470.9	50.4	305.7	3.5	325.8	6.3
11	0.0528	0.0012	0.0512	0.0006	0.3726	0.0085	0.0156	0.0003	0.1	319.0	50.8	321.9	3.7	321.6	6.3
12	0.0795	0.0020	0.0477	0.0006	0.5228	0.0130	0.0168	0.0003	42.2	1185.7	49.0	300.2	3.6	427.0	8.7
13	0.0558	0.0014	0.0604	0.0007	0.4649	0.0118	0.0185	0.0003	2.5	444.6	55.8	378.1	4.4	387.6	8.2
14	0.0742	0.0014	0.1704	0.0020	1.7444	0.0335	0.0508	0.0008	1.0	1047.6	38.2	1014.5	10.9	1025.1	12.4
15	0.1113	0.0021	0.0592	0.0007	0.9088	0.0171	0.0540	0.0008	77.0	1820.7	33.8	370.8	4.2	656.4	9.1
16	0.0685	0.0015	0.0508	0.0006	0.4798	0.0101	0.0240	0.0004	24.6	884.7	43.1	319.3	3.7	397.9	6.9
18	0.0519	0.0011	0.0522	0.0006	0.3740	0.0077	0.0165	0.0003	1.7	282.0	46.0	328.3	3.7	322.6	5.7
19	0.0823	0.0016	0.2013	0.0024	2.2835	0.0433	0.0578	0.0009	2.1	1252.7	36.4	1182.0	12.6	1207.2	13.4
20	0.0726	0.0014	0.1653	0.0019	1.6549	0.0319	0.0499	0.0008	0.5	1003.2	38.5	986.1	10.6	991.4	12.2
21	0.0519	0.0014	0.0362	0.0004	0.2592	0.0069	0.0114	0.0002	2.0	281.2	60.3	229.4	2.8	234.1	5.6
22	0.1034	0.0022	0.1567	0.0019	2.2340	0.0479	0.0686	0.0011	27.0	1685.7	39.4	938.5	10.6	1191.8	15.0
23	0.2848	0.0050	0.0824	0.0010	3.2363	0.0566	0.1483	0.0022	187.1	3389.2	26.9	510.6	5.7	1465.9	13.6
24	0.0620	0.0014	0.1038	0.0012	0.8880	0.0196	0.0313	0.0005	1.4	675.6	46.7	636.6	7.2	645.3	10.6
25	0.0624	0.0017	0.0986	0.0012	0.8492	0.0230	0.0302	0.0006	2.9	689.1	57.4	606.4	7.2	624.2	12.7
26	0.0559	0.0012	0.0620	0.0007	0.4776	0.0102	0.0202	0.0004	2.2	446.6	46.8	387.8	4.4	396.4	7.0
27	0.0838	0.0015	0.2204	0.0025	2.5460	0.0457	0.0640	0.0010	0.1	1287.1	34.3	1284.2	13.4	1285.3	13.1
28	0.1187	0.0022	0.3396	0.0040	5.5597	0.1035	0.0973	0.0015	1.3	1937.3	32.8	1884.7	19.1	1909.9	16.0
29	0.0660	0.0021	0.1075	0.0014	0.9787	0.0307	0.0308	0.0006	5.2	806.6	65.0	658.4	8.2	692.9	15.7
30	0.0652	0.0014	0.0775	0.0009	0.6972	0.0148	0.0299	0.0006	11.6	782.2	44.0	481.2	5.5	537.1	8.8
31	0.0760	0.0019	0.0573	0.0007	0.6000	0.0144	0.0245	0.0004	32.9	1093.8	47.9	359.1	4.2	477.2	9.1
33	0.0526	0.0014	0.0365	0.0004	0.2644	0.0070	0.0115	0.0002	3.2	311.9	59.6	230.8	2.7	238.2	5.6
34	0.0589	0.0017	0.0993	0.0013	0.8066	0.0234	0.0309	0.0006	1.6	563.9	62.6	610.3	7.3	600.6	13.2
35	0.0541	0.0012	0.0564	0.0007	0.4208	0.0093	0.0171	0.0003	0.8	375.4	49.1	353.7	4.1	356.6	6.7
38	0.0778	0.0018	0.1717	0.0021	1.8408	0.0414	0.0538	0.0009	3.8	1140.8	44.4	1021.4	11.4	1060.1	14.8
51	0.0598	0.0018	0.0427	0.0005	0.3520	0.0104	0.0143	0.0002	13.7	597.7	63.5	269.4	3.3	306.2	7.8
52	0.1198	0.0016	0.3626	0.0040	5.9871	0.0837	0.1039	0.0013	1.0	1952.7	24.1	1994.5	19.1	1974.0	12.2
53	0.0480	0.0015	0.0332	0.0004	0.2195	0.0067	0.0103	0.0001	4.2	97.3	72.0	210.4	2.5	201.5	5.6
54	0.0514	0.0014	0.0515	0.0006	0.3650	0.0097	0.0164	0.0003	2.4	259.4	60.4	323.7	3.8	316.0	7.2
55	0.0532	0.0016	0.0372	0.0005	0.2727	0.0083	0.0118	0.0002	4.0	336.0	68.0	235.5	2.9	244.9	6.6
56	0.0503	0.0014	0.0529	0.0006	0.3667	0.0101	0.0167	0.0003	4.6	207.0	63.3	332.4	3.9	317.2	7.5
57	0.0652	0.0012	0.0662	0.0008	0.5944	0.0110	0.0354	0.0005	14.7	779.1	38.2	413.1	4.6	473.7	7.0
58	0.0550	0.0013	0.0558	0.0007	0.4232	0.0102	0.0194	0.0004	2.4	413.3	52.6	349.9	4.1	358.3	7.3
60	0.0720	0.0014	0.1536	0.0018	1.5259	0.0302	0.0466	0.0008	2.1	987.3	39.6	921.3	10.0	940.8	12.2
61	0.0743	0.0013	0.1793	0.0021	1.8377	0.0322	0.0540	0.0007	0.4	1050.5	34.5	1063.2	11.3	1059.0	11.5
62	0.0614	0.0012	0.0975	0.0011	0.8252	0.0159	0.0311	0.0004	1.9	653.7	40.6	599.5	6.6	611.0	8.8
63	0.0577	0.0012	0.1041	0.0012	0.8283	0.0166	0.0318	0.0005	4.0	518.5	43.4	638.4	7.1	612.7	9.2
64	0.0554	0.0011	0.0630	0.0007	0.4817	0.0097	0.0200	0.0003	1.3	429.5	43.8	394.0	4.4	399.2	6.7
65	0.0506	0.0023	0.0360	0.0005	0.2508	0.0114	0.0110	0.0002	0.2	221.6	102.6	227.7	3.1	227.2	9.2
66	0.0571	0.0015	0.0973	0.0012	0.7662	0.0201	0.0301	0.0004	3.5	495.0	57.7	598.7	6.9	577.6	11.5
67	0.0540	0.0011	0.0521	0.0006	0.3884	0.0076	0.0162	0.0003	1.7	372.1	43.0	327.7	3.7	333.2	5.5
68	0.0575	0.0014	0.0822	0.0010	0.6521	0.0156	0.0315	0.0007	0.1	511.9	52.3	509.2	5.9	509.8	9.6
69	0.0521	0.0010	0.0515	0.0006	0.3698	0.0070	0.0166	0.0003	1.2	291.4	42.1	323.4	3.6	319.5	5.2
70	0.0661	0.0013	0.1193	0.0014	1.0866	0.0214	0.0373	0.0005	2.8	808.9	40.7	726.3	8.0	746.8	10.4
71	0.0545	0.0012	0.0498	0.0006	0.3747	0.0082	0.0151	0.0002	3.1	393.4	48.0	313.5	3.6	323.1	6.0
72	0.0603	0.0014	0.1110	0.0013	0.9223	0.0218	0.0324	0.0005	2.2	614.0	50.6	678.2	7.7	663.5	11.5
73	0.0572	0.0016	0.0527	0.0006	0.4162	0.0112	0.0184	0.0004	6.6	500.2	59.1	331.3	3.9	353.3	8.0
74	0.0528	0.0031	0.0365	0.0005	0.2652	0.0155	0.0114	0.0003	3.5	318.6	129.0	230.8	3.4	238.9	12.5
75	0.0607	0.0011	0.1049	0.0012	0.8783	0.0162	0.0353	0.0008	0.5	628.8	39.3	643.2	6.9	640.1	8.8
76	0.0562	0.0013	0.0500	0.0006	0.3872	0.0086	0.0158	0.0003	5.7	460.0	49.1	314.3	3.6	332.3	6.3
77	0.0636	0.0010	0.1138	0.0013	0.9990	0.0165	0.0336	0.0005	1.2	729.7	34.3	695.0	7.4	703.3	8.4
78	0.1736	0.0027	0.4742	0.0055	11.3496	0.1809	0.1329	0.0021	2.0	2592.9	25.9	2501.8	24.2	2552.3	14.9
79	0.0595	0.0022	0.0512	0.0007	0.4194	0.0154	0.0162	0.0004	10.6	584.1	78.6	321.6	4.1	355.6	11.0
80	0.0520	0.0011	0.0501	0.0006	0.3589	0.0078	0.0157	0.0002	1.2	283.5	48.7	315.1	3.6	311.4	5.8
81	0.0568	0.0010	0.0729	0.0008	0.5709	0.0101	0.0227	0.0003	1.1	484.2	38.5	453.4	5.0	458.6	6.5
82	0.0564	0.0013	0.0724	0.0009	0.5627	0.0126	0.0227	0.0004	0.6	466.0	49.6	450.7	5.1	453.3	8.2
83	0.0525	0.0016	0.0506	0.0006	0.3664	0.0110	0.0167	0.0003	0.4	307.1	67.5	318.3	3.9	316.9	8.2
84	0.1794	0.0031	0.4840	0.0058	11.9737	0.2050	0.1306	0.0018	2.3	2647.6	28.0	2544.8	25.3	2602.4	16.1
85	0.0534	0.0016	0.0517	0.0006	0.3802	0.0114	0.0160	0.0003	0.8	344.6	66.9	324.7	3.9	327.2	8.4
86	0.0510	0.0016	0.0518	0.0006	0.3643	0.0114	0.0161	0.0003	3.1	240.8	71.3	325.6	4.0	315.4	8.5
87	0.0523	0.0023	0.0362	0.0005	0.2607	0.0115	0.0119	0.0003	2.7	298.0	99.1	229.0	3.1	235.2	9.3
89	0.1321	0.0022	0.3800	0.0045	6.9230	0.1180	0.1072	0.0016	1.2	2126.4	29.3	2076.4	20.8	2101.6	15.1
90	0.0658	0.0026	0.0953	0.0013	0.8650	0.0342	0.0354	0.0008	7.8	800.1	81.9	587.1	7.7	632.8	18.6
91	0.0538	0.0013	0.0508	0.0006	0.3770	0.0089	0.0160	0.0003	1.7	362.8	52.9	319.5	3.7	324.8	6.6
92	0.0496	0.0032	0.0506	0.0008	0.3458	0.0224	0.0155	0.0007	5.2	173.8	145.7	318.3	4.8	301.6	16.9
93	0.0651	0.0014	0.1304	0.0016	1.1695	0.0255	0.0401	0.0007	0.5	776.4	45.3	790.0	8.8	786.4	11.9
94	0.0735	0.0012	0.1720	0.0020	1.7423	0.0285	0.0507	0.0008	0.1	1027.3	31.8	1023.0	10.8	1024.3	10.5
95	0.0547	0.0018	0.0524	0.0007	0.3946	0.0130	0.0170	0.0004	2.7	398.8	72.0	328.9	4.1	337.7	9.4
96	0.0580	0.0012	0.0914	0.0011	0.7312	0.0155	0.0284	0.0004	1.2	529.6	46.1	564.0	6.3	557.3	9.1
97	0.1164	0.0019	0.3320	0.0038	5.3269	0.0859	0.0936	0.0013	1.4	1901.2	28.3	1848.0	18.4	1873.2	13.8
98	0.0554	0.0015	0.0515	0.0006	0.3932	0.0108	0.0165	0.0003	4.1	428.9	60.5	323.5	3.9	336.7	7.9
99	0.0529	0.0011	0.0522	0.0006	0.3803	0.0078	0.0163	0.0003	0.2	322.4	45.6	327.9	3.7	327.3	5.7
100	0.0555	0.0011	0.0586	0.0007	0.4481	0.0086	0.0180	0.0003	2.5	432.3	41.4	366.8	4.1	375.9	6.0
101	0.0607	0.0012	0.0674	0.0008	0.5641	0.0107	0.0641	0.0011	8.1	629.9	40.1	420.3	4.7	454.2	6.9
102	0.0536	0.0011	0.0510	0.0006	0.3771	0.0078	0.0164	0.0003	1.3	355.1	45.0	320.7	3.6	324.9	5.7
103	0.0728	0.0013	0.1577	0.0018	1.5822	0.0292	0.0498	0.0008	2.0	1007.8	36.8	943.9	10.1	963.2	11.5
104a	0.1262	0.0019	0.3578	0.0040	6.2237	0.0967	0.0943	0.0014	1.8	2045.3	26.7	1971.5	19.1	2007.8	13.6
104b	0.1240	0.0020	0.3529	0.0040	6.0333	0.0980	0.1008	0.0014	1.7	2014.7	28.2	1948.2	19.3	1980.7	14.2
105	0.0518	0.0013	0.0513	0.0006	0.3667	0.0090	0.0162	0.0003	1.7	277.6	55.7	322.6	3.8	317.2	6.7
107	0.0536	0.0012	0.0521	0.0006	0.3846	0.0089	0.0166	0.0003	1.0	353.8	51.6	327.1	3.8	330.4	6.5
109	0.0680	0.0015	0.0890	0.0011	0.8341	0.0184	0.0271	0.0004	12.1	867.7	45.4	549.6	6.3	615.9	10.2
111	0.0618	0.0016	0.0393	0.0005	0.3351	0.0086	0.0129	0.0002	18.0	667.8	54.5	248.6	3.0	293.4	6.6
112	0.0533	0.0020	0.0348	0.0005	0.2560	0.0095	0.0110	0.0002	4.8	340.9	82.9	220.8	2.8	231.4	7.7

Appendix B. Results of single grain zircon U-Pb ICP-MS analysis from Thera (Santorini), Greece

Grain no.	Measured ratios									Apparent ages (Ma)					
	$^{207}Pb/^{206}Pb$	1σ	$^{206}Pb/^{238}U$	1σ	$^{207}Pb/^{235}U$	1σ	$^{208}Pb/^{232}Th$	1σ	Discordance (%)	$^{207}Pb/^{206}Pb$	1σ	$^{206}Pb/^{238}U$	1σ	$^{207}Pb/^{235}U$	1σ
113	0.0608	0.0013	0.0945	0.0011	0.7915	0.0164	0.0293	0.0004	1.7	631.1	43.8	582.0	6.5	592.0	9.3
114	0.0692	0.0017	0.1477	0.0018	1.4099	0.0335	0.0450	0.0009	0.6	905.7	48.5	888.0	10.1	893.1	14.1
115	0.1605	0.0025	0.1007	0.0012	2.2287	0.0357	0.0580	0.0008	92.3	2460.4	26.5	618.8	6.8	1190.1	11.2
116	0.0590	0.0014	0.0776	0.0009	0.6313	0.0146	0.0228	0.0005	3.1	566.4	49.8	482.0	5.5	496.9	9.1
117	0.0611	0.0018	0.0997	0.0013	0.8399	0.0247	0.0303	0.0007	1.1	642.8	62.6	612.6	7.4	619.1	13.6
118	0.0568	0.0012	0.0636	0.0007	0.4979	0.0103	0.0195	0.0003	3.3	484.2	45.2	397.2	4.5	410.3	7.0
119	0.0595	0.0027	0.0336	0.0005	0.2756	0.0124	0.0111	0.0002	16.1	586.3	95.9	212.9	3.0	247.2	9.9
120	0.1346	0.0023	0.3561	0.0041	6.6096	0.1138	0.1099	0.0016	4.9	2158.7	29.6	1963.8	19.5	2060.6	15.2
121	0.0544	0.0012	0.0357	0.0004	0.2676	0.0060	0.0122	0.0002	6.6	388.3	49.3	225.9	2.6	240.8	4.8
122	0.0555	0.0011	0.0502	0.0006	0.3838	0.0079	0.0159	0.0002	4.5	431.5	44.8	315.6	3.6	329.9	5.8
123	0.0575	0.0012	0.0770	0.0009	0.6106	0.0125	0.0264	0.0008	1.1	509.8	44.6	478.4	5.4	483.9	7.9
124	0.1176	0.0018	0.3466	0.0039	5.6217	0.0890	0.0986	0.0013	0.1	1920.7	27.6	1918.1	18.7	1919.4	13.6
125	0.1801	0.0027	0.4673	0.0052	11.6036	0.1788	0.1289	0.0017	4.1	2653.6	24.9	2471.9	23.0	2573.0	14.4
126	0.0542	0.0010	0.0514	0.0006	0.3844	0.0072	0.0152	0.0002	2.2	379.1	41.2	323.3	3.6	330.3	5.3
127	0.0527	0.0011	0.0357	0.0004	0.2598	0.0055	0.0111	0.0002	3.6	316.8	47.4	226.4	2.6	234.5	4.4
128	0.0562	0.0015	0.0539	0.0007	0.4171	0.0107	0.0171	0.0003	4.7	458.0	56.3	338.2	4.0	354.0	7.7
129	0.0583	0.0012	0.0626	0.0007	0.5031	0.0100	0.0220	0.0004	5.8	541.6	43.7	391.1	4.4	413.8	6.8
130	0.0686	0.0014	0.0659	0.0008	0.6233	0.0130	0.0287	0.0005	19.5	886.0	42.9	411.5	4.7	491.9	8.2
133	0.0790	0.0016	0.0674	0.0008	0.7337	0.0146	0.0407	0.0007	32.9	1171.9	38.7	420.3	4.8	558.7	8.5
134	0.0630	0.0011	0.1093	0.0012	0.9494	0.0173	0.0333	0.0006	1.3	707.3	38.1	668.9	7.2	677.8	9.0

Appendix C. Cathode luminescence images of zircon from samples dated for U-Pb using ICP-MS

Sample: ALS02

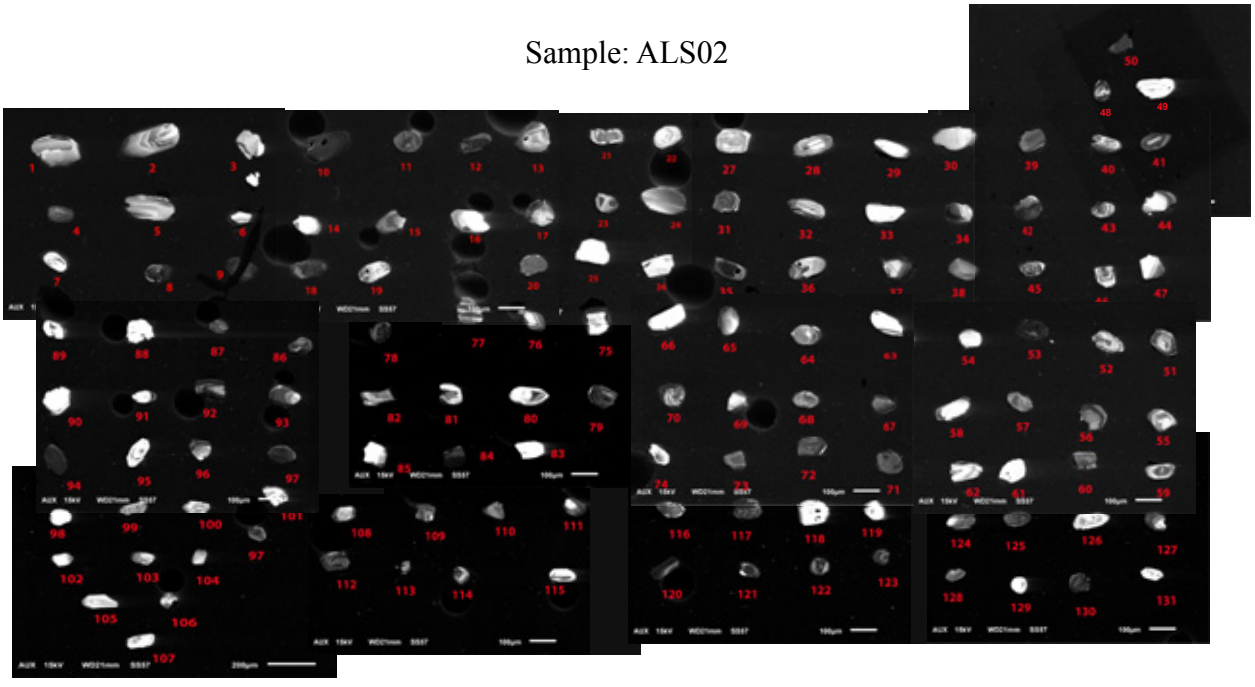

Sample: ALS03

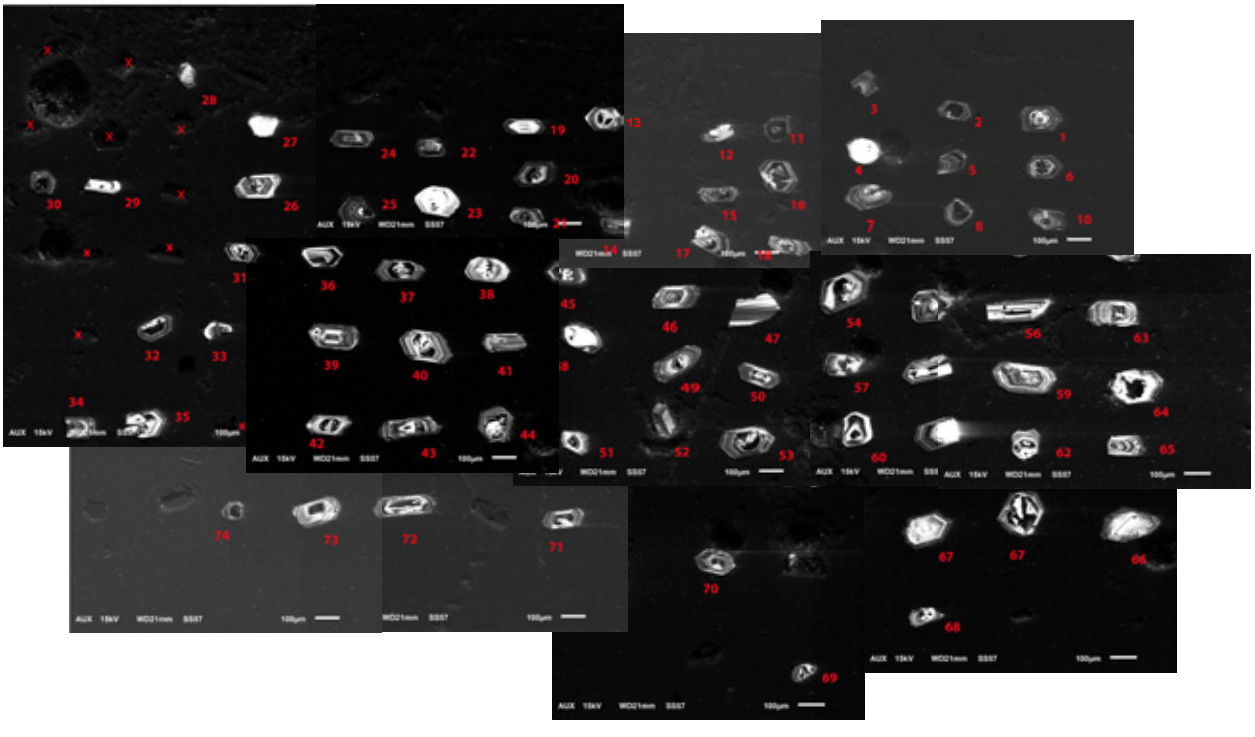

Sample: ALS05

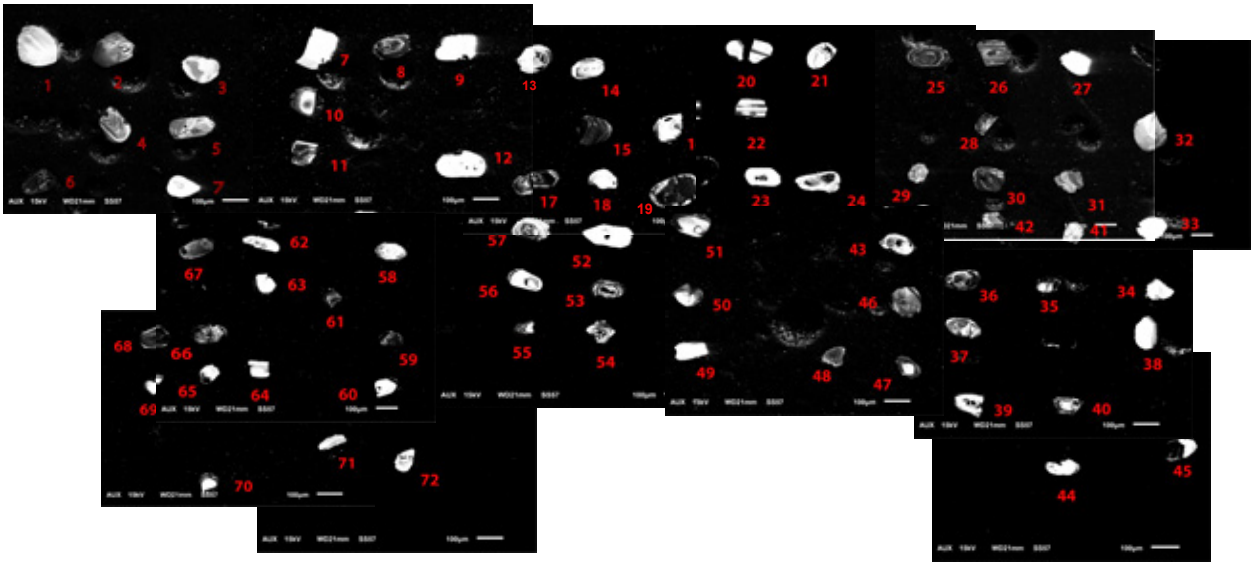

Sample: ALS08

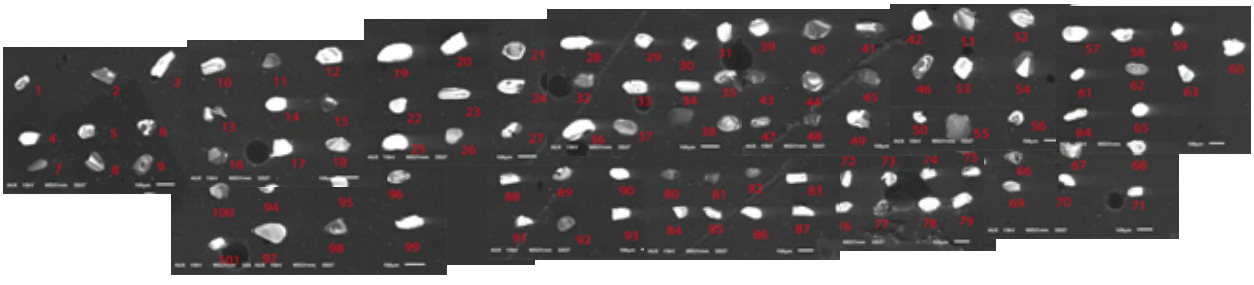

Sample: ALS11

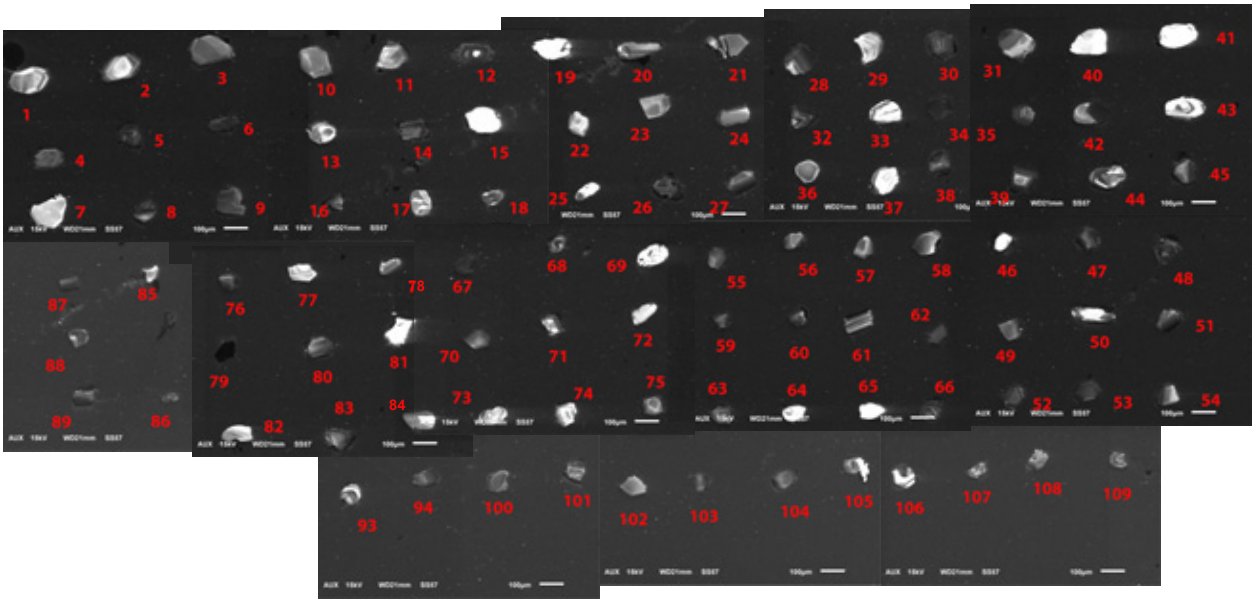

Sample: ALS13a[1]

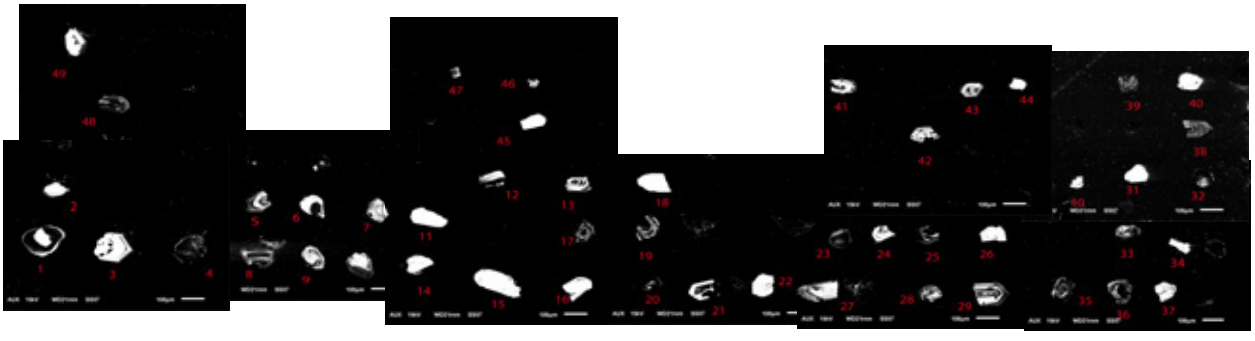

Sample: ALS13b[1]

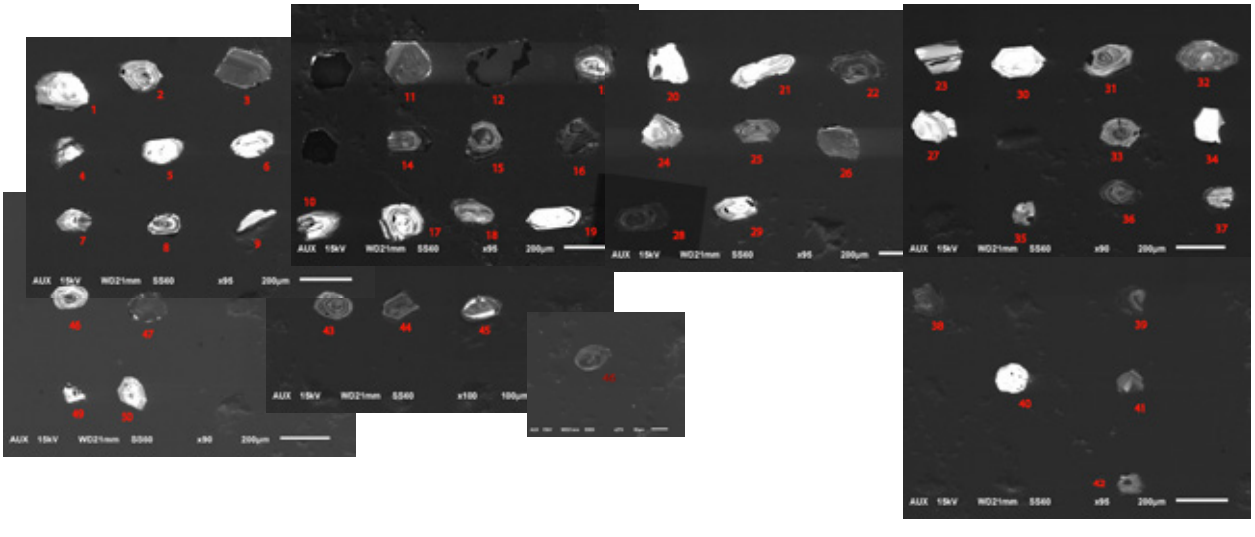

Sample: ALS16

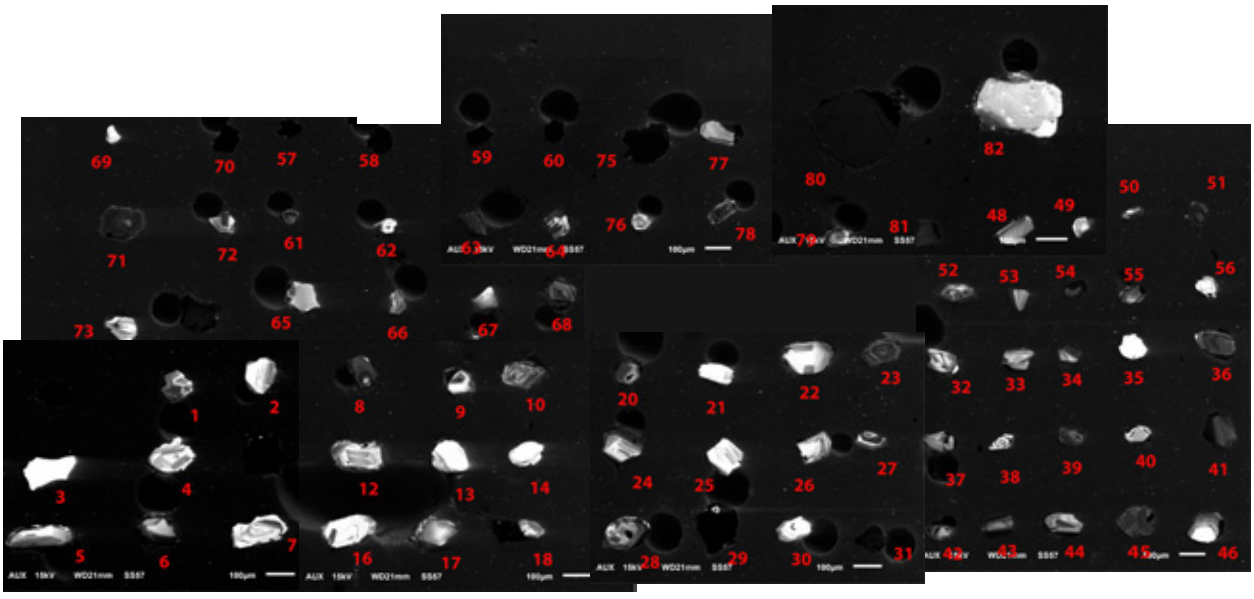

Sample: ALS17a[1]

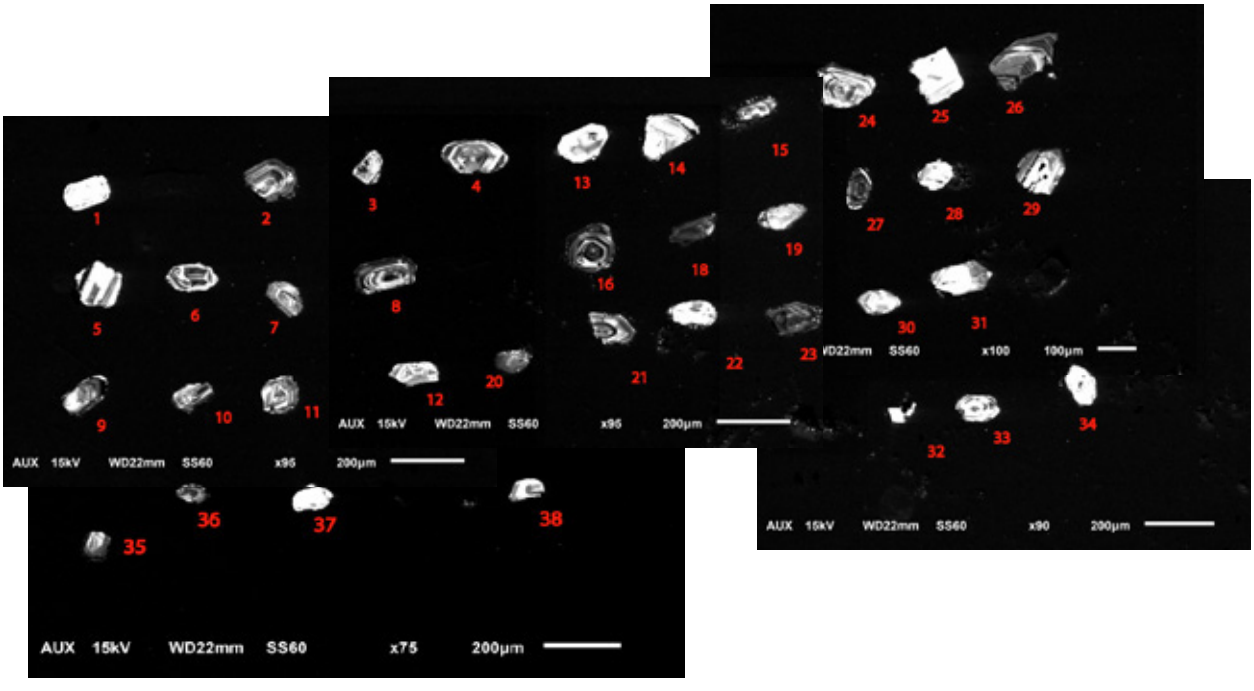

Sample: ALS17b[1]

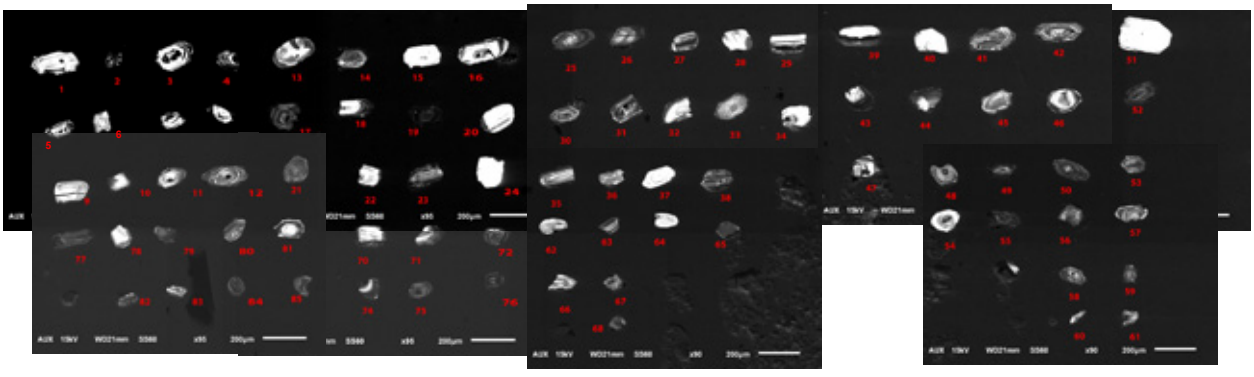

[1] In the case of samples ALS13 and ALS17, two batches of analyses were performed to account for loss of zircon during polishing phase.

Appendix D. Total fusion $^{40}Ar/^{39}Ar$ data of white mica from Thera (Santorini), Greece

Sample/grain	^{40}Ar	±1σ	^{39}Ar	±1σ	^{38}Ar†	±1σ	^{37}Ar†	±1σ	^{36}Ar	±1σ	$^{40}Ar/^{39}Ar$	±1σ	Age (Ma)	±1σ
ALS02, quartzite, 359540 N, 4027830 E, J = 0.0018668 ± 1.84E-06														
Grain 1	121.389	0.075	20.706	0.066	0.248	0.033	0.030	0.027	0.029	0.001	5.45	0.03	18.3	0.1
Grain 2	88.682	0.077	15.175	0.064	0.229	0.029	BDL	BDL	0.038	0.001	5.11	0.03	17.1	0.1
Grain 3	55.761	0.067	10.109	0.062	0.079	0.027	BDL	BDL	0.018	0.001	4.98	0.05	16.7	0.2
Grain 4	83.164	0.071	10.393	0.065	0.127	0.031	0.026	0.027	0.021	0.001	7.39	0.06	24.7	0.2
Grain 5	70.220	0.068	9.847	0.068	0.093	0.030	0.027	0.027	0.033	0.001	6.15	0.06	20.6	0.2
Grain 6	35.330	0.069	4.902	0.062	0.104	0.030	BDL	0.027	BDL	0.001	6.82	0.11	22.8	0.4
Grain 7	59.789	0.071	4.710	0.063	0.092	0.031	BDL	0.028	BDL	0.002	7.47	0.15	25.0	0.5
Grain 8	421.851	0.099	6.557	0.066	0.294	0.033	0.026	0.028	1.307	0.006	5.45	0.37	18.3	1.2
ALS05, conglomerate, 358981 N, 4027944 E, J = 0.0018727 ± 1.64E-06														
Grain 1	80.843	0.065	12.541	0.049	0.134	0.037	0.041	0.032	0.012	0.001	6.15	0.04	20.7	0.1
Grain 2	169.540	0.080	21.464	0.056	0.315	0.034	0.035	0.031	0.021	0.001	7.61	0.03	25.5	0.1
Grain 3	121.758	0.079	10.068	0.069	0.102	0.032	BDL	BDL	0.012	0.001	11.73	0.09	39.2	0.3
Grain 4	421.156	0.095	5.852	0.064	0.157	0.031	BDL	BDL	0.018	0.001	71.00	0.81	225.2	2.4
Grain 5	41.610	0.068	5.826	0.066	0.066	0.035	0.010	0.026	0.016	0.001	6.32	0.09	21.2	0.3
Grain 6	321.959	0.092	4.434	0.060	0.087	0.029	BDL	BDL	0.019	0.001	71.26	1.00	226.0	3.0
Grain 7	397.949	0.109	5.472	0.063	0.099	0.030	0.056	0.026	0.023	0.001	71.43	0.85	226.5	2.5
Grain 8	105.007	0.076	14.146	0.071	0.174	0.031	0.002	0.027	0.052	0.001	6.33	0.05	21.3	0.1
Grain 9	102.775	0.082	13.172	0.067	0.141	0.035	0.075	0.028	0.044	0.001	6.82	0.05	22.9	0.2
Grain 10	188.908	0.088	11.275	0.066	0.156	0.030	0.041	0.027	0.019	0.001	16.24	0.10	54.0	0.3
ALS07, schist, 360528 N, 4025622 E, J = 0.0018683 ± 1.67E-06														
Grain 1	33.543	0.065	3.427	0.068	0.156	0.029	0.011	0.028	0.043	0.001	6.06	0.17	20.3	0.6
Grain 2	26.282	0.065	2.400	0.066	0.085	0.033	BDL	BDL	0.034	0.001	6.71	0.26	22.5	0.9
Grain 3	42.623	0.065	3.755	0.067	0.133	0.030	0.025	0.029	0.018	0.001	9.92	0.21	33.1	0.7
Grain 4	28.054	0.068	2.947	0.065	BDL	BDL	0.071	0.028	0.024	0.001	7.08	0.20	23.7	0.7
Grain 5	31.459	0.068	3.815	0.063	0.125	0.028	BDL	BDL	0.021	0.001	6.63	0.15	22.2	0.5
Grain 6	55.190	0.069	6.447	0.066	0.027	0.032	BDL	BDL	0.035	0.001	6.94	0.09	23.2	0.3
Grain 7	48.837	0.069	5.591	0.061	0.075	0.030	0.012	0.028	0.037	0.001	6.75	0.10	22.6	0.3
ALS11, meta-rhyolite, 360636 N, 4025605 E, J = 0.0018624 ± 1.84E-06														
Grain 1	40.401	0.069	4.984	0.064	0.028	0.032	BDL	BDL	0.021	0.001	6.83	0.12	22.8	0.4
Grain 2	64.113	0.075	6.144	0.064	0.106	0.030	0.009	0.027	0.039	0.001	8.56	0.11	28.5	0.4
Grain 3	50.230	0.071	5.484	0.062	0.195	0.029	0.020	0.027	0.028	0.001	7.67	0.12	25.6	0.4
Grain 4	91.195	0.074	10.671	0.068	0.211	0.028	0.001	0.030	0.028	0.001	7.76	0.07	25.9	0.2
Grain 5	70.605	0.075	5.331	0.063	0.150	0.031	0.044	0.027	0.037	0.001	11.17	0.15	37.1	0.5
Grain 6	68.183	0.071	7.893	0.066	0.053	0.030	0.023	0.030	0.014	0.001	8.12	0.08	27.1	0.3
Grain 7	155.655	0.074	6.880	0.064	0.069	0.028	BDL	BDL	0.014	0.001	21.99	0.22	72.4	0.7
Grain 8	65.690	0.077	6.492	0.065	0.114	0.028	0.009	0.026	0.011	0.001	9.62	0.11	32.0	0.4
Grain 9	73.553	0.077	9.062	0.058	0.167	0.030	BDL	BDL	0.013	0.001	7.69	0.06	25.7	0.2
Grain 10	65.497	0.072	8.451	0.064	0.060	0.030	0.017	0.027	0.019	0.001	7.08	0.07	23.6	0.2
Grain 11	46.887	0.072	5.807	0.062	0.007	0.030	BDL	BDL	0.003	0.001	7.92	0.10	26.4	0.3
ALS12, paleosol, 361335 N, 4024917 E, J = 0.0018553 ±1.53E-06														
Grain 1	135.290	0.081	17.025	0.071	0.248	0.030	0.273	0.027	0.029	0.002	7.45	0.04	24.8	0.1
Grain 2	115.421	0.067	13.559	0.069	0.160	0.031	0.135	0.030	0.018	0.001	8.12	0.05	27.0	0.2
Grain 3	164.371	0.094	19.554	0.075	0.209	0.032	0.254	0.028	0.032	0.001	7.93	0.04	26.4	0.1
Grain 4	152.192	0.079	17.298	0.069	0.208	0.029	0.041	0.028	0.019	0.001	8.46	0.04	28.1	0.1
Grain 5	94.091	0.067	10.737	0.068	0.143	0.029	0.147	0.028	0.010	0.001	8.49	0.07	28.2	0.2
Grain 6	38.540	0.070	4.408	0.066	0.057	0.030	0.012	0.026	0.012	0.001	7.93	0.14	26.4	0.5
Grain 7	37.744	0.063	4.311	0.063	0.043	0.032	0.097	0.026	0.011	0.001	7.99	0.14	26.6	0.5
Grain 8	53.296	0.070	3.775	0.057	0.028	0.029	0.066	0.026	0.009	0.001	13.43	0.23	44.4	0.7
ALS13, conglomerate, 363067 N, 4025097 E, J = 0.0018606 ± 1.21E-06														
Grain 1	77.882	0.071	3.240	0.069	BDL	BDL	1.629	0.028	0.091	0.002	16.15	0.39	53.4	1.3
Grain 2	252.408	0.092	12.366	0.067	0.155	0.028	0.174	0.028	0.135	0.002	17.17	0.11	56.7	0.4
Grain 3	182.288	0.082	9.055	0.060	0.103	0.030	0.191	0.027	0.081	0.002	17.50	0.13	57.8	0.4
Grain 4	255.616	0.092	11.441	0.066	0.203	0.029	0.407	0.029	0.153	0.002	18.40	0.13	60.7	0.4
Grain 5	210.818	0.098	10.218	0.066	0.166	0.032	0.297	0.029	0.094	0.002	17.94	0.13	59.2	0.4
Grain 6	161.473	0.083	7.657	0.068	0.057	0.031	0.641	0.027	0.112	0.002	16.82	0.18	55.6	0.6
ALS17, schist, 363135 N, 4025970 E, J = 0.0018653 ± 1.08E-06														
Grain 1	74.377	0.076	1.173	0.065	0.039	0.028	0.026	0.027	0.005	0.001	62.19	3.56	198.0	10.7
Grain 2	83.820	0.077	3.462	0.064	0.033	0.030	BDL	BDL	0.013	0.001	23.12	0.45	76.2	1.4
Grain 3	62.548	0.070	2.969	0.043	0.045	0.032	BDL	BDL	0.021	0.001	18.97	0.30	62.7	1.0
Grain 4	146.644	0.118	3.322	0.008	0.053	0.035	0.009	0.031	0.040	0.001	40.51	0.15	131.4	0.5
Grain 5	81.121	0.076	4.250	0.009	BDL	BDL	0.045	0.032	0.014	0.001	18.08	0.08	59.8	0.3
Grain 6	51.730	0.067	2.603	0.059	BDL	BDL	0.028	0.028	0.008	0.001	18.93	0.46	62.6	1.5
Grain 7	50.061	0.068	2.087	0.063	0.031	0.029	0.080	0.028	0.016	0.001	21.82	0.69	72.0	2.2
Grain 8	36.898	0.069	1.368	0.065	0.010	0.032	0.079	0.029	0.041	0.001	18.23	0.94	60.3	3.1

† below detection limits

Appendix E. Additional WDS compositional maps of muscovite

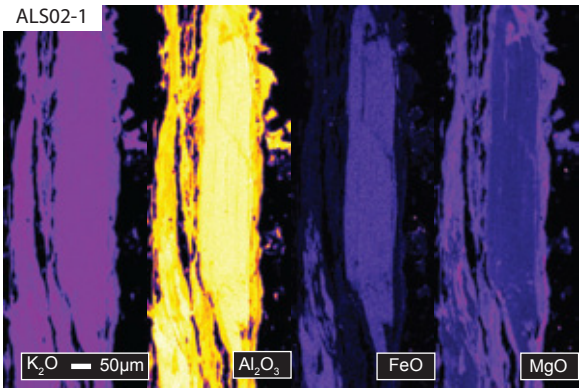

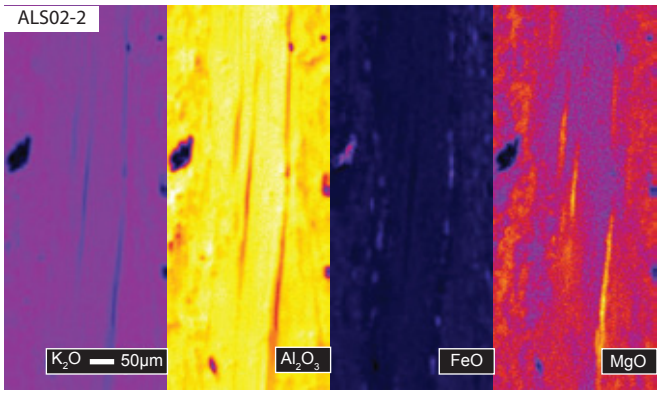

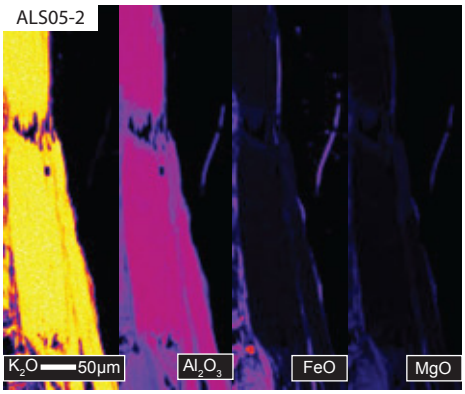

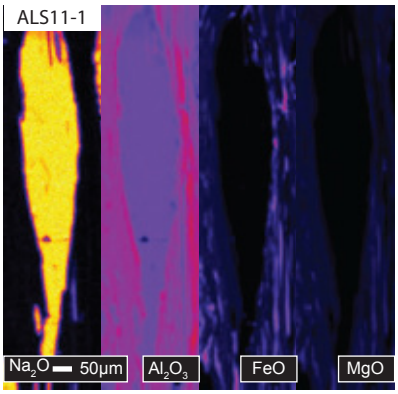

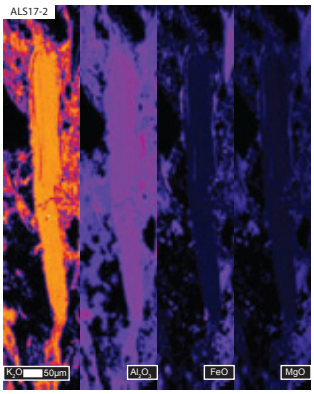

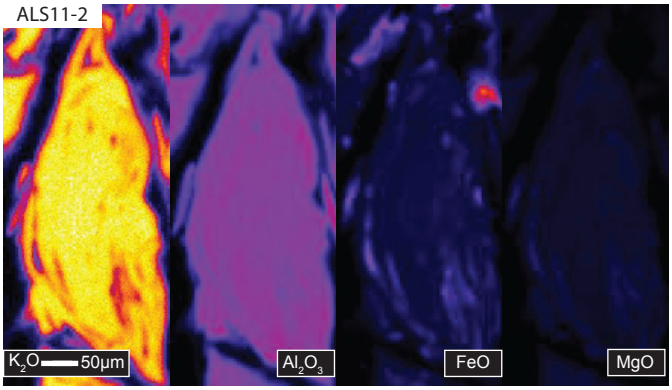

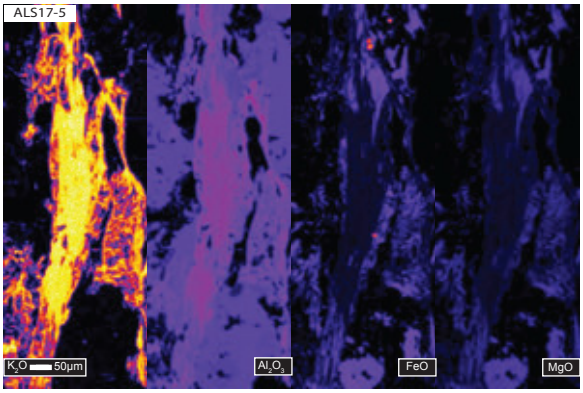

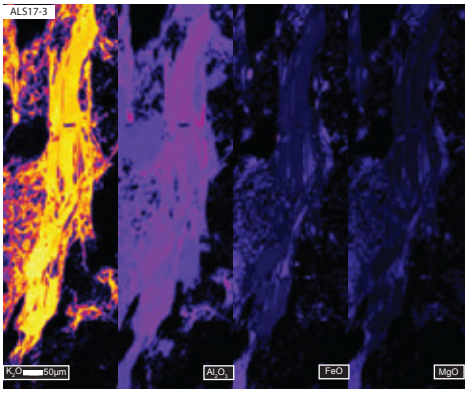

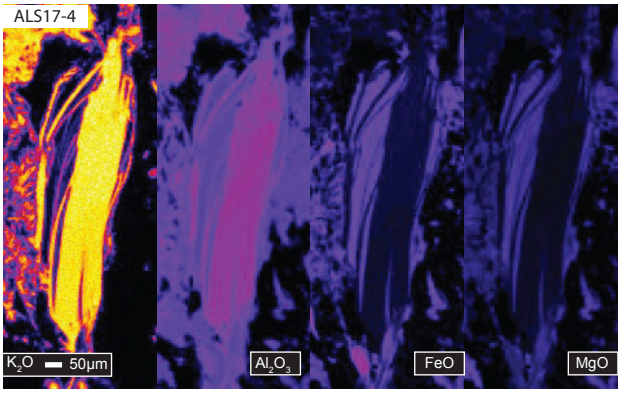

Appendix F. Single grain (U-Th)/He analyses of zircon from Thera (Santorini), Greece

Sample	Mass (mg)	rs (mm)	^{4}He (nmol/g)	±	U (ppm)	±	Th (ppm)	±	Sm (ppm)	±	eU	Th/U	F_t	± (%)	Raw Date (Ma)	±	Corrected Date (Ma)	±
ALS02, quartzite, 359540 N, 4027830 E																		
Z01	4.94	52.2	6.7	0.0	169.8	2.1	112.5	1.5	2.6	5.8	196	0.66	0.78	8.1	6.3	0.1	8.0	0.7
Z02	8.18	62.0	12.0	0.0	205.4	3.1	188.7	4.3	7.3	9.6	250	0.92	0.81	7.0	8.9	0.1	10.9	0.8
Z03	2.75	45.8	4.7	0.1	113.2	1.5	74.0	1.5	6.5	17.0	131	0.65	0.75	7.8	6.7	0.1	8.9	0.7
Z04	4.27	53.4	7.0	0.0	183.1	2.8	119.0	2.1	0.0	0.0	211	0.65	0.79	7.0	6.2	0.1	7.8	0.5
Z05	2.15	41.4	10.5	0.1	248.1	2.6	304.8	6.5	0.0	0.0	320	1.23	0.72	12.8	6.1	0.1	8.4	1.0
Z06	2.02	40.2	4.4	0.0	104.2	1.4	75.8	1.4	0.0	0.0	122	0.73	0.72	12.5	6.6	0.1	9.2	1.1
ALS03a, dacite, 359381 N, 4027820 E																		
Z01	9.63	66.7	97.7	0.2	2740.4	46.9	794.8	9.9	1.3	3.6	2927	0.29	0.83	7.0	6.2	0.1	7.5	0.5
Z02	17.6	84.9	57.5	0.2	1676.7	18.8	446.4	7.7	0.9	1.0	1782	0.27	0.86	7.0	6.0	0.1	6.9	0.5
Z03	2.78	42.3	115.1	0.4	3505.4	49.4	1652.4	26.8	0.0	0.0	3894	0.47	0.73	9.7	5.5	0.1	7.5	0.7
Z04	5.84	54.5	72.6	0.2	2195.5	40.2	774.4	10.5	2.5	7.2	2378	0.35	0.79	7.0	5.7	0.1	7.2	0.5
Z05	7.06	60.1	115.4	0.3	3128.7	48.2	1084.3	14.5	1.4	2.7	3383	0.35	0.81	7.0	6.3	0.1	7.8	0.6
Z06	4.85	53.2	93.5	0.1	2773.3	38.0	972.8	15.8	0.0	0.0	3002	0.35	0.79	7.3	5.8	0.1	7.3	0.5
ALS05, conglomerate, 358981 N, 4027944 E																		
Z01	3.44	46.8	9.2	0.1	256.6	5.5	51.3	0.8	0.0	0.0	269	0.20	0.76	8.2	6.3	0.1	8.3	0.7
Z02	3.60	46.8	22.3	0.1	708.5	6.2	140.8	1.9	0.0	0.0	742	0.20	0.76	10.8	5.6	0.0	7.3	0.8
Z03	3.76	47.1	8.6	0.0	209.2	4.4	126.8	2.0	0.0	0.0	239	0.61	0.76	11.1	6.6	0.1	8.7	1.0
Z04	7.15	58.3	3.7	0.0	98.2	1.6	39.2	1.0	2.2	6.0	107	0.40	0.81	7.0	6.4	0.1	7.9	0.6
Z05	3.10	47.1	5.0	0.0	114.0	1.5	183.9	2.8	0.0	0.0	157	1.61	0.75	8.1	5.9	0.1	7.8	0.6
Z06	2.41	43.4	4.5	0.1	129.5	1.7	90.5	1.3	0.0	0.0	151	0.70	0.74	9.3	5.5	0.1	7.4	0.7
Z07	3.27	48.5	11.6	0.0	350.9	4.1	85.1	1.3	0.0	0.0	371	0.24	0.77	7.3	5.8	0.1	7.5	0.6
Z08	4.08	45.8	3.9	0.0	114.4	1.6	126.2	2.1	0.8	7.8	144	1.10	0.75	12.1	5.0	0.1	6.6	0.8
ALS08, schist, 360641 N, 4025605 E																		
Z01	13.8	69.0	15.0	0.0	246.6	3.9	54.4	0.7	0.0	0.0	259	0.22	0.84	7.0	10.7	0.2	12.9	0.9
Z02	5.94	53.4	4.2	0.0	77.7	1.2	31.9	0.5	1.8	8.0	85.2	0.41	0.79	7.5	9.0	0.1	11.5	0.9
Z03	3.73	48.9	7.7	0.1	122.3	2.8	146.0	1.9	3.3	16.4	157	1.19	0.76	8.6	9.1	0.2	11.9	1.0
Z04	5.78	59.0	25.0	0.1	404.0	4.1	125.7	1.9	3.3	8.7	434	0.31	0.81	7.0	10.7	0.1	13.2	0.9
Z05	5.29	52.4	7.3	0.0	157.8	3.3	64.1	1.1	1.9	10.6	173	0.41	0.79	7.0	7.9	0.2	10.0	0.7
Z06	6.44	54.0	5.7	0.0	137.1	1.2	26.3	0.7	4.4	11.8	143	0.19	0.79	7.3	7.3	0.1	9.2	0.7
ALS13, conglomerate, 363067 N, 4025097 E																		
Z01	5.83	57.5	28.0	0.1	337.6	5.4	45.9	0.6	0.0	0.0	348	0.14	0.80	7.0	14.9	0.2	18.5	1.3
Z02	7.53	57.7	7.5	0.0	93.3	1.9	67.7	1.0	1.9	7.1	109	0.73	0.80	7.0	12.8	0.2	15.9	1.1
Z03	4.19	50.8	24.7	0.1	274.8	4.7	160.8	1.7	0.7	6.2	313	0.58	0.78	7.0	14.6	0.2	18.9	1.3
Z04	1.89	37.3	29.1	0.1	416.2	5.8	128.0	2.7	0.0	0.0	446	0.31	0.70	7.0	12.1	0.2	17.2	1.2
Z05	4.03	51.9	56.3	0.2	754.5	18.4	205.2	3.9	1.0	10.9	803	0.27	0.78	7.0	13.0	0.3	16.6	1.2
Z06	3.64	48.5	8.5	0.0	121.9	2.4	59.9	0.7	4.0	12.3	136	0.49	0.77	7.0	11.6	0.2	15.1	1.1
Z07	1.69	34.6	9.4	0.1	124.4	2.9	85.4	3.3	0.6	18.5	144	0.69	0.68	7.0	12.0	0.3	17.7	1.3
Z08	3.26	46.0	67.4	0.2	708.8	8.8	330.5	4.6	0.0	0.0	786	0.47	0.76	7.0	15.9	0.2	21.0	1.5
ALS17, schist, 363135 N, 4025970 E																		
Z01	3.48	45.5	47.4	0.1	570.2	13.7	207.0	3.5	6.5	14.4	619	0.36	0.75	7.0	14.2	0.3	18.9	1.4
Z02	4.47	54.3	23.3	0.0	138.3	4.0	93.7	2.7	2.2	8.3	160	0.68	0.79	7.0	26.9	0.7	34.0	2.5
Z03	3.25	45.5	31.0	0.1	428.6	6.8	69.7	1.5	5.2	15.7	445	0.16	0.75	7.0	12.9	0.2	17.1	1.2
Z04	1.92	40.0	31.5	0.1	376.0	7.8	146.6	2.0	0.0	0.0	410	0.39	0.72	7.0	14.2	0.3	19.7	1.4
Z05	2.43	42.2	31.6	0.1	216.8	2.9	165.5	2.6	2.8	15.3	256	0.76	0.73	7.0	22.9	0.3	31.2	2.2
Z06	2.13	41.4	39.2	0.1	337.4	7.1	89.9	1.7	29.9	41.1	359	0.27	0.73	7.0	20.2	0.4	27.6	2.0
Z07	2.53	44.1	96.3	0.2	600.0	8.9	240.0	6.5	0.0	0.0	656	0.40	0.75	7.0	27.2	0.4	36.4	2.5
Z08	1.41	35.4	16.6	0.1	186.1	4.3	108.7	2.2	6.3	50.6	212	0.58	0.69	7.0	14.5	0.3	21.1	1.5

Note: Coordinates are Universal Mercator (UTM) zone 35S. rs- radius of a sphere with an equivelant area to volume ratio as the crystal; F_t- α ejection correction factor.